Developing Highly Efficient Lead Halide Perovskite Solar Cells

by

Jason J. Yoo

B.S. Chemistry, The University of Texas at Austin (2015)

Submitted to the Department of Chemistry
in partial fulfillment of the requirements for the degree of

Doctor of Philosophy in Chemistry

at the

MASSACHUSETTS INSTITUTE OF TECHNOLOGY

May 2020

Author . . . .
Department of Chemistry
May 1, 2020

Certified by . . . .
Moungi G. Bawendi
Lester Wolfe Professor of Chemistry
Thesis Supervisor

Accepted by . . . .
Robert W. Field
Haslam and Dewey Professor of Chemistry
Chairman, Department Committee on Graduate Theses

This doctoral thesis has been examined by a Committee of the
Department of Chemistry as follows:

Professor Gabriela Schlau-Cohen..
Chairman, Thesis Committee
Cabot Career Development Assistant Professor of Chemistry

Professor Moungi G. Bawendi..
Thesis Supervisor
Lester Wolfe Professor of Chemistry

Professor Keith Nelson..
Member, Thesis Committee
Haslam and Dewey Professor of Chemistry

Developing Highly Efficient Lead Halide Perovskite Solar Cells

by

Jason J. Yoo

Submitted to the Department of Chemistry
on May 1, 2020, in partial fulfillment of the
requirements for the degree of
Doctor of Philosophy in Chemistry

Abstract

Lead halide perovskite solar cells are an emerging technology that can be solution processed to yield low-cost, light weight and flexible photovoltaics. Much of the early work has been focused on developing device structures and processing techniques to improve light absorption and eliminate detrimental traps within the bulk of the perovskite active layer. As a result, the device efficiency of perovskite solar cells has improved from $\sim$3% up to $\sim$20% in less than a decade. However, the device efficiency of perovskite solar cells still need to be much improved in order to compete with traditional photovoltaic technologies, such as Silicon and GaAs, and to ultimately realize the theoretically determined Shockley-Queisser (SQ) efficiency limit.

In this thesis, I focus on the development of a novel interface passivation strategy called selective precursor dissolution (SPD) strategy, that utilizes low dimensional 2D perovskites as the interface passivating layer. The post treatment of the bulk perovskite thin film with 2D perovskites via SPD strategy prevented formation of a detrimental non-perovskite phase at the interface and resulted in much improved thin film quality with reduced detrimental interface recombination. As a result, a certified power conversion efficiency (PCE) of 22.6% is achieved from a quasi steady-state measurement along with an electroluminescence (EL) efficiency up to $\sim$9%. Both device metrics were the highest values reported at the time of publication.

In addition to developing an interface passivation strategy to improve device performance, a high quality electron transport layer (ETL) was developed and a new perovskite composition was adopted to further improve the device performance. A chemical bath deposition (CBD) was used for the synthesis of a tin dioxide (SnO_2) ETL. The pH of the reaction solution is identified as the key parameter for the CBD of SnO_2 that controls the quality of the SnO_2 ETL. pH 1.5 is determined to be the optimum acidity that results in a SnO_2 ETL with compact and conformal coverage without producing a detrimental secondary crystal phase.

To improve the optoelectronic properties of the perovskite active layer, $MAPbBr_3$ is significantly reduced to minimize the band gap penalty, which also resulted in improved effective carrier mobility. $MAPbBr_3$ is commonly added to the perovskite composition to stabilize the α-phase $FAPbI_3$ but results in an increase in the band gap. Addition of 0.8 mol% of $MAPbBr_3$ to the $FAPbI_3$ perovskite resulted in much improved carrier lifetime and effective mobility, compared to conventionally added 10 mol%.

Together with the new SnO_2 and the perovskite active layer, a record setting and certified PCE of 25.2% is achieved, which translates to 80.5% of the SQ limit for its band gap. In addition, due to low open-circuit voltage (V_{OC}) loss, the newly developed devices exhibit an EL efficiency up to 17.2% and an EL wall-plug efficiency up to 21.6%. Both PCE and the EL efficiency is the highest reported so far from a single perovskite solar cell structure.

Thesis Supervisor: Moungi G. Bawendi
Title: Lester Wolfe Professor of Chemistry

Acknowledgments

I would like to first thank my research advisor Professor Moungi Bawendi. The skill sets and knowledge I learned under Moungi's advisement is invaluable. I acknowledge I came into graduate school without much independent research background. However, by interacting with Moungi and setting him as my touchstone, I learned how to ask the right questions, formulate a compelling storyline for a paper, and pitch my ideas for a proposal. I now realize how valuable these intangible skill sets are and I am confident these will become useful in my future careers. In addition, I am thankful for the amount of time I was able to spend interacting with him, whether it is during meetings, discussions in the hallway, or while I am walking him to the car in the parking lot as he is going to his next meeting at MGH. Lastly, thank you for driving me back to Boston all the way from Vermont after I broke my leg at the Killington ski resort! I promise I'll behave and always carry my insurance card.

I also would like to thank my thesis committee members, Professor Gabriela Schlau-Cohen and Professor Keith Nelson. I really appreciate the fresh point of views they offered with respective to their own expertise. Also I enjoyed the interactions I had with them during committee meetings.

I could not have been here in this place if it weren't for my Mom and Dad, literally. Mom, I know how curious you are as to how I'm doing on a daily basis and I regret not calling you more often. You believed in me, I think, even when I doubted myself and it has been my motivation to keep pursuing and push forward. You always told me "Be yourself" and learn how to make independent decisions that I can take responsibility of. There were times when I just wanted to ride someone else's coattail and compromise with the situation. I am glad I didn't and you deserve so much more credit than I can offer. I love you Mom. Dad, your support is what carried me through graduate school. I know you trust me way more than I trust myself and looking back that has been incredibly helpful in getting through tough times. You often heckle me by asking how an earth I will make it out of graduate school successfully. I'm proud to say that I did all thanks to you! I love you Dad.

I would also like to thank my only sibling. Thank you Jennifer for not making my life more miserable. Moving on, Next.

Eric, you and I both know we spent too much time together. I'm not proud of it but oh boy was it fun. Like taking tequila shots on Tuesday afternoons whenever our experiments wouldn't go as planned. So that's like every Tuesday huh? I cherish every moment we had at Green Street, even though most of the time the conversations went no where and you got frustrated and tried to convince me to join you at the Cantab Lounge to watch people waste their pension money together. Thank you for making my PhD extra spicy and please get rich so that I can retire soon. Also, I forgive you for not getting me the correct trail mix from Costco when I couldn't go grocery shopping due to a broken leg.

Sophie, you are a gem. I don't know how you handled me asking for favors every other day, ranging from fixing the TCSPC set up that I messed up and taking me to Costco. Thank you for having so much patience with me. I will definitely miss us just out of nowhere judging people by their outfit as they innocently walk by Clover while enjoying morning popovers. I appreciate you not holding back and pointing out that I need to loose my love handles and taking me to the gym with you. I was only able to survive "gym at two" (pronounced /Jĭmi Tŭ/) each day only because there was Snack (pronounced /SHoü Nääk/) Daddy waiting for me at the kitchen!!! Boris, I have to confess; I love your dad jokes. No matter what other people say, don't ever change that. I will definitely miss making dumb and silly jokes at Loyal Nine and embarrassing Sophie in front of others. I will never forget our trip to Montana and especially the last minute decision to go to the Water of the Gods hotsprings. It was CLUTCH!

I was fortunate to live with Matthias and Odin during most of my time at MIT. Some people say you shouldn't live with lab mates but I can prove them wrong. I can count back to so many memorable moments while living at 24A with you guys; painting night, Fried Food Friday, and talking behind the back of our landlord for poor managements. Also, I appreciate you guys taking care of me while I was out of service for almost 3 months from the snowboard accident. It definitely made the not-so-fun period much more manageable.

I will remember all of Bawendi group members that I have cross paths with. Special shout-out to Jess for adopting me as her mentee when I was confused and lost in first year of graduate school, Mari for letting me take goofy photos of her and putting them up as my ending slide for my group meeting presentation, and Yongli for courageously deciding to be my mentee and eventually be in charge of the subgroup.

I would like to thank Dr. Seong Sik Shin at KRICT, who I consider as my second advisor. You taught me how to make a solar cell from scratch and what is important when it comes to perovskite solar cells. Although we didn't overlap much at MIT, I'm glad we were able to keep working together and set several world records together! You are full of creative ideas and designing fun experiments, which I look up to. I look forward to working together at KRICT soon.

Most of my work is smeared with Matthew's fingerprint and it's for a reason. Matthew has been exceptionally helpful in characterizing perovskite solar cells and understanding their dynamics. I appreciate you teaching basic device physics to me in "r/explainlikeimfive" mode, which is the only way I could understand device physics. I know there were many times when I was behind in making devices for your experiments and I appreciate you having patience with me. I hope our paths cross again in the near future.

Dr. Mahmooda Sultana and the rest of NASA team has been extremely helpful in developing ideas for the quantum dot spectrometer project. I feel very lucky to be able to visit Goddard Space Flight Center, through the NASA fellowship, and work closely with the senior engineers and ultimate install the picoliter dispenser that will one day fabricate the quantum dot hyperspectral imager! I look forward to the research that will come out of Dr. Sultana's team.

I am writing my PhD thesis and defending during a COVID-19 pandemic. Due to social distancing, my PhD defense will be done over video conference. This means I could get away with doing my defense by just wearing a shirt and underwear! Just kidding, I don't wear underwear.

I would like to thank National Aeronautics and Space Administration (NASA)

for their support through the NASA Space Technology Research Fellowships and also Eni S.p.A., which funded the projects through the MIT Energy Initiative.

Contents

List of Figures

Chapter 1

Introduction

1.1 Lead Halide Perovskite

1.1.1 Why Study Lead Halide Perovskites?

Perovskites are a class of material that follow the crystal structure of $CaTiO_3$ with the chemical formula ABX_3. Specifically, organic/inorganic lead halide perovskite, such as methylammonium lead iodide ($MAPbBr_3$) and cesium lead bromide ($CsPbBr_3$), is a category of perovskite semiconductor that is of particular interest for optoelectronic applications. The general crystal structure of a lead halide perovskite with the chemical formula ABX_3 is shown in Figure 1-1. The A site cation is surrounded by an octahedral cage of $[PbX_6]^{4-}$. If all three unit cell lengths are the same (a=b=c), then it forms a cubic phase, a tetragonal phase if two of the unit cell lengths are the same(a≠b=c), and an orthorhombic phase if all three are different (a≠b≠c).

Over the last decade or so, an immense interest in understanding the fundamental material properties and photophysics of these perovskite materials have lead to the development of highly efficient perovskite-based optoelectronics. For example, perovskite solar cells are now the most efficient photovoltaics technology within thin film categories, which includes Cadmium Telluride (CdTe) and Copper Indium Gallium Selenide (CIGS) that has >50 years of research background, and is within striking distance of the efficiency of Silicon and GaAs solar cells. Figure 1-2 shows the record

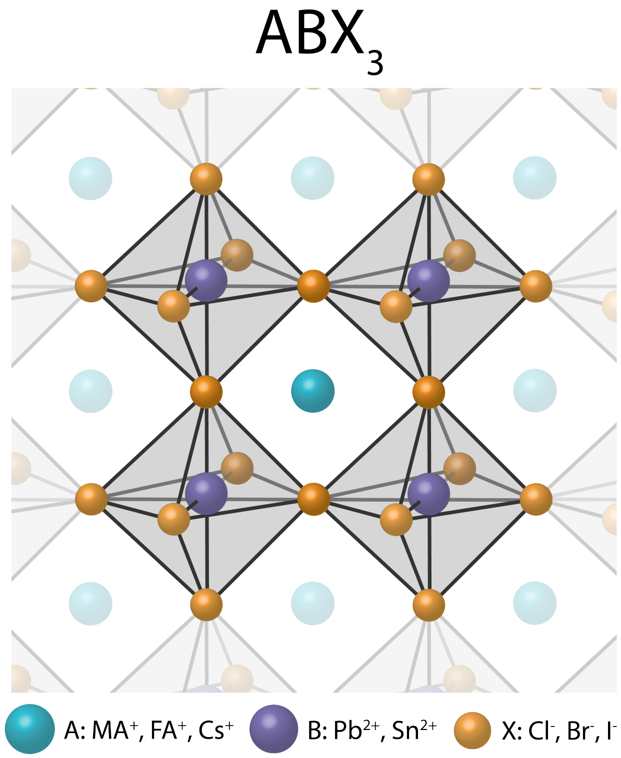

Figure 1-1: Illustration of the perovskite crystal structure with the chemical formula ABX_3.

research solar cell performance published by National Renewable Energy Laboratory (NREL). Perovskite solar cells efficiency has improved at a rate that has not been observed before. So, why is perovskite such an attractive class of material for optoelectronic devices and why are we so interested in these perovskites?

There are several key traits that distinguish perovskites from other classes of semiconductors. I have summarized these key traits into four categories: solution processability, band gap tunability, intrinsic optoelectronic properties, and high specific-power (Figure 1-3)

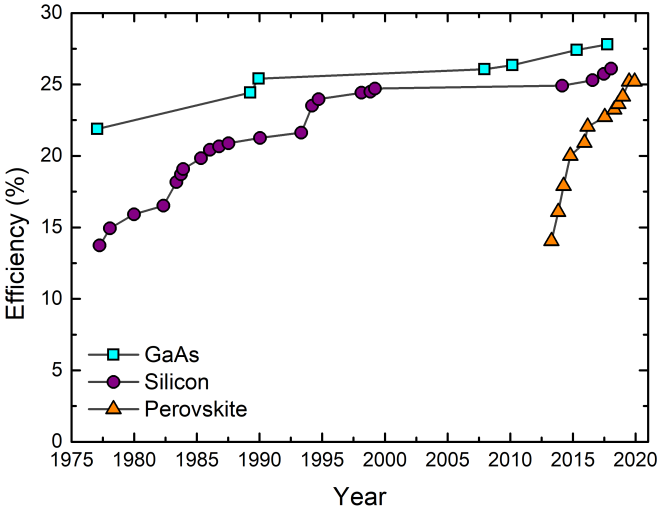

Figure 1-2: Plot of progress in efficiency for Silicon, GaAs, and perovskite solar cell. Perovskite solar cell was first included in the NREL chart in 2013 and is demonstrating impressive improvements in efficiency.

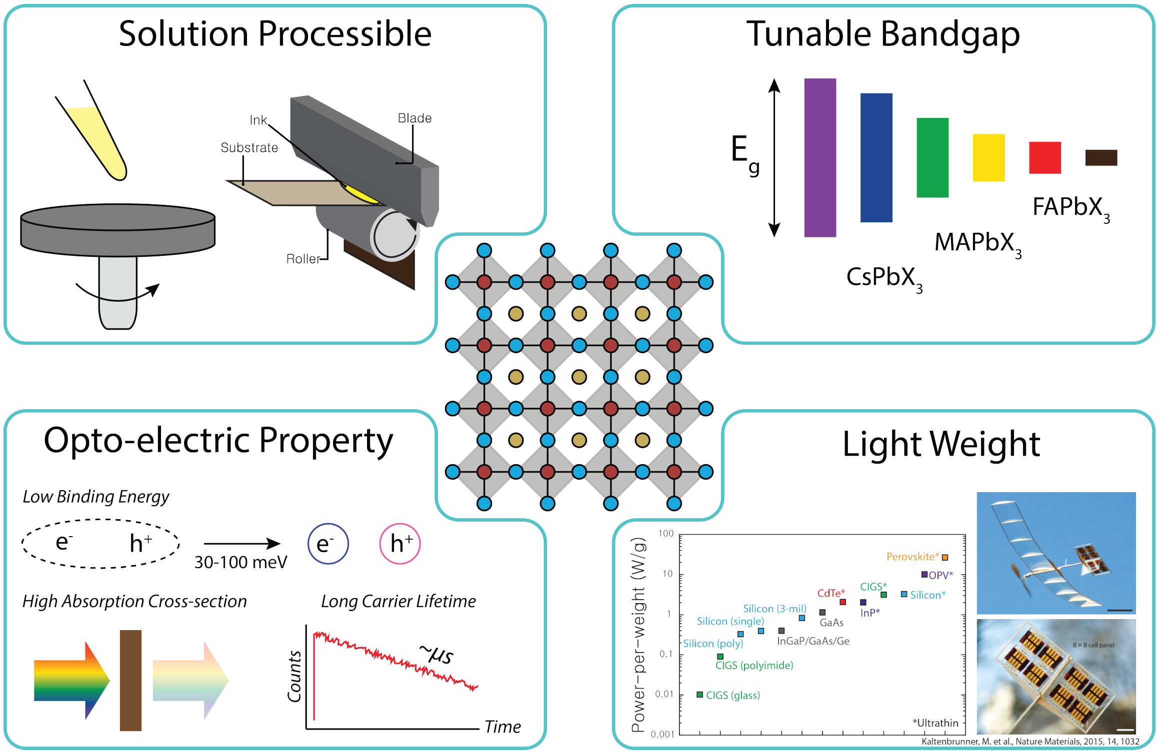

Figure 1-3: Properties of lead halide perovskites. Figures in "Light Weight" is adapted with permission from ref[1]. Copyright (2015) Springer Nature.

Solution Processing

Perovskites are "easy" to make. This is a huge trait for scientific research as it allows various researchers to explore perovskite based on their own area of expertise, ranging from synchrotron-based measurements to single molecule spectroscopy. Typically, to prepare a perovskite thin film, a "perovskite ink" that is composed of lead halide (such as PbI_2) and an A site cation (such as MAI) dissolved in polar solvents, such as DMF and DMSO, is deposited onto a substrate, spin coated to obtain a uniform film, and annealed on a hot-plate at a moderate temperature (<150 °C) to evaporate the solvent and induce crystallization. As a result, perovskite solar cells can be fabricated on various substrates, from rigid glass to flexible plastic, with a wide range of form-factors. In addition, the use of solution ink allows fabrication of perovskite thin films with various deposition methods that is suitable for scale-up fabrication. For example, perovskite ink can be deposited using, but not limited to, ink-jet printing or blade-coating methods that is already widely used in the semiconductor industry (Figure 1-4).

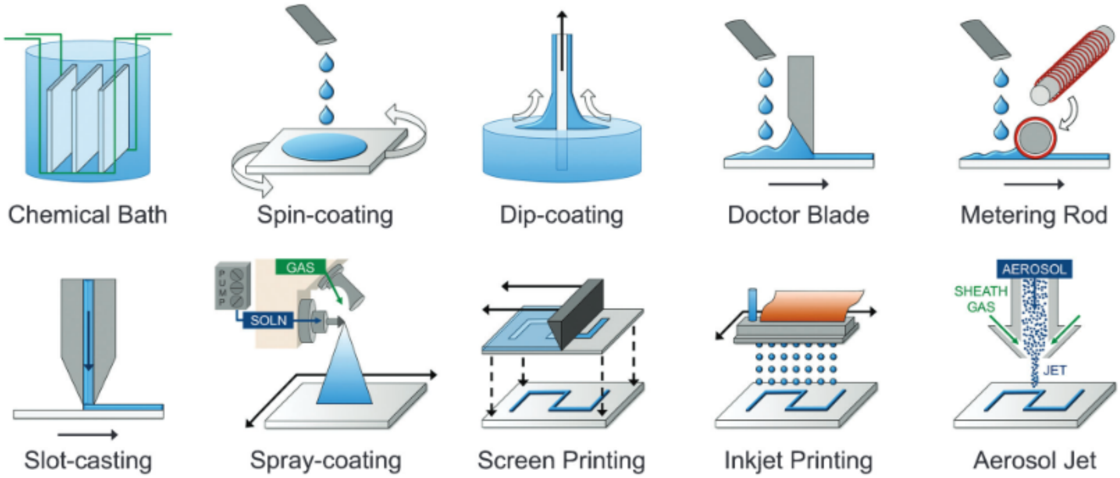

Figure 1-4: Cartoon describing various solution processing methods. Reproduced from Ref [2] with permission from The Royal Society of Chemistry.

Such perovskite thin film processing is very mild compared to fabrication of Silicon solar cell. For fabrication of Silicon solar cells, temperatures exceeding ~1500 °C is used to grow a Silicon ingot. The Silicon ingot, or the crystal, is cut into a more manageable size known as a wafer (Figure 1-5).

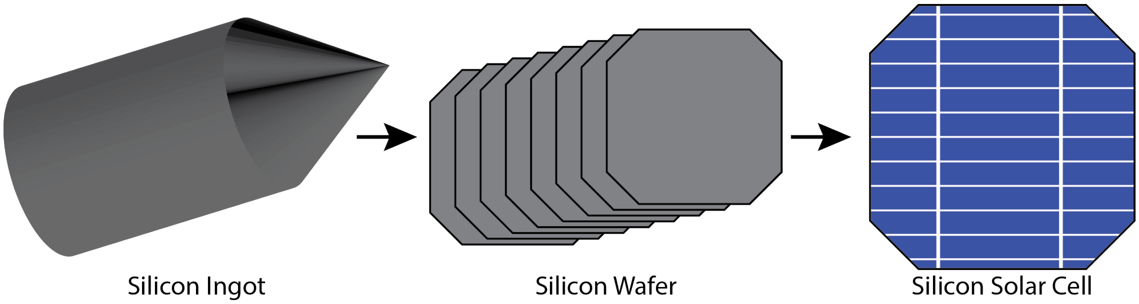

Figure 1-5: Cartoon describing how Silicon solar cells are made from Silicon ingots.

Another advantage of perovskite thin films is the reduced number of processing steps. Semiconductor nanocrystals, or quantum dots, requires several steps of purification to obtain the quantum dot ink and additional post-treatments, such as solid-state ligand exchange, for device fabrication. On the other hand, a single perovskite ink can be prepared for fabrication of high quality perovskite thin films. Not only does this simplify the fabrication steps, it becomes more important when considering the synthesis cost for commercialization purposes. The perovskite thin films offer lower materials cost compared to quantum dot based solar cells, providing a pathway for low levelized cost of energy (LCOE).[10]

Band Gap Tunability

The ability to tune the band gap of a semiconductor material offers wide range of applications, ranging from light emitting diodes (LEDs), tandem solar cells, and color multiplexing. For perovskites, the band gap of the material can easily be changed by tuning the 1) elemental composition, 2) stoichiometry, 3) crystal structure, and 4) the dimensionality of the perovskite crystal (Figure 1-6). This results in a wide parameter space for tunability and the band gap of the perovskite can span across the entire visible wavelength range.[3]

Tandem solar cells have benefited from band gap engineering of perovskite solar cells more than other aforementioned applications. Tandem solar cell is composed of two sub cells with different band gap in order to minimize the loss in energy, or photo-voltage due to carrier thermalization. A two-junction tandem solar cell can be fabricated by utilizing a perovskite as the wide band gap top cell and a Silicon or CIGS solar cell as the narrow band gap bottom cell. This structure allowed fabrication of a tandem solar cell that exhibits device efficiency up to 29.1%, which exceeds that of the single-junction Silicon solar cells. [11] In addition, perovskite-perovskite tandem solar cells can be developed exclusively using solution processing techniques, which allows fabrication of flexible and light-weight tandem solar cells.

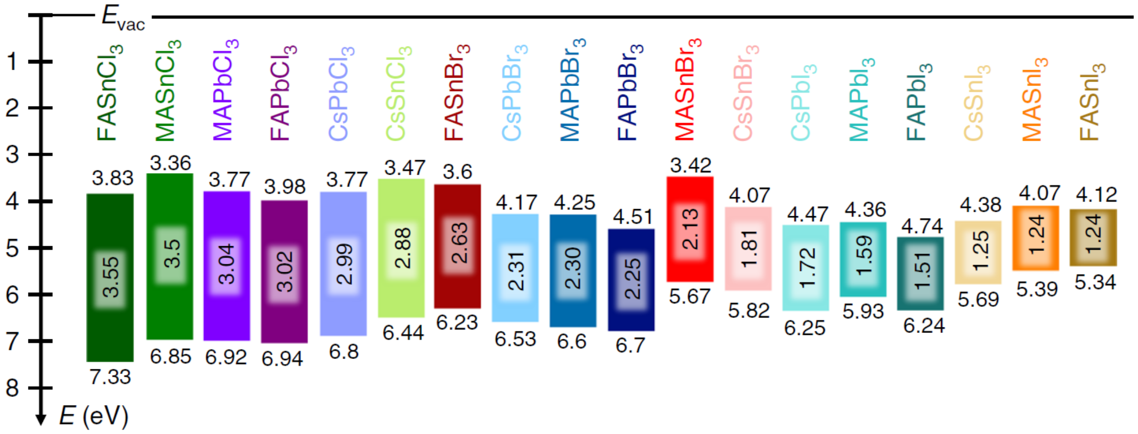

Figure 1-6: Energy level diagram of various perovskite materials showing band gap tunability of perovskites with composition tuning. [3]

Photophysics

Solar cells convert sun light into useful electricity. In order to achieve this, the photoactive layer of the solar cell, perovskite in our case, needs to 1) efficiently absorb the sun light, 2) create and separate the electron (e^-)-hole (h^+) pair, and 3) have carriers (e^- and h^+) that are long lived.

First, perovskites have high absorption coefficient. This allows perovskite thin films to efficiently absorb the sun light with relatively thin thicknesses. In the visible wavelength range, perovskites have an absorption coefficient that is ∼10 times greater than that of Silicon. As a result, a typical perovskite solar cell has an active layer thickness of 500-700 nm, where as the thickness of a Silicon solar cell exceeds several hundred micrometer. [12]

Second, perovskites exhibit low exciton binding energy. Exciton binding energy is how much energy it takes to separate the exciton (e^- and h^+ that are bound together) into free carriers. This is an important metric for solar cells as the free carriers need to be efficiently separated upon light absorption and be collected at charge selective contacts. Perovskites have an exciton binding energy of 15-40 meV, which is comparable to room temperature (k_BT=25.7 meV).[13]

Lastly, perovskites can have an extremely long carrier lifetime and is known to be "defect tolerant". Having a long carrier lifetime means that there are low density of parasitic defects that can trap the carriers that prevents efficient charge extraction. The carriers that are trapped in these parasitic defects are lost through non-radiative recombination pathways, usually as heat. Defect tolerance is an unusual property for a material that are solution processed at low temperature, which generally leads to formation of detrimental defects. For traditional solar cells, the semiconductor needs to be processed at high temperature to provide enough thermal energy for the system to reach its desired thermodynamic state to grow a single crystal with acceptable concentration of defects, or in a highly controlled environment for epitaxial growth.[14] The total trap density of solution processed perovskite is comparable to traditional semiconductors. Then why is perovskite considered as defect tolerant material?

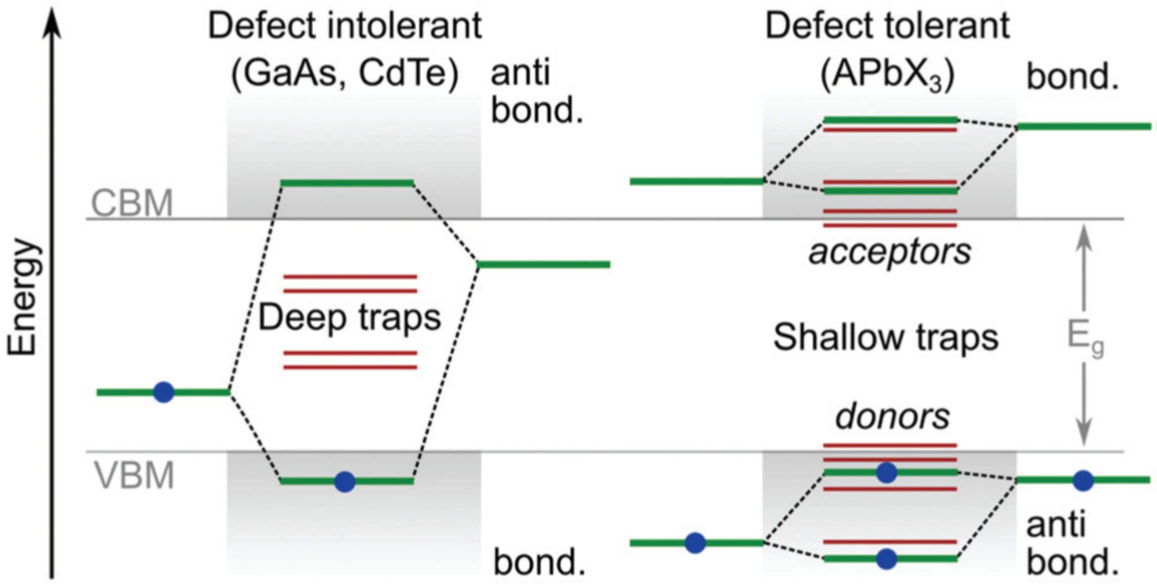

Figure 1-7: Energy level diagram of traditional semiconductor materials, GaAs and CdTe, and the location of deep traps versus "defect tolerant" perovskite (ABX_3). [4]

The nature of the traps and the relative energy position of these trap state to the conduction and valence band of the semiconductor determine its effect on the carrier dynamics (Figure 1-7). Semiconductor systems that are defect intolerant have trap states positioned deep within its band gap. The energy difference between these deep trap and the band edge is greater than thermal energy (k_BT), preventing them from thermally being excited back to the transport band. In contrast, defect tolerance perovskites have shallow traps that is positioned either within the band or very close to the band edge. This allows shallow trapped carriers to be thermally excited back into the transport bands without undergoing non-radiative recombinations.

Due to these defect tolerant behaviour, perovskite thin films exhibit extremely long carrier lifetime that is carried over to high photovoltaic efficiencies. This is because the carrier lifetime affect the carrier diffusion length, where the diffusion length can be determined though the Einstein relation,

$$L_D(n) = \sqrt{\frac{D}{R_{total}(n)}}$$

where D is the diffusion constant, $D=\mu k_BT/e$, n is the charge carrier density, μ

is the effective carrier mobility, k_B is the Boltzmann constant, e is the elementary charge, and T is the temperature. The carrier diffusion length needs to be longer than, if not comparable, to that of the physical thickness of the solar cell active layer to result in an efficient solar cell with efficient carrier extraction.

The total recombination rate $R_{total}(n)$ is,

$$R_{total}(n) = -\frac{1}{n}\frac{dn(t)}{dt} = -k_1 - k_2 n - k_3 n^2$$

where k_1 is a trap assisted monomolecular recombination rate, k_2 is a bimolecular recombination rate, and k_3 is an Auger recombination rate. For solar cell applications, having a low k_1 and a high k_2 is important as the photoluminescence quantum efficiency (PLQE) is defined as

$$PLQE = \frac{k_2 n}{k_1 + k_2 n + k_3 n^2}$$

PLQE is an important metric for solar cell application as the open-circuit voltage (V_{OC}) scales with the logarithm of the PLQE,

$$V_{OC} = V_{OC}^{radiative} + \frac{k_B T}{e} ln(PLQE)$$

(I will discuss in more detail the relationship between the PLQE and the V_{OC} of the device in relationship with the electroluminescence efficiency of the solar cell in Chapter 2.4.2)

In general, the Auger recombination rate (k_3) is several orders of magnitude lower than that of trap assisted (k_1) and bimolecular recombination (k_2) rate, and if often insignificant for carrier density at a solar irradiation of 100 mW/cm^2 (10^{15}-10^{16} cm^{-3}).

Specific Power and Form-Factor

Specific power, or power-per-weight, is a metric that indicates the amount of power a solar cell can generate per mass of the device (unit of Watts/gram). High specific power is critical for applications where there is a strict restriction on the weight of the payload, such as space missions, drones, or mobile solar power generators.[15] Due to solution processing at low temperatures and high absorption coefficient, perovskite solar cells can be fabricated on various supporting substrates, such as polyethylenimine (PEI) plastics, or even flexible substrates (Figure 1-8). Not only does this allows fabrication of perovskite solar cells with extremely high specific power, it opens up new applications where flexible solar cells need to be installed conformally to the base structure and generate power from the Sun.

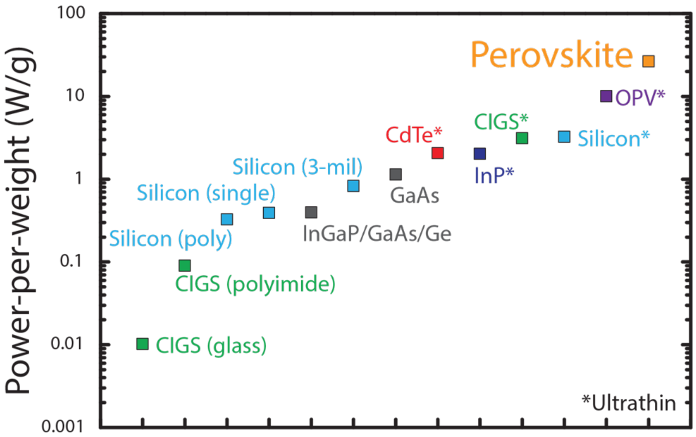

Figure 1-8: Plot of specific power, or power-per-weight, of various solar cell technologies. Adapted with permission from ref[1]. Copyright (2015) Springer Nature.

1.1.2 3D Perovskite vs Low Dimensional 2D Perovskite

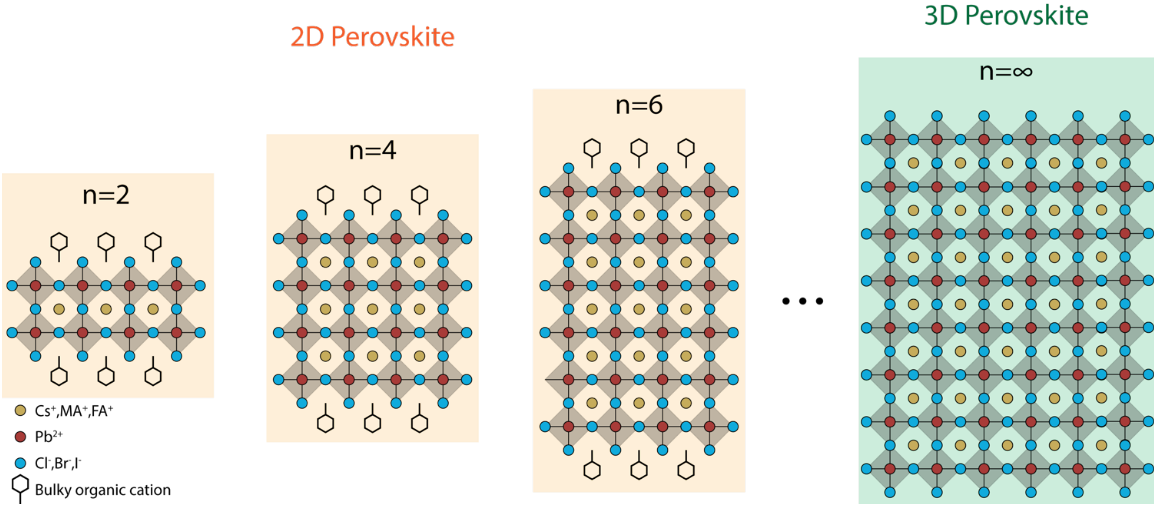

Figure 1-9: Structural comparison between 2D (yellow) and 3D (green) perovskites. The optoelectronic properties of the 2D perovskite, such as the bandgap, can be tuned by changing its n value and its bulky organic cation.

With its report as a successful photo-absorber for solar cell applications, lead halide perovskite has gained much interest due to unprecedented improvements in optoelectronic device performance. Much of the early work on perovskite optoelectronic devices has been done on bulk perovskite, or a 3D perovskite, which is depicted in Figure 1-9. 3D perovskite has an extended network of perovskite crystal structure and offers high absorption cross-section, long carrier lifetime, and long carrier diffusion length. Another family is a layered perovskite, or a 2D perovskite, which is a crystal structure with bulky organic ligands intercalating between layers of perovskite crystal structures (Figure 1-9). This occurs when the A site cation is too big or too small to stabilize the perovskite crystal structure and falls out of the optimum Goldschmidt's tolerance factor (t),

$$t = \frac{r_A + r_I}{\sqrt{2}(r_{Pb} + r_I)}$$

where r_A, r_{Pb}, and r_I, are the effective radii for A site cation, Pb^{2+}, and I^-. The Goldschmidt's tolerance factor is an empirical result and A site cations that results in t values between $0.8 < t < 1$ results in stable perovskite structures (mostly cubic or orthohombic structures), and such cations include methylammonium $CH_3(NH_3)^+$, formamidinium $CH(NH_2)_2^+$, and Cesium (Cs). On the other hand, A site cations with t values outside of 0.8-1 range results in a distorted $[PbI_6]^{4-}$ octahedra that results in non-perovskite phases. Some of the examples are shown in Figure 1-10.

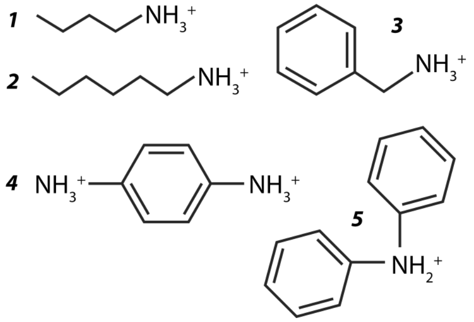

Figure 1-10: (1) n-butylammonium, (2) n-hexylammonium, (3) benzylammonium, (4) 1,4-benzene diammonium, (5) diphenylammonium

The thickness of the 2D perovskite (the n value) is determine by the number of $[PbI_6]^{4-}$ octahedra cage within the bulky organic layer. This results in 2D perovskites with a chemical formula of $(A')_m(A)_{n-1}Pb_nX_{3n+1}$, where A' is the bulky organic cation, m is either 1 for Dion-Jacobson phase (organic cations with two binding groups) or 2 for Ruddlesden-Popper phase (organic cations with a single binding group), n is the number of $[PbI_6]^{4-}$ layer, and X is the halide. In the case of 3D perovskite, the thickness is $n=\infty$.

Just like the 3D perovskite, the band gap and the optoelectronic properties of the 2D perovskite can be tuned by changing the composition, such as the A site cation, the halides, and the its stoichiometries. In addition to changing the composition, large difference in the dielectric constants between the perovskite structure and the bulky organic layer results in a strong quantum confinement of carriers within the perovskite crystal, similar to how semiconductor quantum dots exhibits quantum confinement. As a result, 2D perovskites with different n values (perovskite thickness) show different optoelectronic properties. In general, 2D perovskite with lower n value have larger band gap, higher exciton binding energy, and lower carrier mobility.

Layered 2D perovskite structures offer various advantages compared to the 3D perovskite counterpart. The hydrophobicity of the bulky organic cations in the 2D perovskite thin films results in more resistance to degradation from water and these 2D perovskite based optoelectronic devices have shown to be more tolerant to operation in humid environments. [16] In addition, the layered structures with bulky organic cations limit the ion migrations (both the A cations and the halides) within the perovskite structure and these ion migrations is shown to be linked to decrease in device performance during long-term stability tests.[17] However, these layers 2D perovskite suffer from low carrier mobility and diffusion length through the direction of the A' organic cation.[18] Thus, perovskite solar cells fabricated with layered 2D perovskites suffer from low FF and current density. Currently, much effort is put into maneuvering the orientation of the layered 2D perovskite structure so that the layers are vertical with respect to the charge transport layers.[19]

1.1.3 Important Milestones in Perovskite Solar Cells

It is worth discussing some of the important milestones in the field of lead halide perovskite solar cells that has contributed in boosting the efficiency from mere ∼3% to ∼20% in less than a decade (Figure 1-11).

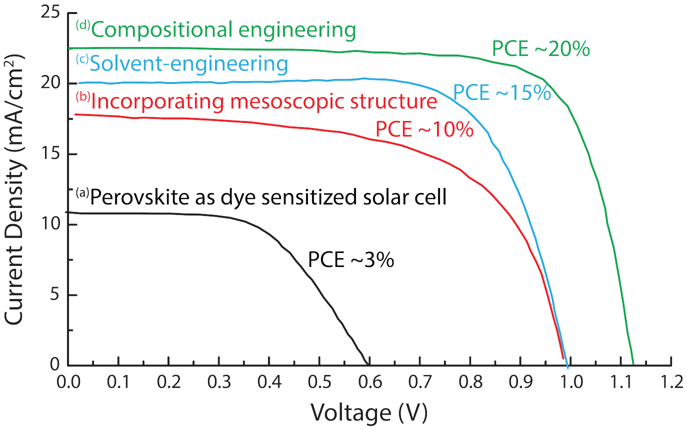

Figure 1-11: Plot of JV curves from seminal works that has contributed significantly in improving the device performance of perovskite solar cells. The JV curves were extracted using WebPlotDigitizer [(Copyright 2010-2019 Ankit Rohatgi <ankitrohatgihotmail.com>, https://automeris.io/WebPlotDigitizer)] from the following references: (a) Ref [5] ,(b) Ref [6] ,(c) Ref [7] ,(d) Ref [8]

Kojima et al. reported the first case of using lead halide perovskite material as a photo-absorber back in 2009 (Figure 1-12). [5] They report an efficiency up to ∼3% when using $MAPbI_3$ in a dye sensitized solar cell using TiO_2 as the templating scaffold.

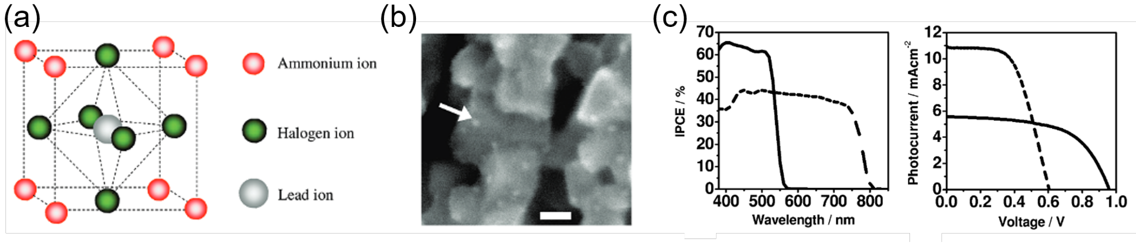

Figure 1-12: First report of using perovskite as a photo-absorbser for a photoelectrochemical cells, or a dye-sensitized solar cell. Adapted with permission from ref[5] . Copyright (2009) American Chemical Society.

Moving beyond a dye sensitized solar cell, Lee et al. reported using lead halide perovskite as a photoactive layer in a solid-state solar cell (Figure 1-13). [6] They incorporated a compact and a mesoporous metal oxide layer as the electron transport layer, which resulted in efficiency close to ~10%.

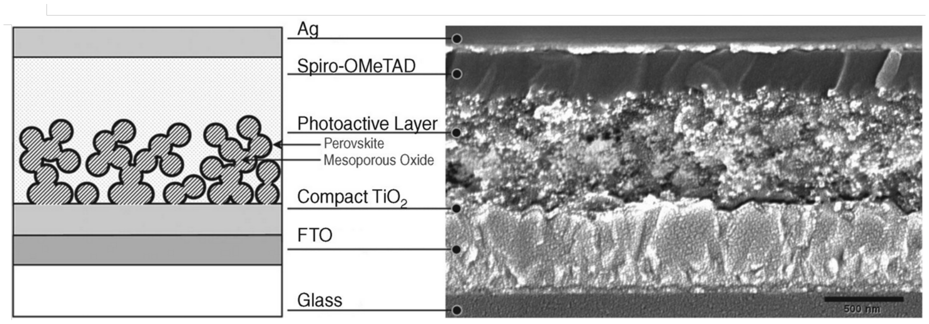

Figure 1-13: Using perovskite in a solid-state solar cell utilizing mesoporous scaffolds to improve carrier extraction. Adapted with permission from ref[6]. Copyright (2012) The American Association for the Advancement of Science.

To fabricate a high quality perovskite thin films, a fabrication technique called "solvent-engineering" was reported in 2014 by Jeon et al (Figure 1-14). [7] A solvent that does not dissolve the perovskite precursors (usually referred to as a non-solvent), is deposited onto the perovskite thin film during spin coating but prior to thermal annealing. The non-solvent treatment induces formation of an intermediate phase and an in-situ crystallization of the perovskite active layer. This allowed fabrication of polycrystalline perovskite thin films that is highly compact and with improved film coverage. A similar technique was developed for fabricating highly efficient perovskite light emitting diodes (LEDs), demonstrating the wide application of the solvent-engineering technique.[20]

Most recently, much of the effort have been focused on investigating the effect of the perovskite composition on the device performances (Figure 1-15a). For example, Jeon et al. showed successful stabilization of an α-phase $FAPbI_3$ perovskite, which is unstable but is ideal for solar cell application, by adding $MAPbBr_3$ as a stabilizaing agent. [8] This eliminated formation of detrimental δ-phase $FAPbI_3$ perovskite during device fabrication and resulted in efficiency exceeding 18%. In addition, Saliba et al. reported the benefit of introducing a small amount (~5 mol%) cesium (Cs) to the perovskite composition. The addition of Cs resulted in much improved device stability

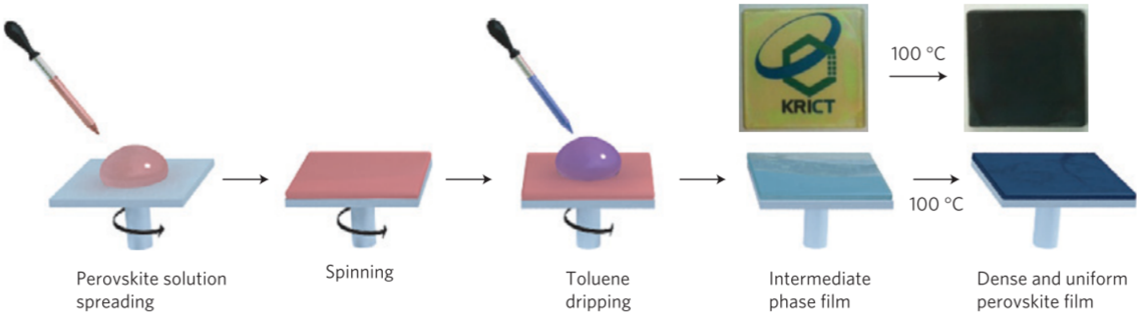

Figure 1-14: Schematic illustration of solvent-engineering. A non-solvent is introduced during spin coating process to induce formation of a perovskite intermediate phase, which is converted to a perovskite active layer upon thermal annealing. Adapted with permission from ref[7]. Copyright (2014) Springer Nature.

and was able to achieve efficiency up to ∼21%. [9]

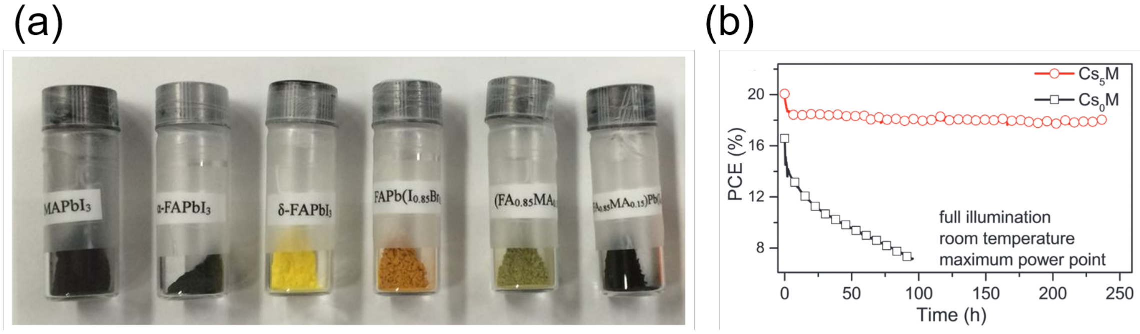

Figure 1-15: (a) Photograph of various lead halide perovskite powders. The right most sample, $(FAPbI_3)_{0.85}(MAPbBr_3)_{0.15}$, demonstrates the phase stabilizing effect of $MAPbBr_3$ for α-phase $FAPbI_3$ perovskite. Adapted with permission from ref[8] . Copyright (2015) Springer Nature. (b) Plot of PCE versus time for perovskite solar cell with and without Cs in its composition. The device with Cs exhibits higher efficiency and improved stability. Ref[9] - Published by The Royal Society of Chemistry.

1.2 What is the Ultimate Efficiency Limit in a Solar Cell?

1.2.1 Shockley-Queisser Efficiency Limit

A solar cell cannot convert 100% of the sun light into useful electricity. Rather, the theoretical maximum efficiency of a single junction solar cell is capped at ~33%. This theoretical limit of often referred to as the Shockley-Queisser (SQ) efficiency limit, based on their seminal work published in 1961.[21] In this chapter, I will go over the derivation of the SQ efficiency limit and the physical meanings behind it. For more detailed analysis and derivations, I recommend looking into the original work (Ref [21]) and Ref [22][23][24] as well.

The Ultimate Efficiency

Before SQ efficiency limit was derived, an empirical approach was used to calculate the theoretical maximum efficiency of a single junction solar cell by using values derived from experiments. SQ's approach was different in that they based the calculation on the thermodynamic principles and phenomenons, hence the "detailed balance limit". Detailed balanced means that the system is considered to be in an equilibrium system such as,

$$\mathrm{A} \underset{\mathrm{k_{BA}}}{\overset{\mathrm{k_{AB}}}{\rightleftharpoons}} \mathrm{B}$$

$$N_A k_{AB} = N_B k_{BA}$$

where A,B are the states, k is the rate between A and B, and N is the number of states.

To start simple, we set ourselves to find the maximum efficiency in the most ideal situation. The following assumptions describe the most ideal situation: 1) The sun has a temperature of 6000K and the solar cell has the temperature of 0K, 2) there is no flow of current through the device and there is only radiative recombination of carriers,

3) the solar cell looks like a donut that absorbs sun light from all direction, 4) the absorption profile is a step function where there is 100% absorption for photon with energy greater than the band gap (h$\nu > $ E$_g$), and one photon creates one electron-hole pair. Figure 1-16 shows how SQ depicted the ideal solar cell.

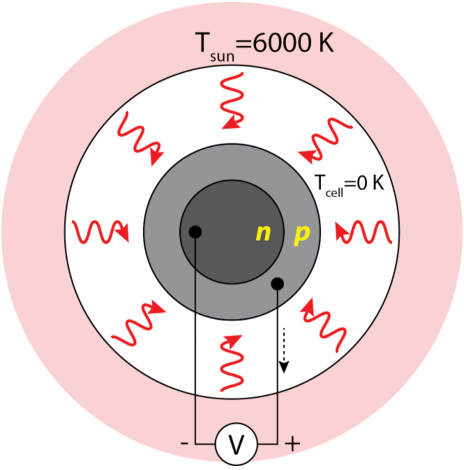

Figure 1-16: An ideal solar cell that is surrounded by a black body source (the sun) with the temperature of 6000K and the solar cell with the temperature of 0K.

We call the theoretical efficiency with the aforementioned assumptions as the "ultimate efficiency (u(E$_g$))" and it is,

$$u(E_g) = \frac{\text{output power}}{\text{input power}}$$

First we determine the output power of the ideal solar cell. Due to the assumptions, the ideal solar cell will absorb the black body radiation of the sun and emit photons corresponding to its band gap (E$_g$), Thus, the output power is,

$$\text{output power} = E_g \times \text{number of photons emitted}(Q_{sun})$$

Since the temperature of the cell is 0K and does not emit any black body radiation, the number of photons emitted is equal to the number of photons absorbed. The number of photons absorbed can be calculated by dividing the energy of the black body radiation of the sun as a function of the energy of the photon for photons with energy greater than the band gap,

$$Q_{sun} = Q(\nu, T_{sun}) = \frac{\text{Planck's Law}}{h\nu}$$
$$= \frac{\frac{2\pi h}{c^2} \int_{\nu_g}^{\infty} \frac{\nu^3}{e^{\frac{h\nu}{k_B T_{sun}}} - 1} d\nu}{h\nu}$$

where ν is the frequency of the light ($E_g = \frac{h\nu}{q}$), h is the Planck's constant, c is the speed of light in vacuum, k_B is the Boltzmann constant, T_{sun} is the temperature of the sun. The black body radiation of the sun is shown in Figure 1-17.

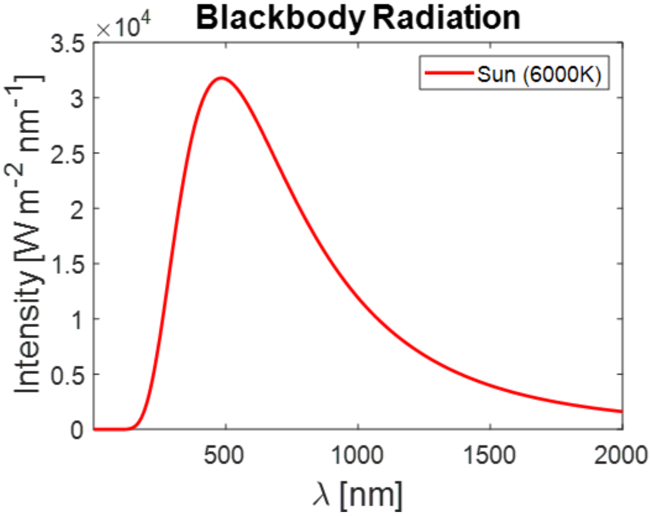

Figure 1-17: Plot of spectral irradiance versus wavelength for a black body radiation source with T=6000K.

Next, we determine the input power of the idea solar cell. The input power is simply the incident solar power (P_{sun}) and is the total energy of the black body radiation,

$$P_{sun} = \frac{2\pi h}{c^2} \int_{\nu_g}^{\infty} \frac{\nu^3}{e^{\frac{h\nu}{k_B T_{sun}}} - 1} d\nu$$

thus the ultimate efficiency $u(E_g)$ is,

$$u(E_g) = \frac{E_g \frac{2\pi}{c^2} \int_{\nu_g}^{\infty} \frac{\nu^2}{e^{\frac{h\nu}{k_B T_{sun}}} - 1} d\nu}{\frac{2\pi h}{c^2} \int_{\nu_g}^{\infty} \frac{\nu^3}{e^{\frac{h\nu}{k_B T_{sun}}} - 1} d\nu}$$

The plot of $u(E_g)$ versus the band gap (E_g) is shown as the red trace in Figure

1-18. Here, the maximum efficiency of ∼44% is achieved at the band gap of ∼1.1 eV.

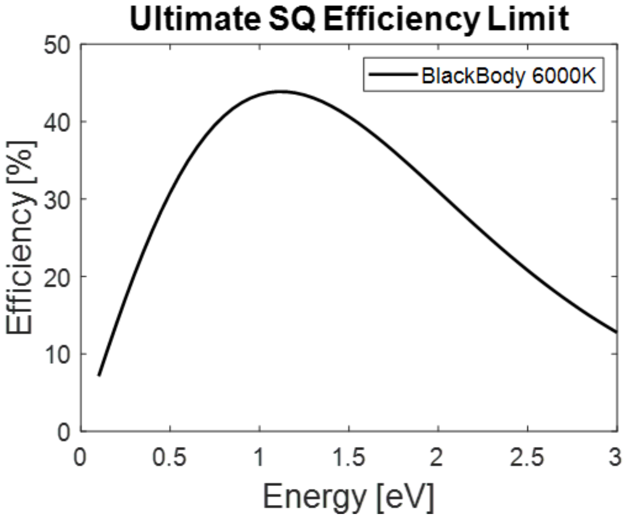

Figure 1-18: Plot of ultimate efficiency as a function of the band gap for an ideal solar cell.

The Nominal Efficiency

While the ultimate efficiency provides a good platform to understand how we should approach determining the maximum efficiency of a solar cell, some of the assumptions made to calculate the ultimate efficiency does not apply to real world applications.

First, while the temperature of the actual Sun is ~6000K, the observed solar spectrum from the Earth does not follow the black body radiation but rather a unique solar spectrum that is a combination of absorption from the atmosphere, scattering, and diffusion. Currently, the global standard for solar spectrum is Air Mass 1.5 Global, or AM 1.5G (Figure 1-19a). Air Mass is determined by the relative position between the Sun and the surface of the Earth. For example, A.M. 0 is defined as the solar spectrum outside of the Earth's atmosphere, whereas A.M. 1 is on the Earth's surface vertical from the Sun. In addition, depending on the relative angle, A.M. $\frac{1}{cos\theta}$ is determined. For example, A.M. 1.5 is for 48.2° relative from the axis. In addition to the relative angle, Direct and Global is distinguished (Figure 1-19b). Direct is considered as the straight ray, whereas Global considers diffused, scattered, and reflected light as well. Figure 1-20 shows three different solar spectrums: A.M. 0, A.M. 1.5 Direct, and A.M. 1.5 Global.

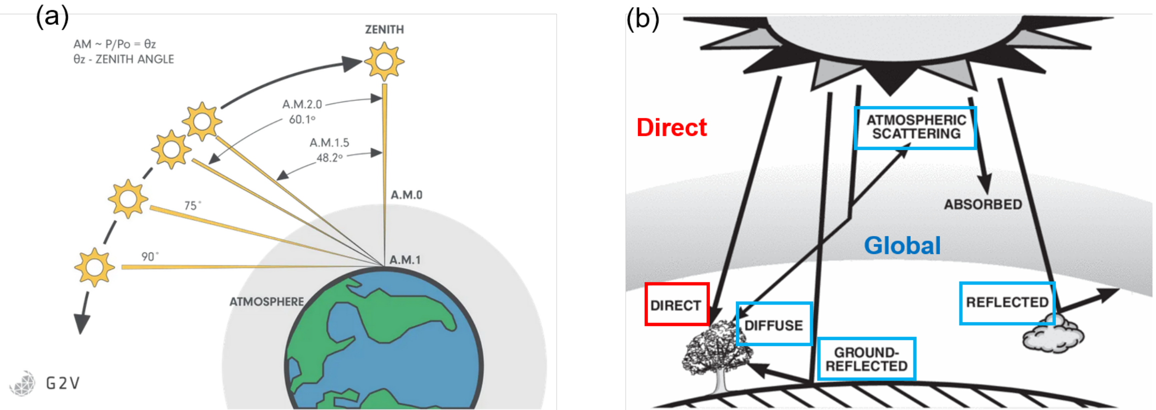

Source: G2V website

Source: Newport

Figure 1-19: (a) Illustration of various A.M. position. (b) Illustration describing the difference between Direct and Global.

By using the A.M. 1.5 G as the solar specturm, we can calculate the updated ultimate efficiency, u'(E_g)

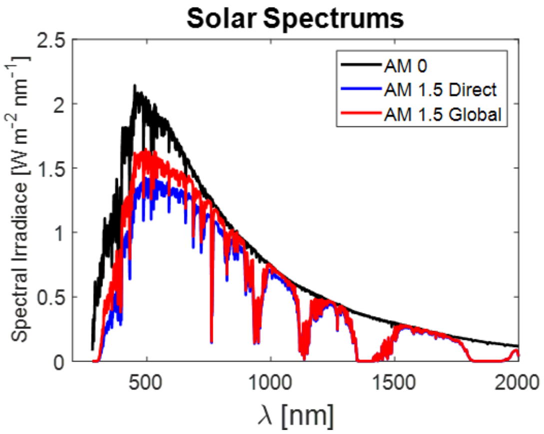

Figure 1-20: Plot of three different solar spectrum versus wavelength. A.M. 1.5 Global is considered as the standard reference spectrum for simulating the Sun's solar spectrum.

$$u'(E_g) = \frac{\text{output power}}{\text{input power}} = \frac{E_g \int_{\nu_g}^{\infty} \frac{\Phi_v^{A.M.1.5G}}{h\nu} d\nu}{\int_{\nu_g}^{\infty} \Phi_v^{A.M.1.5G} d\nu}$$

where $\Phi_v^{A.M.1.5G}$ is the A.M. 1.5 Global solar spectrum. Figure 1-21a shows the spectrum used for the initial ultimate efficiency and the updated ultimate efficiency using A.M. 1.5 Global as the solar spectrum. Figure 1-21b shows the calculated maximum efficiency for each band gap.

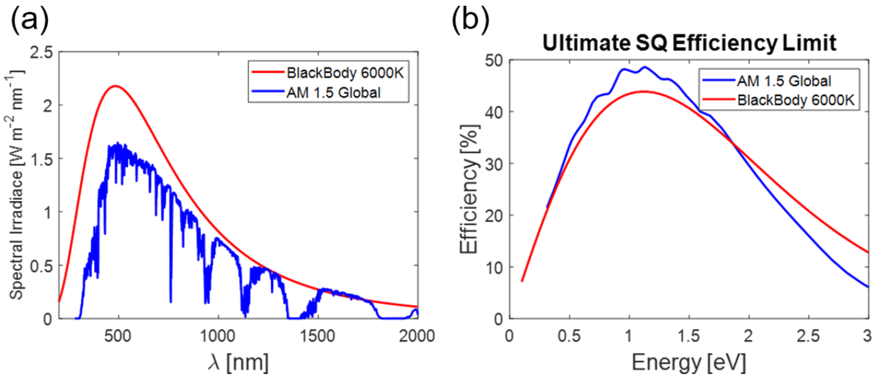

Figure 1-21: (a) Plot of solar spectrum from a black body source with T=6000K and an AM 1.5 Global spectrum. The concentration factor of 6.85e^{-5} is used for the black body radiation. (b) Plot of ultimate efficiency versus band gap using either black body source or the A.M. 1.5 Global solar spectrum.

Second, the initial ultimate efficiency assumes radiative recombination process is the only loss mechanism and that the cell's temperature is 0K. However, in an actual solar cell, carriers are extracted as a current through an external circuit and the cell's temperature is not 0K but can be considered as 300K. To consider the flow of current, we set a continuity equation where the generation of carriers is equal to the elimination of carriers at a given time.

$$0 = \text{Generation of carriers} - \text{elimination of carriers}$$

$$0 = G_{rs} + G_{re} - (R_r + I/q)$$

where G$_{rs}$ is the generation rate due to sun solar spectrum, G$_{re}$ is the generation rate due to the Earth's black body radiation, R$_r$ is the radiative recombination rate, and I/q is the flow of current. The mathematical expression for each rates are,

$$G_{rs} = \int_{E_g}^{\infty} EQE(E)\Phi_{Sun}^{AM1.5G} dE$$

$$G_{re} = \int_{E_g}^{\infty} EQE(E)\Phi_{Earth}^{BB} dE$$

$$R_r(V) = G_{re} e^{\frac{qV}{kT}}$$

In dark condition, G$_{rs}$ is zero, thus we can find the expression for I as,

$$\frac{I}{q} = G_{re} - R_r = G_{re}(1 - e^{\frac{qV}{kT}})$$

$$I_{dark} = qG_{re}(1 - e^{\frac{qV}{kT}}) = I_0(1 - e^{\frac{qV}{kT}})$$

To find the current (I),

$$I = I_{sc} + I_{dark} = I_{sc} + I_0(1 - e^{\frac{qV}{kT}}), I_{sc} = qG_{rs} = \int_{E_g}^{\infty} EQE(E)\Phi_{Sun}^{AM1.5G} dE$$

The plot of maximum short circuit current (J$_{SC}$) versus band gap is shown in

Figure 1-22 .

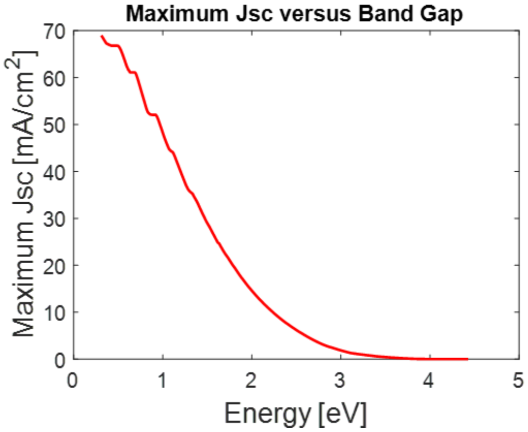

Figure 1-22: Plot of maximum short-circuit current density (J$_{SC}$) versus band gap.

To find the open-circuit voltage(V$_{OC}$), we set the current to zero,

$$I = I_{sc} + I_0(1 - e^{\frac{qV}{kT}})$$

$$0 = I_{sc} + I_0(1 - e^{\frac{qV_{OC}}{kT}})$$

$$V_{OC} = \frac{kT}{q} ln(\frac{I_{sc}}{I_0} + 1)$$

The plot of maximum open-circuit voltage (V$_{OC}$) versus band gap is shown in Figure 1-23 .

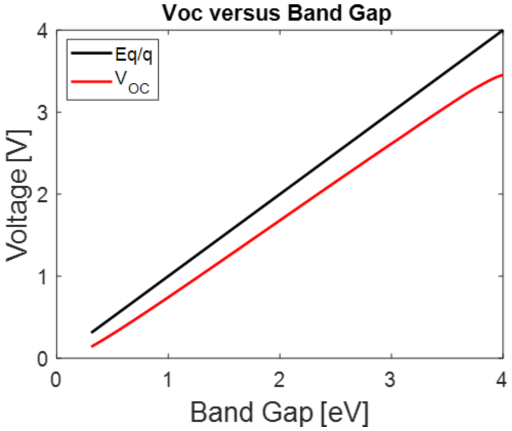

Figure 1-23: Plot of maximum open-circuit voltage (V$_{OC}$) and Eg/q versus band gap.

Lastly, we find the expression for the fill-factor (FF). FF is the ratio between

J$_{SC}$V$_{OC}$ and JmaxVmax, which generates the most power (Figure 1-24a),

$$FF = \frac{J_{max}V_{max}}{J_{OC}V_{OC}}$$

$$FF = \frac{d(JV)}{dV} = 0$$

$$\frac{d(JV)}{dV} = \frac{d[(J_{sc} + J_0(1 - e^{\frac{qV}{kT}}))]V}{dV} = J_0[e^{\frac{qV_{OC}}{kT}} - \frac{qV + kT}{kT}e^{\frac{qV}{kT}}] = 0$$

We find the solution to the equation above and set it to Vmax. Alternativley, a widely used empirical expression for the FF is,

$$FF = \frac{\frac{qV_{OC}}{kT} - ln(\frac{qV_{OC}}{kT} + 0.72)}{\frac{qV_{OC}}{kT} + 1}$$

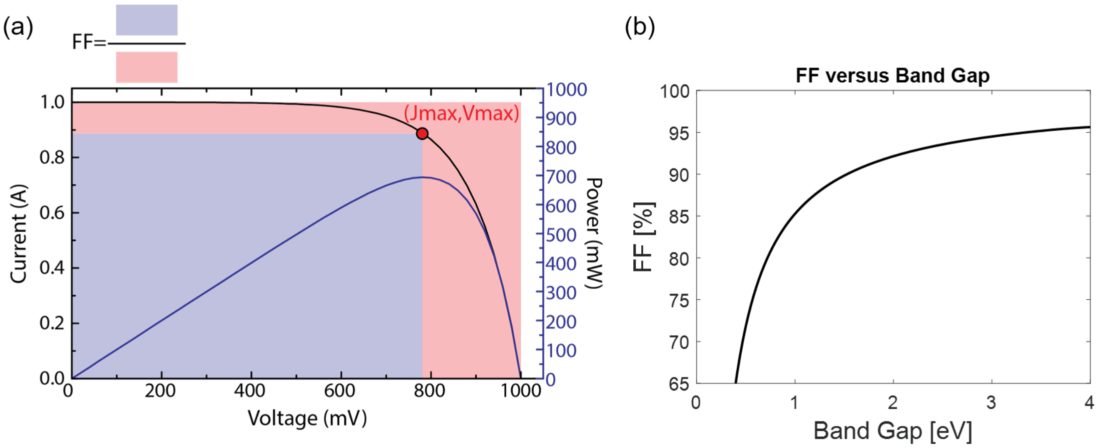

Figure 1-24: (a) A representative JV curve showing the expression for FF. The ratio between the large square (red) and the small square (blue) is the FF. (b) Plot of maximum fill-factor (FF) versus band gap.

Finally, we find the expression for power conversion efficiency (PCE), or the nominal efficiency,

$$PCE = \frac{J_{SC}V_{OC}FF}{\int_0^{\infty} \Phi_{Sun}^{AM1.5G} d\nu}$$

Figure 1-25 shows the plot of PCE versus band gap and the maximum PCE possible for Silicon, GaAs, and a perovskite solar cell.

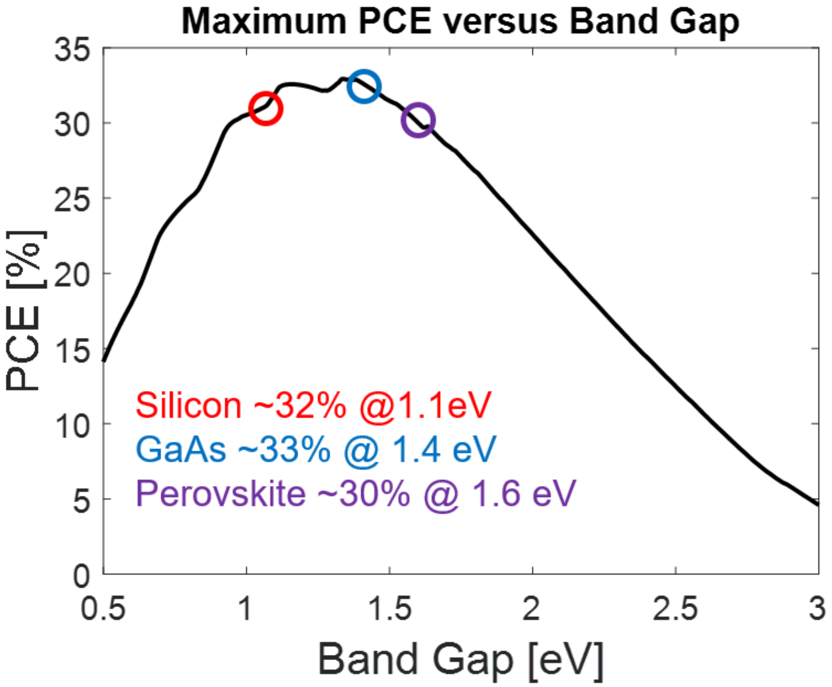

Figure 1-25: Plot of maximum PCE versus band gap. The band gap and maximum PCE possible for Silicon, GaAs, and perovskite (band gap 1.6 eV) is also shown.

Chapter 2

Perovskite Optoelectronics

2.1 Improved Perovskite Solar Cell Device Performance via Interface Passivation

The content of this chapter is published in Ref[25] and is adapted with permission from Ref [25]. Published by The Royal Society of Chemistry.

2.1.1 Why is Interface Passivation Important?

Perovskite solar cells (PSCs) have been intensively studied in the last few years due to their excellent photovoltaic performance and low fabrication costs.[26][27][28] Recent progress on stabilization of the crystal phase and defect management of inorganic/organic lead halide perovskites has resulted in devices with attractive power conversion efficiencies (PCEs). [8][29][9][30][31][32][33] Further improvements should be gained through interlayer/surface engineering to passivate interface defects, using metal oxides, polymers, small molecules, or organic halides.[34][35][36][37][38]

Interface passivation is highly common in semiconductor systems, where a specific treatment is applied to eliminate surface trap states that lead to non-radiative recombination of carriers and negatively affect the device performance and stability (Figure 2-1). For example, in the quantum dot community, it is often observed that core only nanocrystals exhibit poor photoluminescence quantum yield (PLQY), where PLQY is a metric that is used to determine how efficient the the emitter is at emitting a photon upon excitation. This is mostly due to exposed surface states that are prone to non-radiative recombination. By over-coating the core nanocrystal with an appropriate shell material, or with the addition of a suitable binding ligand, the PLQY and the photostability can be significantly improved.[39][29] In addition, in a solid-state semiconductor system, such as crystalline Silicon, an exposed Silicon surface exhibits many dangling bonds that can be passivated to improved device performances.[40]

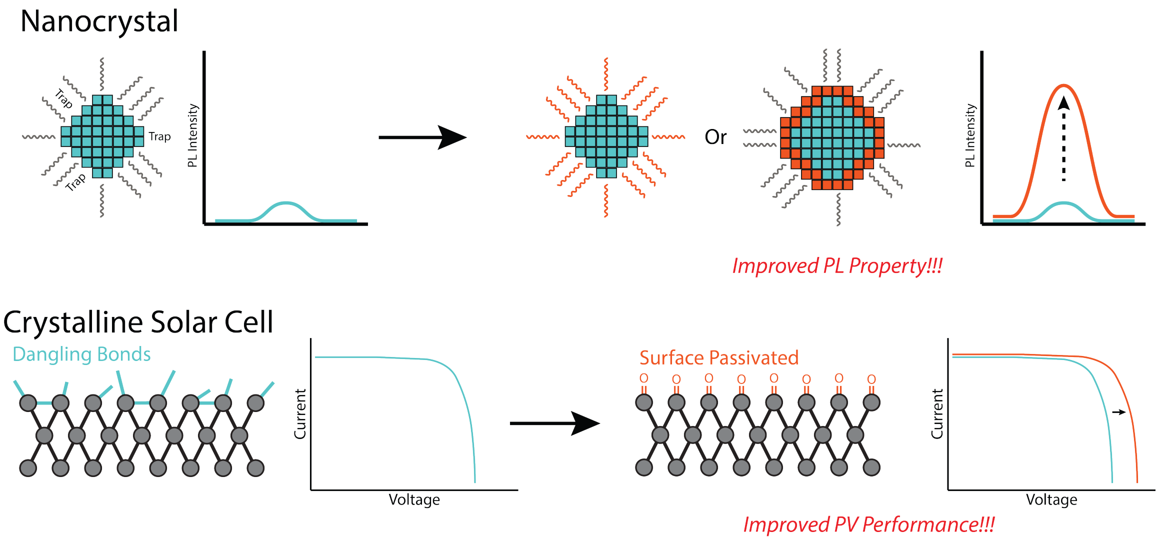

Figure 2-1: Schematic illustration of how surface or interface passivation can improve the optoelectronic properties of colloidal systems, such as nanocrystals, and solid-state systems, such as crystalline Si.

However, conventional surface treatment strategies geared at passivating interface defects have not demonstrated a performance exceeding that of PSCs fabricated simply from 3-dimensional (3D) perovskites. We show that this efficiency gap is due to the hidden role of the solvent that is used in conventional surface treatment method. [30][38][41] The use of an inappropriate solvent during surface treatment can negatively affect the underlying perovskite layer, preventing passivating agents from fulfilling their potential. The key challenge in the fabrication of interface passivated PSCs with high PCE and operational stability is to ensure that the underlying 3D perovskite layer remains pristine during surface treatment without negatively affecting its structure and properties.

In this chapter of the thesis, I report a selective precursor dissolution (SPD) strategy using a unique precursor/solvent combination (linear alkyl ammonium bromides/chloroform) for the effective synthesis of a 2D perovskite layer onto an underlying 3D perovskite thin film. Although the *in-situ* preparation of a 2D perovskite passivation layer on a 3D perovskite layer (thereby forming a 3D/2D heterostructure) has gained attention for its potential to effectively passivate interfaces and grain boundary defects, increase moisture resistance, and outperform state-of-the-art single layer 3D devices, [42] 3D/2D heterostructure devices have not yet delivered on their potential. Compared to previous (conventional) methods, the approach we have developed lead to the most effective synthesis of various 2D perovskite passivating layers onto 3D perovskite layers without disrupting the underlying 3D perovskite layer; a key for maximizing device performance and stability. The SPD strategy prolongs carrier lifetime through defect passivation and improves the open circuit voltage (V_{OC}). Through this strategy, we obtain a champion device with a PCE of 23.4% from a reverse current-voltage (J-V) sweep with a certified stabilized PCE (measured under stabilized conditions for ∼31min.) of 22.6% – the highest stabilized and certified PCE reported for PSCs at the time – with a V_{OC} loss of only ∼340 mV, which was the lowest V_{OC} loss reported at the time, and with enhanced operational stability. In addition, our PSC shows an electroluminescence (EL) external quantum efficiency (EQE) of up to 8.9%, which was the highest value reported from a PSC at the time.

2.1.2 Novel Interface Passivation: Selective Precursor Dissolution (SPD) Strategy

Isopropyl alcohol (IPA) is the most popular solvent used in conventional methods for post-processing of perovskite thin films for surface passivation. To understand the effect of this solvent on the underlying perovskite thin film during surface treatment, we compared the solubility of perovskite precursors in IPA relative to a solvent commonly used as a non-solvent; chloroform (CF). IPA effectively dissolves formamidinium iodide (FAI) due to its highly polar nature and its ability to form hydrogen bonds (Figure 2-2). In contrast, CF, a solvent frequently used as the anti-solvent, shows very limited solubility towards FAI (<1 mg/mL). The effect of solvent on the perovskite is further explored in grazing incident X-ray diffraction (GIXRD), where the 3D perovskite thin film, with the composition $(FAPbI_3)_{0.92}(MAPbBr_3)_{0.08}$ 3D perovskite where MA is methylammonium, is treated with either neat IPA or neat CF (control is without any solvent treatment) (Figure 2-2).

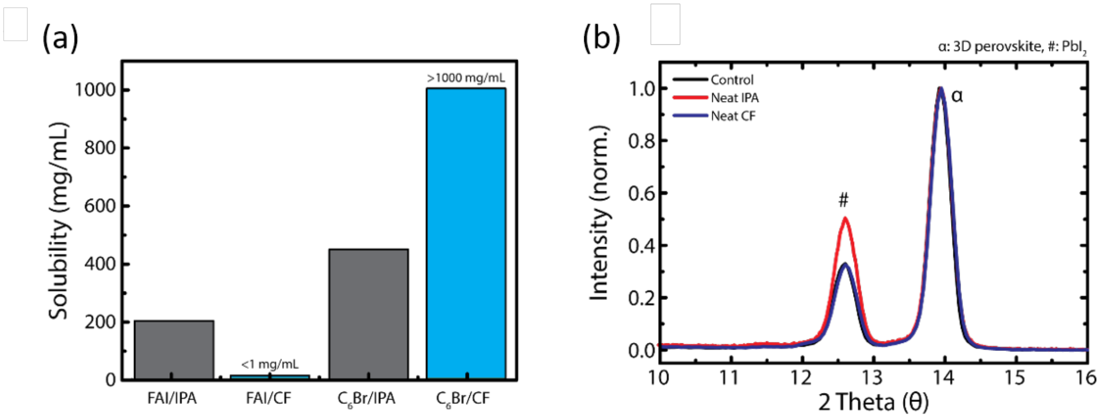

Figure 2-2: a, Solubility of FAI and C_6Br in CF and IPA illustrating the appropriateness of using CF for the 2D perovskite treatment. b, Grazing indicent XRD (GIXRD) of 3D perovskite treated without any solvent (control) ,with neat IPA, or with neat CF.

Compared to the control, the neat IPA treated perovskite film shows a PbI_2 rich surface, likely due to the dissolution and/or decomposition of the ammonium halide salt (Figure 2-2b). In contrast, no visible change is observed for neat CF treated sample. The solubility of n-hexylammonium bromide (C_6Br), a passivating agent used for *in-situ* synthesis of 2D perovskite passivating layer, shows the opposite trend where C_6Br shows higher solubility in CF than in IPA (Figure 2-2a). Interestingly, other commonly used anti-solvents (chlorobenzene, 1,2-dichlorobenzene, and toluene) did not dissolve the passivating agent and cannot be used during surface passivation. (Figure 2-3a). In addition, we tried to dissolve phenylammonium and benzylammonium halides which are mainly used for passivating agents, but these types of ammonium halides were not soluble in CF. Only a unique combination of the linear alkyl ammonium bromide based 2D perovskite precursors and a specific non-solvent (CF) resulted in a passivating solution that can deliver high quality 2D perovskite layers onto 3D perovskites without negatively affecting the underlying 3D perovskite layer.

To further analyze the effect of solvent on 3D perovskite thin films, we compared carrier lifetimes for 3D perovskite films exposed to neat IPA or CF under various conditions (Figure 2-4). 3D perovskite thin films show slightly reduced carrier lifetimes when exposed to neat IPA for a short time period ($<$2sec for typical spin-coating method) in an inert environment compared to neat CF. In fact, a bigger difference in the carrier lifetime is observed when the experiment is carried out in an ambient condition (relative humidity $\sim$30%). In addition, to closely simulate scaled-up fabrication of PSCs where spin coating deposition methods are not feasible, the 3D perovskite films were dipped in an IPA or CF containing C_6Br in an ambient condition (relative humidity $\sim$30%).

The 3D perovskite substrate dipped in a n-hexylammonium bromide (C_6Br) containing IPA (2D/IPA) solution shows significantly reduced carrier lifetimes, likely due to the hygroscopic nature of the solvent as well as the detrimental effect protic polar solvents have on the perovskite film (Figure 2-3b). Together with the use of polar solvents, hygroscopic solvents are a critical issue for the scaled-up production of PSCs under ambient conditions. The difference between hygroscopic IPA and non-hygroscopic CF on 3D perovskite films is demonstrated in Figure 2-4.

The 3D perovskite thin film exposed to neat IPA shows an increase in its absorption baseline above $\sim$800 nm and decreasing relative absorbance below $\sim$550 nm

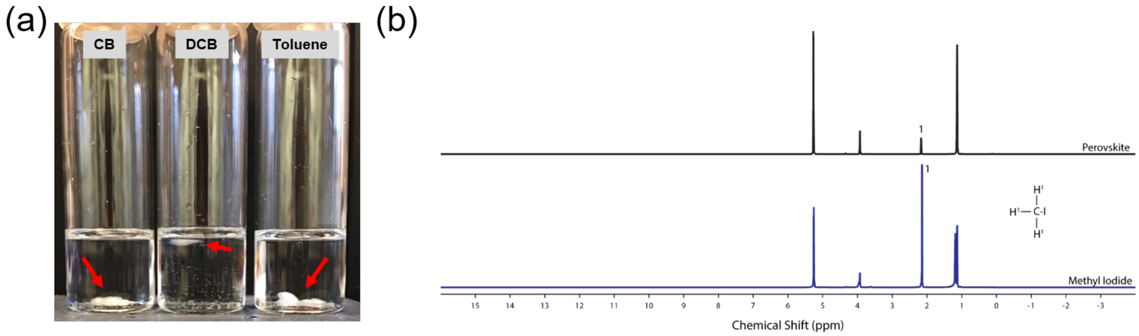

Figure 2-3: a, Photograph of vials containing the 2D perovskite precursor C_6Br in chlorobenzene (CB), 1,2-dichlorobenzene (DCB), and toluene. The precursor concentration is 2.5 mg/mL. The red arrows points to insoluble precursor powder. b, 1H NMR of 3D perovskite dipped in deuterated IPA and methyl iodide in deuterated IPA. When the 3D perovskite is exposed to IPA, the methylammonium iodide decomposes to methyl iodide and ammonia. The methyl iodide peak is visible at ~2.1 ppm in perovskite sample. The peak at ~5.2 ppm is water and peaks at ~3.8 and ~1.1ppm is IPA peak.

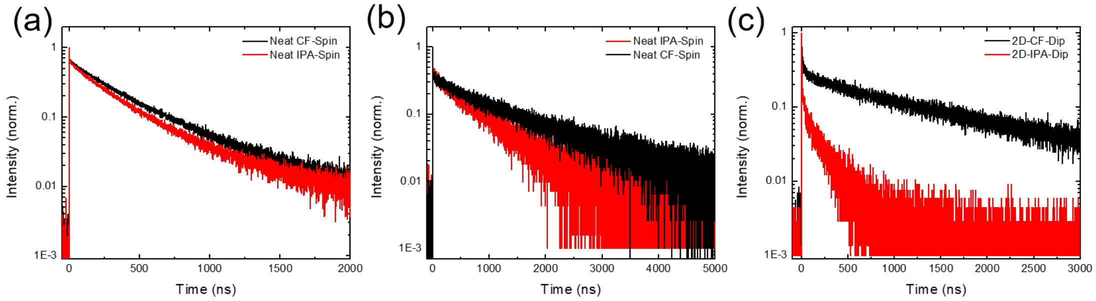

Figure 2-4: a-c, Lifetime traces of perovskite substrate fabricated inside the glovebox with treatment with neat IPA and CF (a), fabricated in ambient condition with treatment with neat IPA and CF (b) and 2D perovskite precursor containing IPA and CF (c).

as a function of time (0-90min) (Figure 2-5a). These changes in optical profile are likely due to changes in the perovskite crystal structure, increasing light scattering, and bleaching of the 3D perovskite film. In contrast, the 3D perovskite thin film submerged in CF shows no change in optical profile even after 90 minutes. The long-term effect of IPA and CF is demonstrated in Figure 2-5b where a perovskite powder and thin film are exposed to IPA and CF overnight in air. Both the perovskite powder and the thin film exposed to IPA show severe perovskite bleaching and decomposition whereas the samples retain their color when submerged in CF. CF is immiscible with water, which suggests CF is an ideal solvent system for post-processing perovskite thin films under ambient conditions.

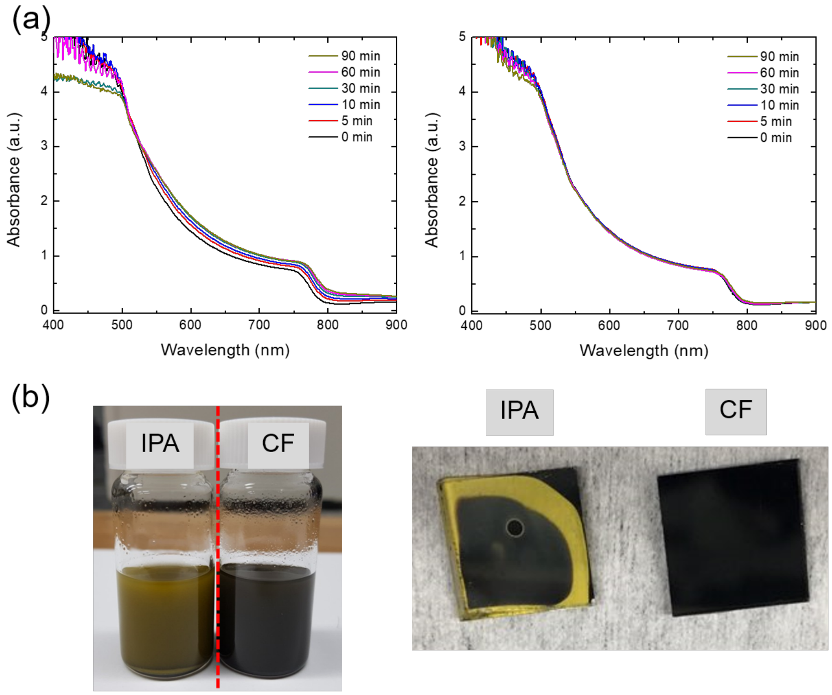

Figure 2-5: a, UVVis of 3D perovskite dipped in IPA (left) and CF (right). The UVVis of perovskite substrate dipped in IPA shows higher scattering background due to roughening of the surface and reduced relative absorbance in the ~500 nm region due to perovskite bleaching or destabilized crystal phase. However, no change in optical response for CF is observed. The experiment was carried in air. b, Photograph of perovskite powder (left) and thin film (right) exposed to IPA or CF in air overnight. IPA causes perovskite bleaching whereas CF does not affect the perovskite samples.

To confirm the negative effect of IPA and the inertness of CF on device performance, 3D PSCs were fabricated by treating the 3D perovskite active layer with either neat IPA or CF. The neat IPA treated PSCs show lower PCEs on average and a wider PCE distribution compared to devices treated with CF, and faster degradation is observed for neat IPA treated PSC under MPP (Figure 2-6). Moreover, devices based on 3D perovskite films exposed to CF overnight retain their high efficiencies (Figure 2-6c) whereas this could not have been possible with PSCs exposed to IPA.

Based on the results above, we expect an improved 3D perovskite interface when using CF during the *in-situ* synthesis of a 2D perovskite passivating layer. Figure

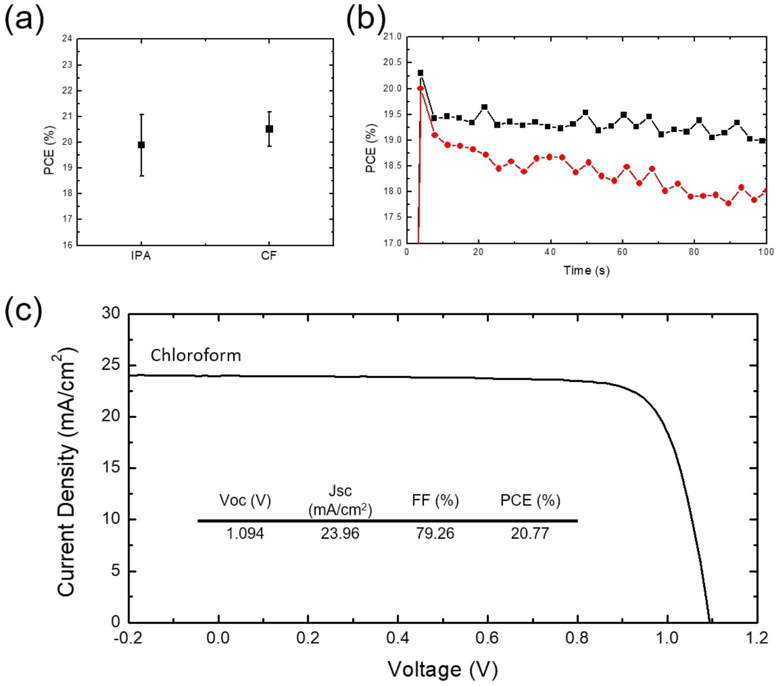

Figure 2-6: a,b, PCE (a) and MPP (b) on PSC fabricated with neat IPA or CF treatment. The neat IPA (red trace) treated PSC results in lower efficiency and faster degradation under MPP condition. c, J-V curve and device performance of PSC fabricated by soaking in CF overnight in air prior to hole transport layer and Au deposition.

2-7a shows XRD results for the 3D perovskite, the 3D perovskite treated with the 2D perovskite with CF or IPA as solvents and C_6Br as the 2D precursor (3D/2D (SPD strategy)) or 3D/2D (Conventional)), and pristine 2D perovskites. Compared to the 3D perovskite, 3D/2D perovskites with C_6Br treatment have additional peaks at 3.9°, 7.9°, and 11.9° (marked with *) and show a lower peak intensity for the PbI_2 peak (marked with #), indicating the incorporation of near-surface PbI_2 into the 2D perovskite during the *in-situ* synthesis of the 2D perovskite. When comparing XRD peaks from pristine 2D perovskite films, the 2D perovskite peaks from 3D/2D structures matches well with the Ruddlesden–Popper hybrid perovskite $(C_6H_{13}NH_3)_2(FA)Pb_2Br_2I_5$ compared to a pure 2D perovskite, $(C_6H_{13}NH_3)_2PbBr_2I_2$.The slight shift in the lower angle peaks can be attributed to varying cation or halide stoichiometries, and/or different thicknesses for the crystal layers in the 2D perovskite (the n value). [43][44][45] In addition, the 2D perovskite peak intensities from 3D/2D perovskites fabricated using CF (3D/2D (SPD strategy)) are noticeably stronger than those from 3D/2D perovskites fabricated using IPA (3D/2D (Conventional)), and show a lower signal intensity from PbI_2.

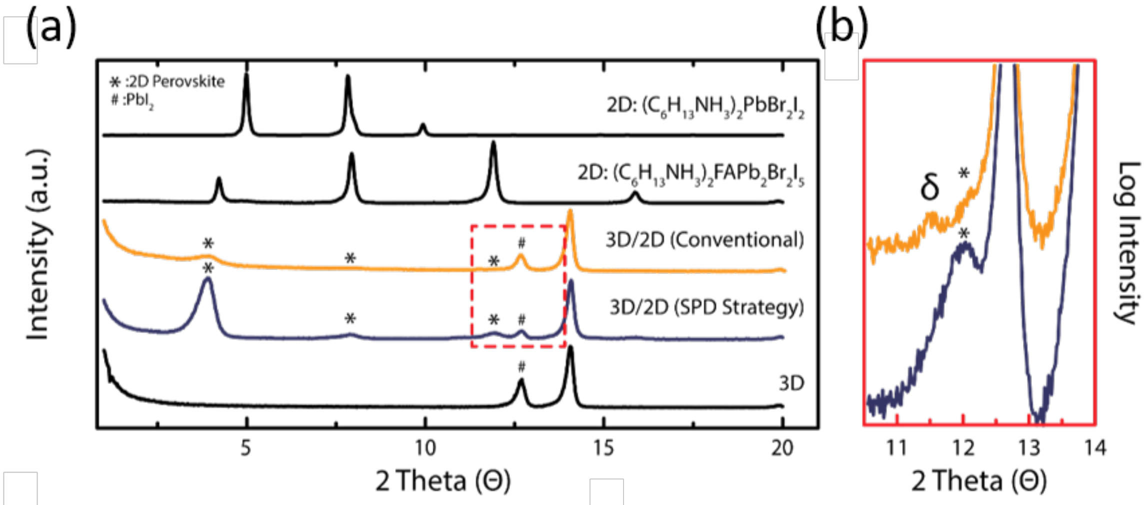

Figure 2-7: a, GIXRD of 3D and 3D/2D perovskites fabricated using IPA (Conventional) or CF (SPD Strategy), and XRD of pristine 2D perovskite with different compositions. * corresponds to the 2D perovskite diffraction peak. b, XRD of the 3D/2D (Conventional) and 3D/2D (SPD Strategy) perovskites showing the formation of the δ-phase ($\sim$11.5°) in 3D/2D (Conventional) perovskites. δ corresponds to the 2D perovskite diffraction peak.

Additionally, scanning electron microscope (SEM) images show less faceted and less distinctive grain surfaces and grain boundaries for the 3D/2D (SPD strategy) film compared to the 3D perovskite (3D control) and the 3D/2D (Conventional) films (Figure 2-8). Generally, various properties of the solvent, such as its dielectric constant and the solubility of precursors, strongly affect reactivity during material synthesis. The use of CF, which has lower dielectric constant and a higher solubility for linear alkyl ammonium bromides than IPA, can increase the reactivity between the surface of 3D perovskites and linear alkyl ammonium bromides, and thus lead to the *in-situ* formation of a highly crystalline 2D perovskite onto 3D perovskite films.

Furthermore, XRD measurements reveal formation of non-perovskite polymorphs of $FAPbI_3$ (δ-phase) for 3D/2D (Conventional) films. Highly polar and hygroscopic IPA may destabilize the 3D perovskite surface layer by removing MA/FA halides

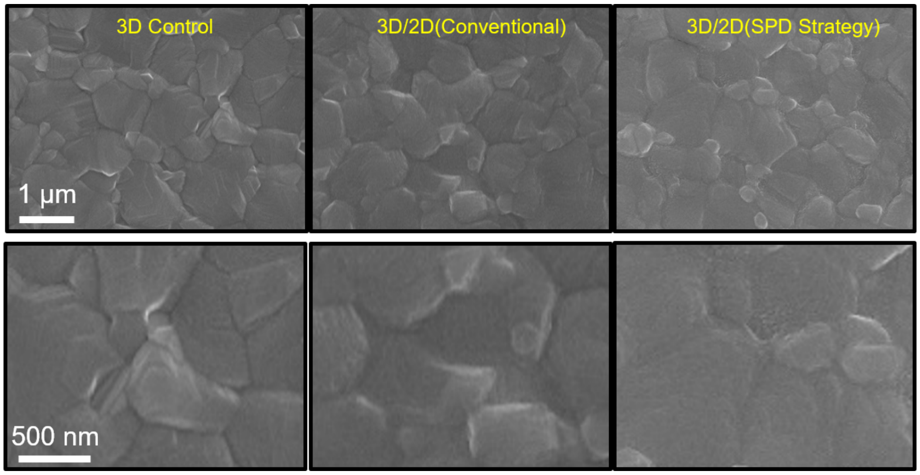

Figure 2-8: Planar SEM images of 3D, 3D/2D (IPA), and 3D/2D (CF) perovskites where C_6Br was used for the 2D perovskite. The grain boundary is most distinct for the 3D perovskite and least distinct for 3D/2D (CF) perovskite.

and altering the chemical composition and structure at the 3D/2D interface (Figure 2-7b). The δ-phase has been correlated to lower device performance and operational stability and should be avoided for optimal device performance. [46] Additionally, 3D perovskite films exposed to an IPA passivating solution (containing the 2D perovskite precursors) beyond conventional spin-coating times (>2 seconds) show inhomogeneous film formation with visible pin-holes (Figure 2-9). In contrast, the SPD strategy results in uniform deposition of the 2D perovskite passivating layer. The SPD strategy allows for a wide processing window, an important factor in the potential scaled-up fabrication of perovskite photovoltaics. [47]

Comparisons of device efficiency/stability demonstrate the impact of the SPD strategy. Figure 2-10a shows J-V curves of representative 3D/2D PSCs fabricated using the conventional method (IPA) or the SPD strategy (CF). Prepared under similar conditions and at the same time, a conventional 3D/2D PSC shows an open-circuit voltage (V_{OC}) of 1.14 V, current density (J_{SC}) of 23.9 mA/cm^2, fill factor (FF) of 78.2% and a PCE of 21.3%, which is comparable to previously reported defect-passivated PSC, [48][42] while the SPD strategy using CF shows an increased device performance, achieving a V_{OC} of 1.16 V, J_{SC} of 24 mA/cm^2, FF of 80% and a PCE of 22.3%. In addition, when the J-V scan is repeatedly performed under contin-

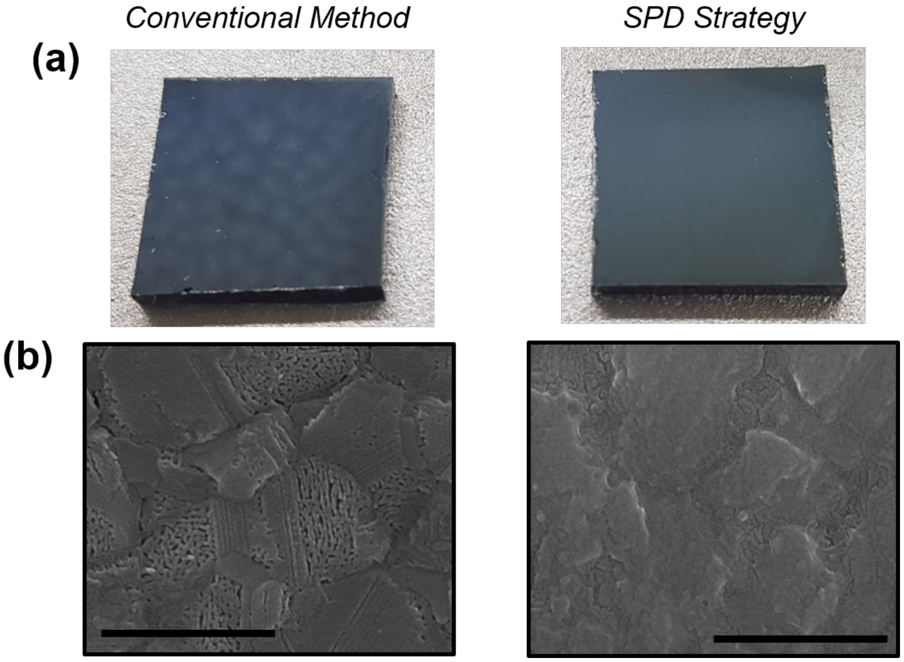

Figure 2-9: a,b, Photograph (a) and SEM image (b) of 3D/2D perovskite substrates fabricated using conventional method or SPD strategy. The conventional method results in 3D/2D perovskite film with incomplete film formation with pin holes whereas the SPD Strategy results in film with homogeneous 2D perovskite coverage. Scale bar is 1 μm.

uous light illumination, putting the PSCs under operational stress, the SPD strategy based 3D/2D PSCs shows superior stability over conventional 3D/2D PSCs (Figure 2-10b). These results indicate that the SPD strategy using CF as a solvent maximizes the effect of the 2D perovskite treatment, leading to effective defect passivation and improved device performance.

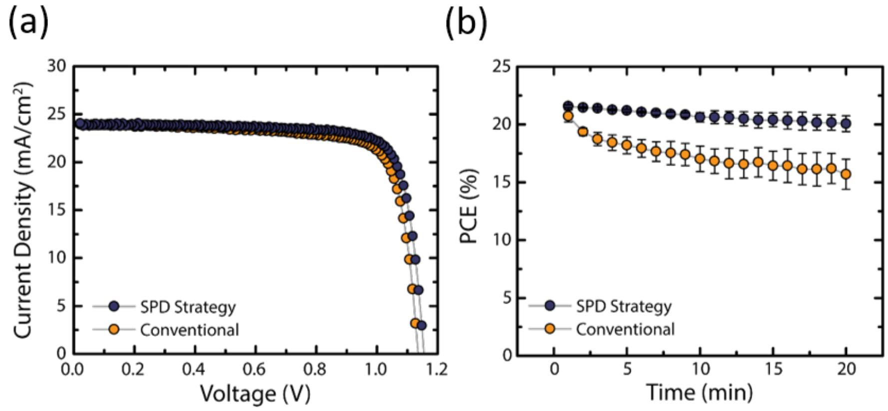

Figure 2-10: a, J-V curve of 3D/2D (Conventional) and 3D/2D (SPD Strategy) PSCs. b, Light stability test of 3D/2D (Conventional) and 3D/2D (SPD Strategy) PSCs showing higher device performance and stability for 3D/2D (SPD Strategy) PSCs.

2.1.3 Effect of alkyl chain length on 3D/2D perovskite thin film properties and device performance

Our solubility and XRD results above support the use of CF instead of IPA during 2D perovskite treatment, leading to PSCs with higher performance and greater stability. We further incorporated three different 2D perovskites with varying carbon chain lengths on 3D perovskite films: n-Butylammonium bromide (C_4Br), C_6Br, and n-Octylammonium bromide (C_8Br), as the alkyl chain length in 2D perovskite structures has been previously shown to affect defect passivation and thus device performance.[49][37][45]

Figure 2-11a shows the 2-dimentional XRD (XRD^2) pattern of 3D and 3D/2D perovskites with varying alkyl chain lengths (C_4Br, C_6Br, and C_8Br).[16] Upon 2D perovskite treatment, a peak appears at $\sim 4^\circ$ (white arrow), shifting to lower angle with increasing chain length due to their larger organic spacing, as has been previously been observed (Figure 2-12a). [44] The single confined spot on the diffraction ring in the XRD^2 pattern for all three 2D perovskites indicates a planar (001) orientation relative to the underlying 3D structure. Although the 2D perovskite layer on the 3D perovskites is too thin for a quantitative determination of its thickness, GIXRD shows a decrease in the 2D perovskite peak and an increase in PbI_2 and 3D perovskite peaks at relatively low incident angles (0.2-1θ), indicating that the 2D perovskite is limited to the very surface of the film (Figure 2-12b).

Morphological changes on the perovskite surface investigated using planar SEM show that 3D/2D perovskites have noticeably less defined grain boundaries compared to the 3D control; increasing the alkyl chain length leads to less visible perovskite grain boundaries. This is consistent with a thin 2D perovskite layer on top of the 3D perovskite film and the filling of grain boundaries. A reduced surface roughness is also demonstrated using atomic force microscopy (AFM) (Figure 2-13a).

The effect of the 2D perovskite layer on the passivation of surface and grain boundary defects was investigated using Kelvin probe force microscopy (KPFM) by measuring the contact potential difference (CPD) between the AFM tip and the sample

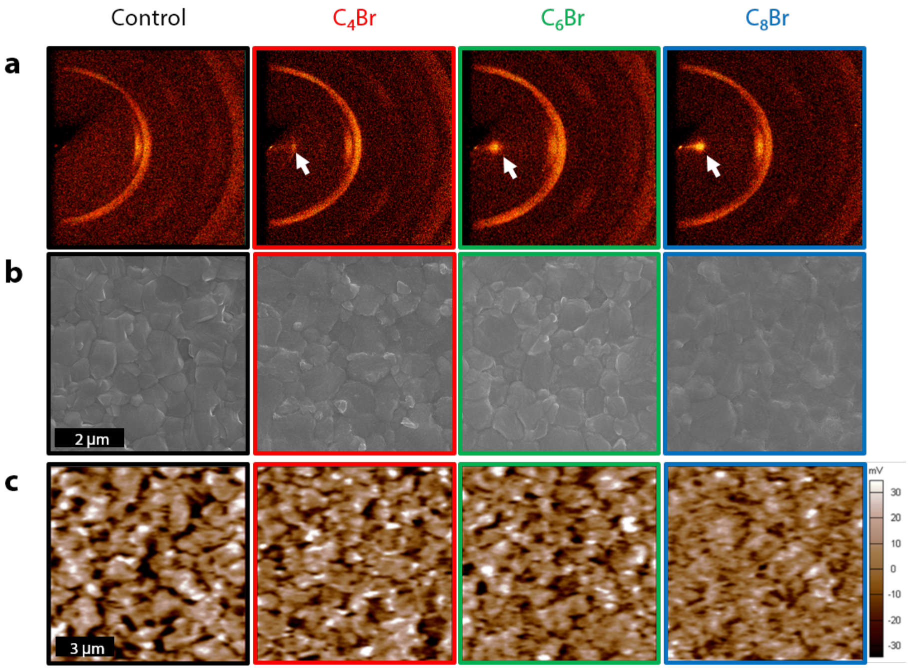

Figure 2-11: a, XRD^2 image of 3D control and three different 3D/2D (C_4Br, C_6Br, C_8Br) perovskites fabricated using the SPD strategy. White arrows indicate the (001) peak of the 2D perovskite. b, Planar SEM of 3D control and 3D/2D perovskite samples. c, KPFM images of 3D control and 3D/2D perovskite samples. SEM images show that the grain boundary is less distinct for the 3D/2D perovskite and the same behavior is observed in potential mapping from KPFM.

surface (Figure 2-11c). [50][51][52][53] Remarkably, upon 2D perovskite treatment, the perovskite films show a significant flattening of the potential distribution suggesting that alkylammonium based 2D perovskite interlayers are effective at passivating surface/grain boundary traps (Figure 2-13b). [51][52]

Additionally, time-resolved photoluminescence (TRPL), used to measure carrier lifetimes for 3D control and 3D/2D perovskites (Figure 2-14) shows an increase in carrier lifetime for all three 3D/2D perovskite samples compared to the 3D control. UPS and TRPL measurements indicate that the wide band gap 2D perovskite prevents carrier quenching (Figure 2-15, 2-16). 2D perovskite treatment is effective in passivating surface/grain boundaries, reducing non-radiative recombination pathways.

The band diagrams depicted in Figure 2-16c-f to provide an explanation of the observed kinetics in the TRPL traces and the observed increased device performance. The 3D-control structure (Figure 2-16c) depicts the band diagram and the observed

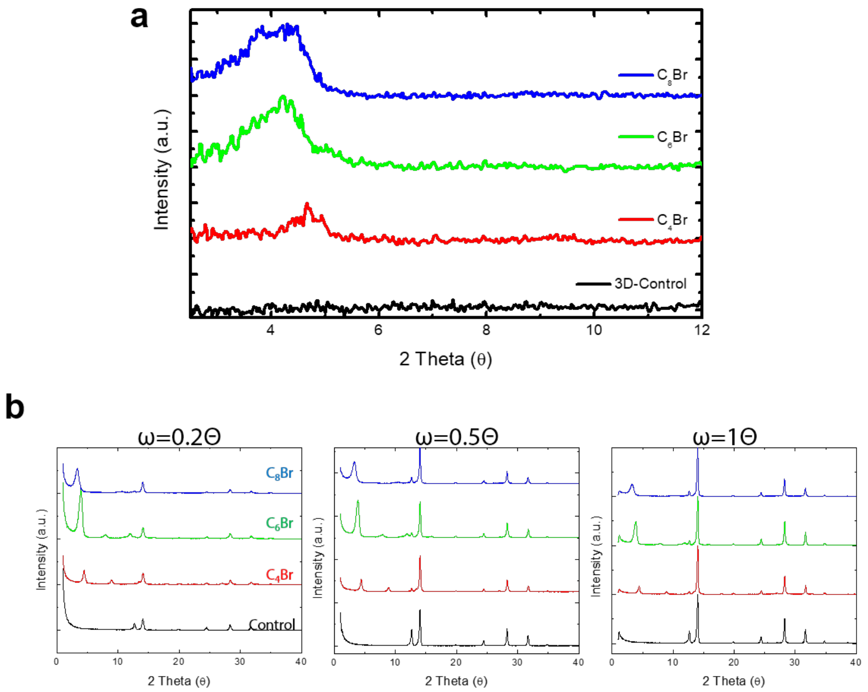

Figure 2-12: (a) The XRD^2 shows the main 2D perovskite peak shifting to lower angles with increasing alkyl chain length. b, GIXRD pattern at various incident angle (ω) on the 3D perovskite and 3D/2D perovskites with different alkyl chain length.

recombination pathways based on TRPL measurements. The observed radiative rate, k_R(3D), is faster than the known intrinsic carrier lifetime in 3D perovskite thin films, likely due to the presence of non-radiative recombination pathways, $k_N R$(3D), associated with the surface. When a 2D layer is deposited on the 3D perovskite (Figure 2-16d), TRPL measurements observed with excitation from the 3D perovskite side show an increase in carrier lifetimes, k_R1(3D/2D), compared to the 3D control perovskite. On the other hand, the lifetime trace shows a relatively fast component, k_R2(3D/2D), when the 3D/2D perovskite is excited from the 2D perovskite side, in addition to the long component (Figure 2.2-14a). This behavior of different lifetime profiles depending on the excitation side is not observed in the 3D control perovskite where the lifetime traces are almost identical for both film and substrate excitation.

We identify the 2D perovskite interlayer as a passivating layer that minimizes surface/interface trap states that otherwise would serve as non-radiative recombination centers. The additional passivation results in an increase in carrier lifetimes and

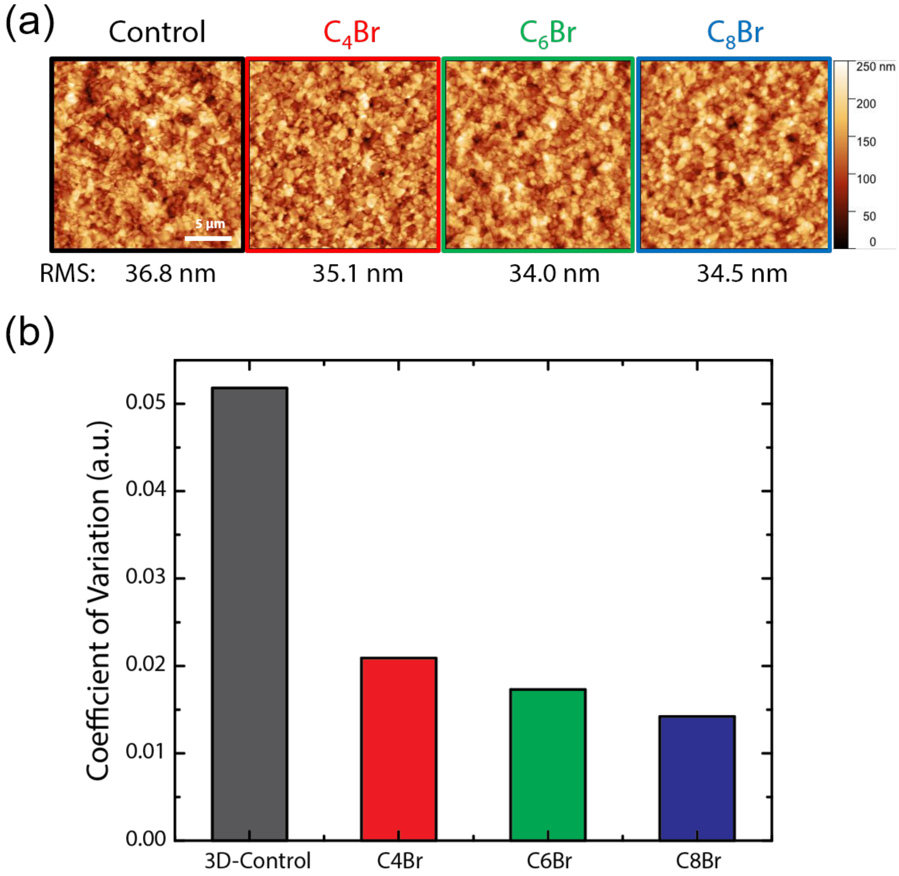

Figure 2-13: a, AFM images of 3D (Control) and 3D/2D (C_4Br, C_6Br, C_8Br) perovskites and their surface roughness shown in RMS value. Surface roughness decreases upon 2D perovskite treatment. b, Coefficient of variation, defined as the standard deviation of the CPD intensity normalized to the average CPD intensity, calculated from KPFM images in Figure 2c.

the increase in detected photons. Furthermore, we hypothesize that the fast radiative component, k_R2(3D/2D), is due to a carrier buildup at the 3D/2D perovskite interface from band bending, which is supported by the UPS results. This carrier accumulation can contribute to the increase of V_{OC} of 3D/2D PSCs, in addition to the increase in the built-in potential due to the higher work function of 3D/2D perovskite.

Our hypothesis on the role of 2D perovskites on the 3D/2D perovskite structure is further supported by TRPL measurement with the addition of hole transport layers (HTL), specifically Spiro-OMeTAD. Figure 2-16e-f shows the band diagram of 3D/HTL and the 3D/2D/HTL structure and Figure 2.2-14d-e shows the correspond-

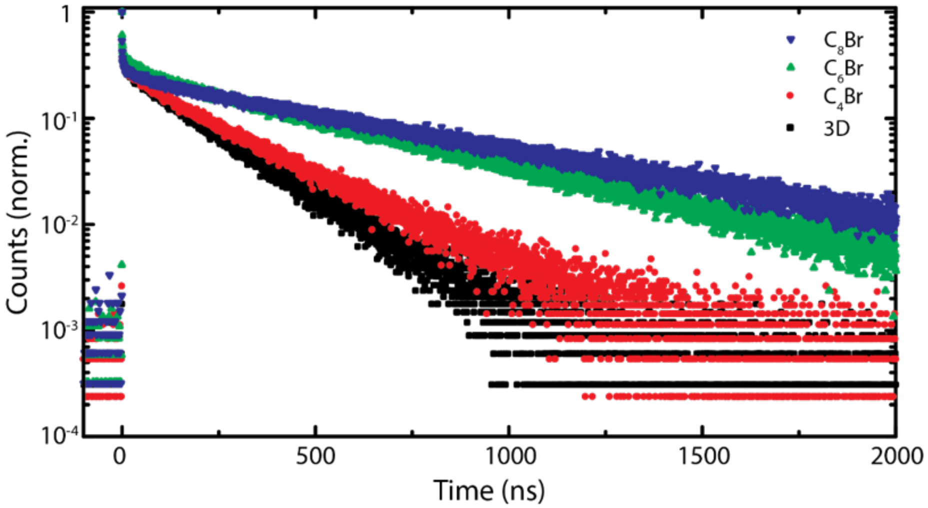

Figure 2-14: TRPL trace of 3D and 3D/2D perovskite films deposited on a quartz substrate. The sample was excited through the quartz substrate. An increase in the carrier lifetime is observed with 2D perovskite treatment

ing lifetime traces, carrier lifetime, and photon counts. The 3D/HTL structure shows significantly faster lifetime traces when compared to pristine 3D perovskites, due to quenching of one of the carriers (hole) into the HTL. On the other hand, a longer lifetime is observed for the 3D/2D/HTL structure compared to 3D/HTL. The limited quenching effect can be explained by the reduced recombination between the electron in the perovskite layer and the hole in the HTL due to the spatial separation and the energy barrier provided by the wide band gap 2D perovskite.

In total, the 2D perovskite interlayer passivates the 3D perovskite surface traps and minimizes nonradiative recombination pathways, while providing a spatial separation and an energy barrier to minimize carrier quenching associated with the 3D perovskite/HTL interface. In eliminating intra-band gap states and removing nonradiative recombination pathways, the 2D perovskite interlayer provides an ideal interface for low V_{OC} loss and improved PCE.

We fabricated PSCs without (3D control) and with various 2D perovskite precursors (C_4Br, C_6Br and C_8Br) using the SPD strategy to show that the improved optoelectronic properties translate to better performing devices. Figure 2-17a shows a schematic illustration of the 3D/2D PSC along with a false colored cross-sectional

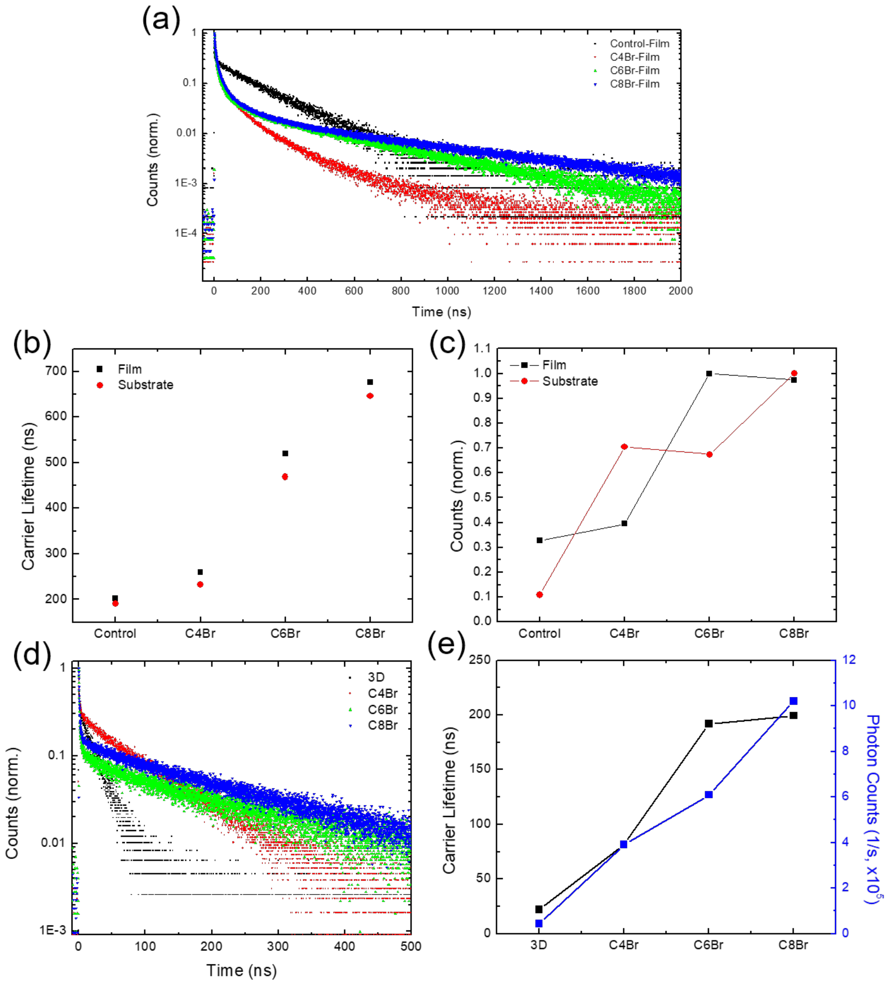

Figure 2-15: a, TRPL traces of 3D and 3D/2D perovskites on quartz substrates. "Film" indicates that the sample is excited from the perovskite film side. b, Carrier lifetimes extracted by fitting the long component of the lifetime traces (a above as well as from Figure 2d). "Substrate" indicates that the sample is excited through the quartz substrate (in Figure 2d). c, Normalized integrated photon counts from the TRPL measurements. d, TRPL of 3D and 3D/2D perovskite samples with Spiro-OMeTAD as the hole transport layer, excited from the perovskite film side. e, Extracted carrier lifetimes and integrated photon counts (from d).

SEM image. Figure 2-17b shows the average J-V curves of the fabricated 3D control and SPD strategy based 3D/2D PSCs. The average PCEs for 3D/2D devices are noticeably higher than the control (∼22% vs ∼20.5%) with reduced hysteresis in the J-V curves regardless of their alkyl chain length (Figure 2-18). The improved PCE can be mainly ascribed to an increase in the V$_{OC}$ of ∼50 mV with 2D perovskite treatment. Figure 2-17c displays the V$_{OC}$ distribution of the corresponding

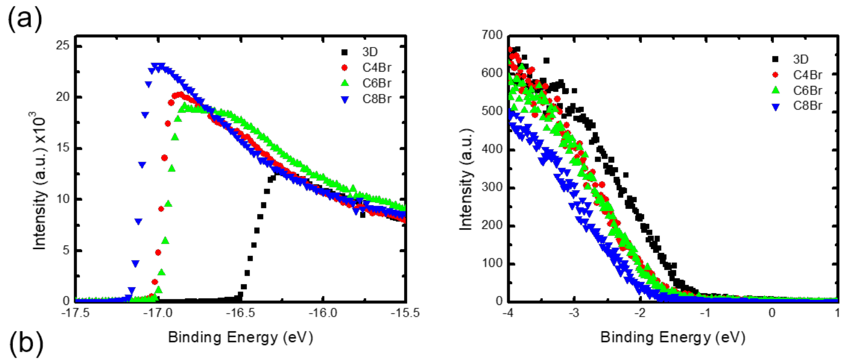

(b)

	Conduction Band (eV)	Work Function (eV)	Valence Band (eV)
3D	4.46	4.71	5.99
2D(C_4Br)	~3.52	4.19	5.89
2D(C_6Br)	~3.51	4.22	5.88
2D(C_8Br)	~3.58	4.06	5.95

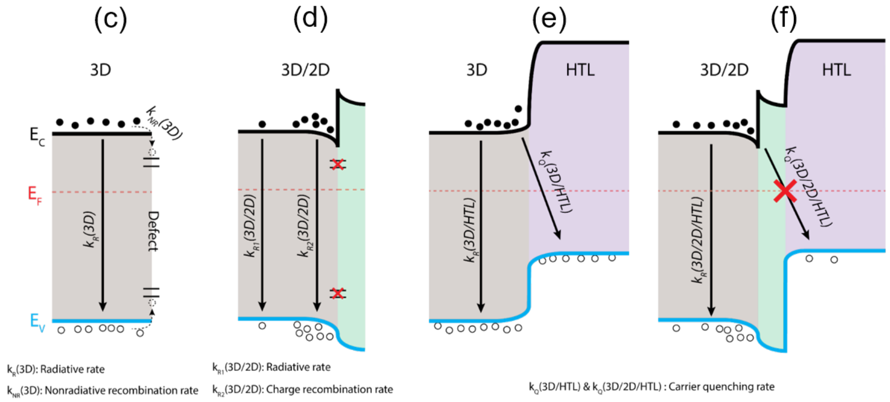

Figure 2-16: a, UPS spectra of 3D and three different 3D/2D perovskite substrates. b, Summary of energy levels determined from UPS measurements. band gaps of 1.53 eV and 2.37 eV were used to determine the conduction band of 3D and 3D/2D perovskites, respectively. The band gap for *in-situ* synthesized 2D perovskite is approximated by measuring the UVVis of a 2D perovskite that is synthesized separately and not using the 3D perovskite as the template. c-f, Energy band diagrams of various perovskite layers determined from UPS and TRPL measurements. CB, WF, and VB correspond to conduction band, work function, and valence band, respectively. Energy band diagram of 3D control (c) and 3D/2D perovskite (d), showing the passivation of surface defects with 2D perovskite treatment. Energy band diagram of 3D control (e) and 3D/2D perovskite (f) with the addition of the hole transport layer (HTL).

devices. The average V_{OC} is 1.10, 1.14, 1.15 and 1.15 V for the 3D control, C_4Br, C_6Br, and C_8Br-treated devices, respectively, and the champion V_{OC} (1.17 V) in this comparison study is achieved with a C_8Br-treated device. The increase in V_{OC} is consistent with measured increased carrier lifetimes (Figure 2.2-13). This result indicates that longer-chained 2D perovskite can effectively passivate surface and grain boundaries.[34][54] Although a slight difference in photovoltaic properties between 2D treated devices is observed, their device performance differences are not statistically significant, with the best PCEs reaching ∼23% for all alkyl chain lengths. Previous studies have focused on the chemical nature of 2D perovskite materials to fabricate high performance 3D/2D PSCs. Our finding, however, suggests that the dominant factor in the fabrication of 3D/2D PSCs is the method by which the *in-situ* synthesis of 2D perovskite is performed, rather than the exact composition of the 2D layer, as device performance seems insensitive to the type of 2D perovskite.

The SPD strategy effectively eliminates non-radiative recombination pathways at the perovskite/Spiro-OMeTAD interface, resulting in an increase in V_{OC}, and an expected increase in electroluminescence efficiency (Figure 2-17d-e and Figure 2-19). Figure 2-17d shows the EL emission from a PSC operating as a light-emitting diode (LED) with the photograph of the device shown in the inset. Figure 2-17e is the plot of current density, EL EQE, and radiance as a function of voltage. The SPD strategy based 3D/2D PSCs show a maximum EL EQE of 8.9%, compared to ∼3% for the 3D control, consistent with the increased V_{OC} for SPD based devices. The PSC fabricated using the conventional method shows a non-uniform EL emission likely due to the formation of an insulating phase being formed between the 3D perovskite and the hole transport layer, such as an amorphous or perovskite δ-phase.

3D and 3D/2D PSCs retain most of their initial device performance when stored under dark and dry conditions (∼ 20% relative humidity (RH)), (Figure 2-20a). Figure 2-20b-c shows a series of photographs and XRD patterns of perovskite substrates stored in a humidity chamber (∼90% RH) at room temperature. The 3D control shows bleaching of the perovskite after day 1 and is almost colorless after day 8. For the 2D perovskite treated substrates, all three samples show superior stability compared to the 3D control; increasing the alkyl chain length yields superior resistance to humidity, suggesting that the longer-chain 2D perovskites may be advantageous for the scale up of PSCs.

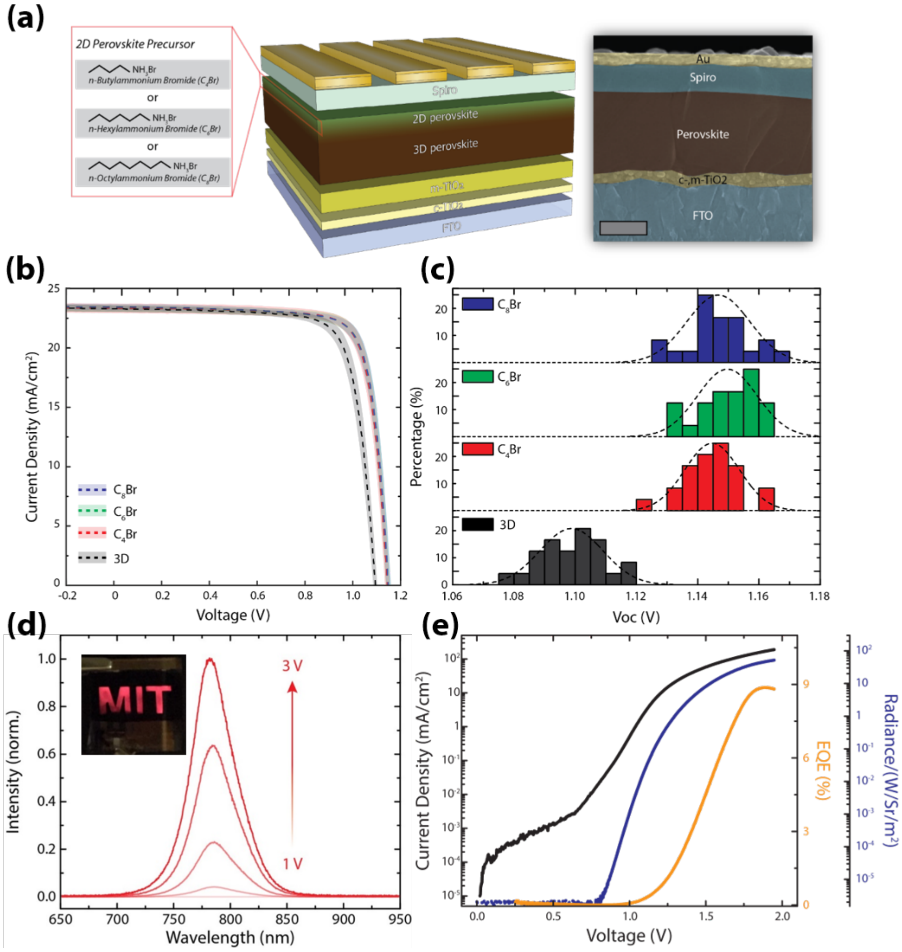

Figure 2-17: a, Schematic illustration of a 3D/2D PSC with false colored cross-sectional SEM (scale bar: 500 nm). b, J-V curves of 3D and 3D/2D (C_4Br, C_6Br, C_8Br) PSCs fabricated using the SPD strategy, with average and standard deviation shown as a dashed line and shaded area, respectively. c, Histogram of V_{OC} for 3D and 3D/2D (C_4Br, C_6Br, C_8Br) PSCs. d, An electroluminescence spectrum from the 3D/2D PSC operated as a LED. The inset shows the bright electroluminescence from the device. e, Plot of current density, EQE, and radiance as a function of voltage. The device shows a max EQE of 8.9%

Through optimization of device performance and with an anti-reflective coating, we achieved a reverse J-V PCE of 23.4% (Figure 2-21a). To ensure reliability of the data, 3D/2D PSCs were sent for certification to the Newport Corporation Technology and Application Center Photovoltaic Lab (Newport), an accredited testing laboratory, confirming a reverse J-V PCE of 23.2%. Quantifying PCEs for perovskite solar cells from J-V scans is problematic because conventional J-V sweeps can give rise

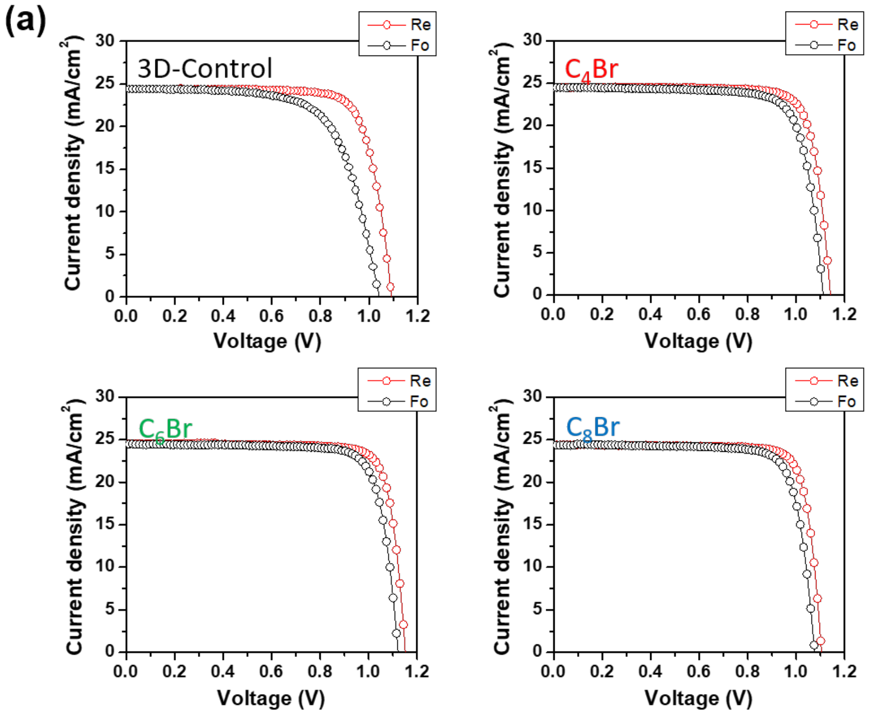

(b)

	V_{OC} (V)	J_{SC} (mA/cm^2)	FF (%)	PCE (%)
3D	1.10±0.01	24.0±0.4	78.5±1.0	20.7±0.4 (21.7)
C_4Br	1.14±0.01	24.0±0.5	79.9±1.1	22.0±0.6 (23.2)
C_6Br	1.15±0.01	24.2±0.4	80.3±1.1	22.4±0.4 (23.2)
C_8Br	1.15±0.01	24.2±0.3	79.8±1.2	22.1±0.4 (23.1)

Figure 2-18: a, J-V curves of 3D and 3D/2D representative PSCs showing reduced hysteresis for 2D perovskite treated PSCs. “Re” is the reverse scan the “Fo” is the forward scan. b, PCE average and standard deviation for 3D and 3D/2D PSCs measured over 20 devices. The PCE values in parentheses represent the result for the best-performing cells.

to out-of-equilibrium effects associated with the dynamic ionic characteristics of the perovskite layer.[55] In addition, several groups have noted that J-V sweeps do not reflect the true efficiency of a PSC device, and that even the absence of hysteresis in J-V measurements of PSCs is insufficient for predicting steady-state device characteristics, leading to an overestimations of steady-state device performance. [56][57][58] PSCs require light soaking for some period of time before reaching a stable state, and defective PSCs do not maintain their maximum efficiency under illumination.[59] As

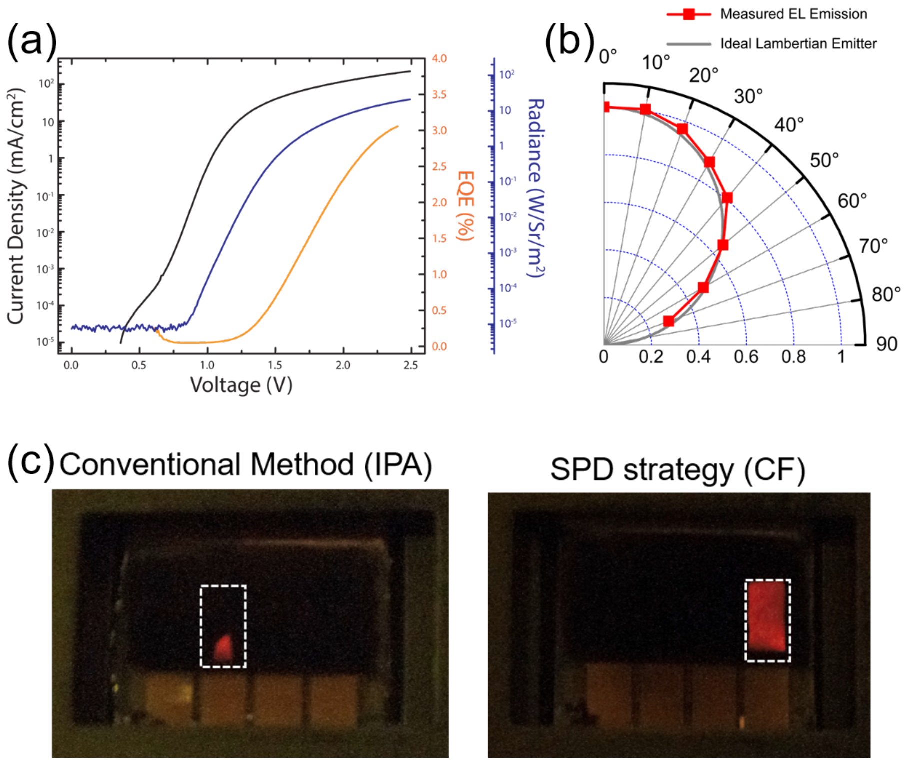

Figure 2-19: a, Plot of current density, EQE, and radiance as a function of voltage from the 3D control PSC. The device shows a max EQE of 3.0%. b, EL emission profile of a PSC showing an emission profile that resembles an ideal Lambertian emitter. c, Photograph of 3D/2D PSC operating as an LED. PSCs fabricated using the conventional method shows non-uniform EL emission from the active area (white dotted line), whereas devices fabricated using our newly developed SPD strategy shows uniform and complete EL emission from the active area.

a result, the most accurate way to translate device performance to that expected in an operational solar cell is to perform the measurement under stabilized conditions. We thus performed stabilized measurements to better quantify the PCE.

We first measured the V_{OC} and current density by holding the bias current, or voltage, until the measured voltage, or current density, remains unchanged at the 0.03% level. Figure 2-21b shows the measurement determining the stabilized V_{OC} ($V_{OC,S}$) where the initial V_{OC} increases from ∼1.16V, stabilizing at V_{OC},S ∼1.19V. The same principle is applied for the stabilized current density, but with the bias voltage held and the current density monitored at each voltage (Figure 2-21c). A total of 13 voltage points were measured (from 0 to $V_{OC,S}$) with a total measurement time of ∼31 min. Figure 2-21d shows the J-V curve extracted from the asymptotic measurement with $V_{OC,S}$: 1.19 V, $J_{SC,S}$: 24.2 mA/cm^2, FF_S: 78.5%, and PCE_S: 22.6% (subscript S means stabilized) (Figure 2-22). To the best of our knowledge, this is the highest certified stabilized PCE thus far for PSCs and the first demonstration of a certified stabilized efficiency over 20%.

In addition, the certified SPD based 3D/2D PSC shows a V_{OC} loss of only ∼340 mV (Figure 2-23), which is the lowest voltage loss report so far, regardless of the device structure. To confirm the reliability of the certification result, the same pad was tested over the course of two days (Figure 2-24), resulting in an almost identical result for both measurements, further supporting the enhanced operational stability of SPD based 3D/2D PSCs. In addition, the long term stability of the PSC was tested with maximum power point (MPP) tracking under full solar illumination without an ultra-violet cut-off filter (UV-filter). The 3D/2D PSC, with an initial PCE of 22.6%, maintained 85% of its initial efficiency over 500 hrs (Figure 2-24b), even without incorporation of Cs and Rb as additives.

In summary, we have shown that the SPD strategy based on a unique combination of linear alkyl ammonium bromides and CF effectively passivates interface defects, minimizes carrier quenching, and results in a record stabilized PCE and a EL efficiency; device performance metrics that conventional surface treatment method and passivation strategies were not previously able to deliver. In addition to effectively passivating interface defects, the SPD strategy is scalable and can be combined with various printing methods that could be used for the scaled-up production of heterojunction PSCs (ink-jet printing, roll-to-roll printing, and blade coating), which inevitability employ longer contact times between the underlying perovskite layer and the solvent used for surface treatment compared to spin-coating. The SPD strategy allows for a wide processing window, providing an ideal platform for the scaled-up production of heterojunction PSCs. [47]

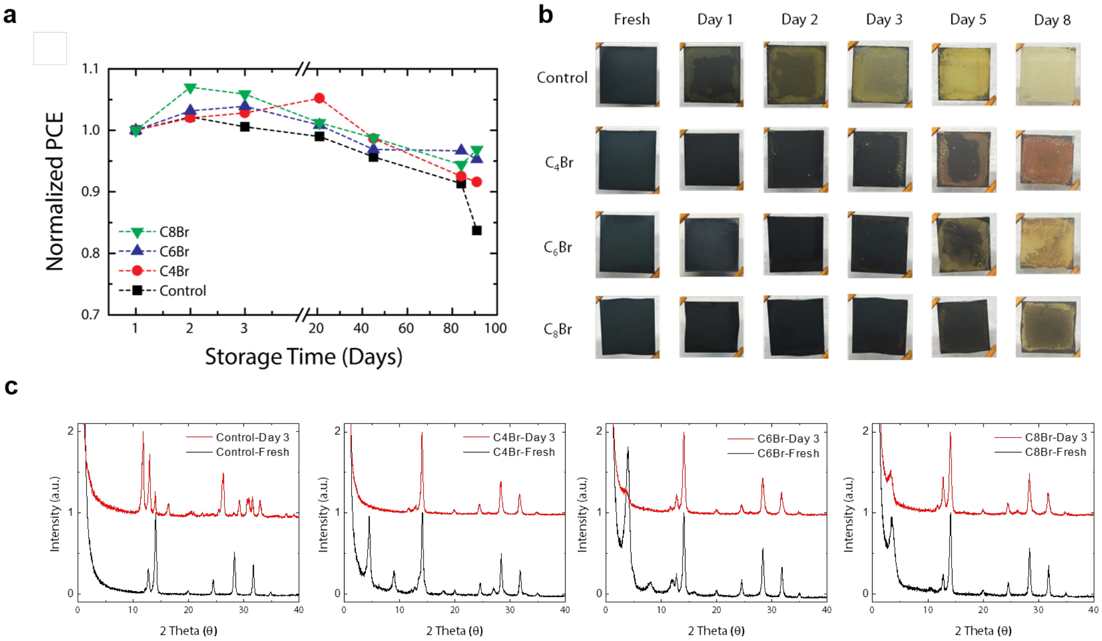

Figure 2-20: a, Normalized PCE as a function of storage time for 3D and 3D/2D PSCs. The devices were stored in dark and dry conditions between measurements. b, Photographs of 3D and 3D/2D perovskite films on glass substrates stored in a humidity chamber (∼90% RH) at room temperature as a function of storage time. The bleaching indicates decomposition of the 3D perovskite. The 3D/2D perovskite films showed higher resistance to moisture than the 3D control. An increase in alkyl chain provides additional resistance. c, XRD pattern of 3D and 3D/2D perovskite films on glass stored in the humidity chamber. The 3D control showed severe decomposition of the perovskite into PbI_2 and δ-phase perovskite on day 3, whereas 3D/2D perovskites showed no sign of δ-phase.

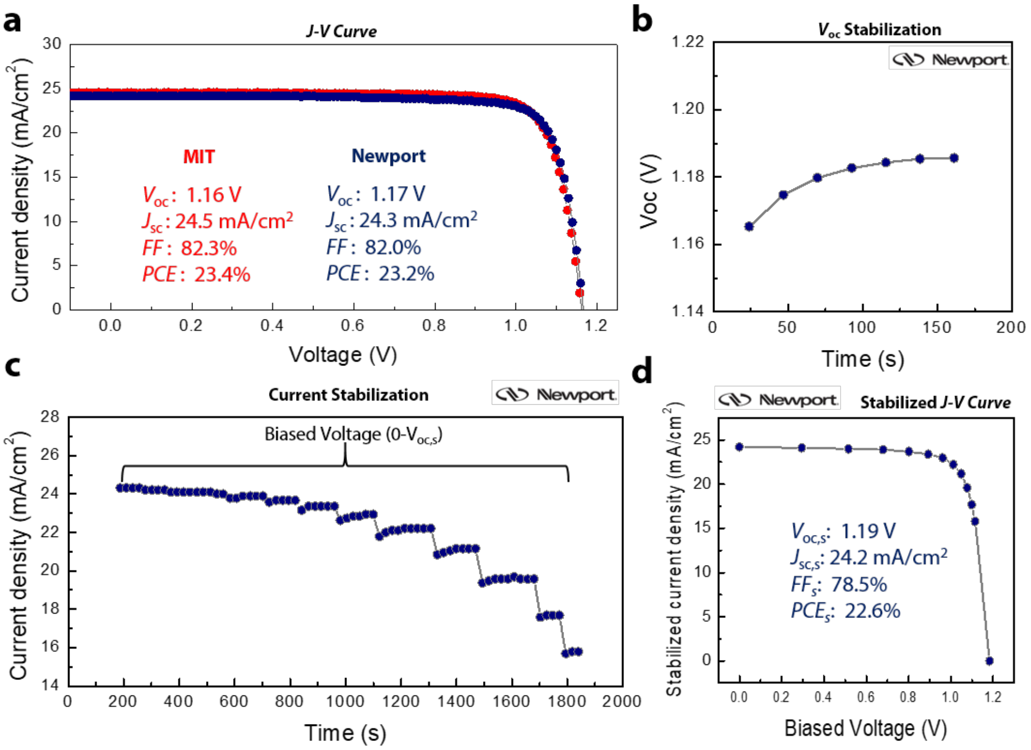

Figure 2-21: a, 3D/2D PSC devices with efficiencies measured at MIT and at Newport. b, Asymptotical measurement on stabilized open-circuit-voltage (V_{OC},S). c, Stabilization of current density. d, Stabilized J-V curve extracted from Figure 4b and c with stabilized power conversion efficiency (PCES) of 22.6%.

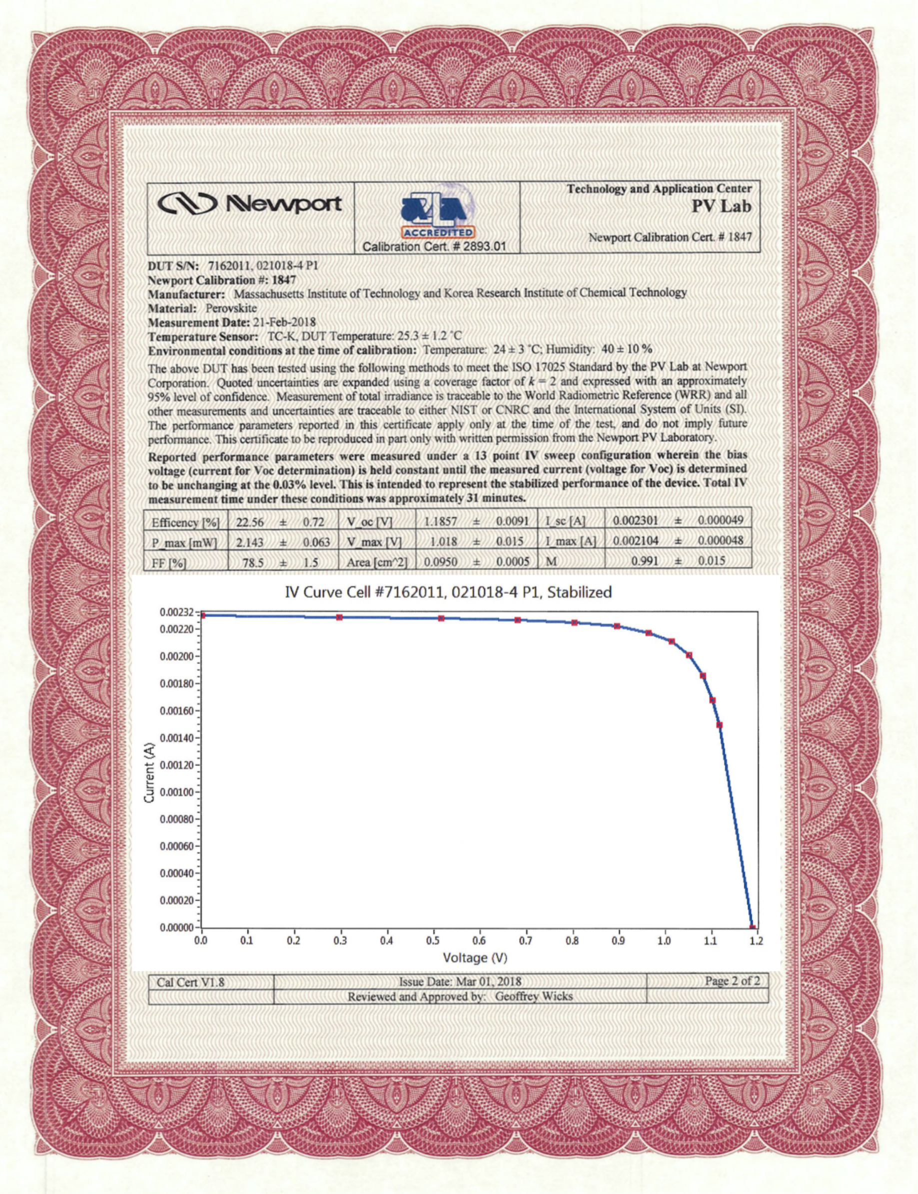

Newport

ACCREDITED
Calibration Cert. # 2893.01

Technology and Application Center
PV Lab
Newport Calibration Cert. # 1847

DUT S/N: 7162011, 021018-4 P1
Newport Calibration #: 1847
Manufacturer: Massachusetts Institute of Technology and Korea Research Institute of Chemical Technology
Material: Perovskite
Measurement Date: 21-Feb-2018
Temperature Sensor: TC-K, DUT Temperature: 25.3 ± 1.2 °C
Environmental conditions at the time of calibration: Temperature: 24 ± 3 °C; Humidity: 40 ± 10 %

The above DUT has been tested using the following methods to meet the ISO 17025 Standard by the PV Lab at Newport Corporation. Quoted uncertainties are expanded using a coverage factor of $k = 2$ and expressed with an approximately 95% level of confidence. Measurement of total irradiance is traceable to the World Radiometric Reference (WRR) and all other measurements and uncertainties are traceable to either NIST or CNRC and the International System of Units (SI). The performance parameters reported in this certificate apply only at the time of the test, and do not imply future performance. This certificate to be reproduced in part only with written permission from the Newport PV Laboratory.

Reported performance parameters were measured under a 13 point IV sweep configuration wherein the bias voltage (current for Voc determination) is held constant until the measured current (voltage for Voc) is determined to be unchanging at the 0.03% level. This is intended to represent the stabilized performance of the device. Total IV measurement time under these conditions was approximately 31 minutes.

Efficency [%]	22.56 ± 0.72	V_oc [V]	1.1857 ± 0.0091	I_sc [A]	0.002301 ± 0.000049
P_max [mW]	2.143 ± 0.063	V_max [V]	1.018 ± 0.015	I_max [A]	0.002104 ± 0.000048
FF [%]	78.5 ± 1.5	Area [cm^2]	0.0950 ± 0.0005	M	0.991 ± 0.015

IV Curve Cell #7162011, 021018-4 P1, Stabilized

Cal Cert V1.8	Issue Date: Mar 01, 2018	Page 2 of 2
	Reviewed and Approved by: Geoffrey Wicks	

Figure 2-22: Certification of 3D/2D PSC with stabilized J-V curve tested at an independent and accredited PV testing lab (Newport).

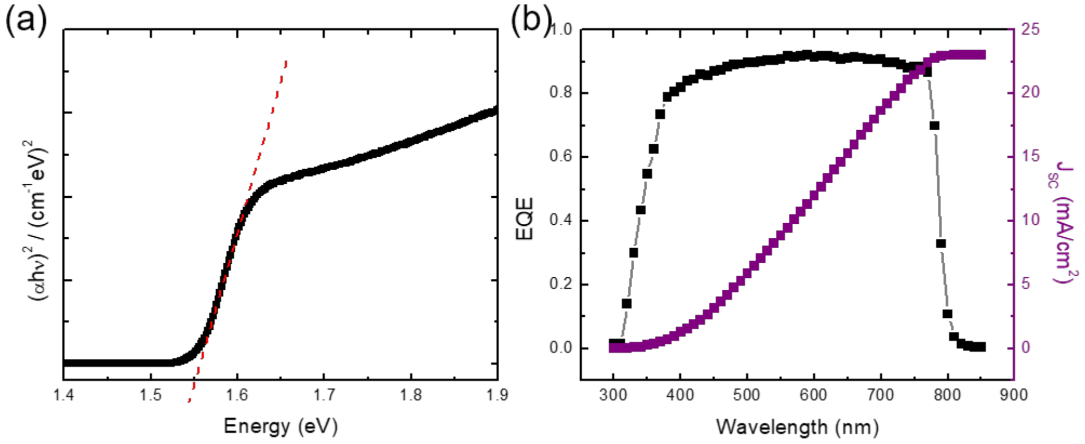

Figure 2-23: a,b, Tauc plot from UV-Vis absorption spectrum (a) and external quantum efficiency (EQE) plot (b) used to determine the band gap. band gap determined from tangent line from UV-Vis tauc plot is ∼1.56 eV and from the EQE plot is ∼1.55 eV. The band gap determined from EQE onset is ∼1.53 eV. The integrated current density determined from the EQE spectrum is also shown in b.

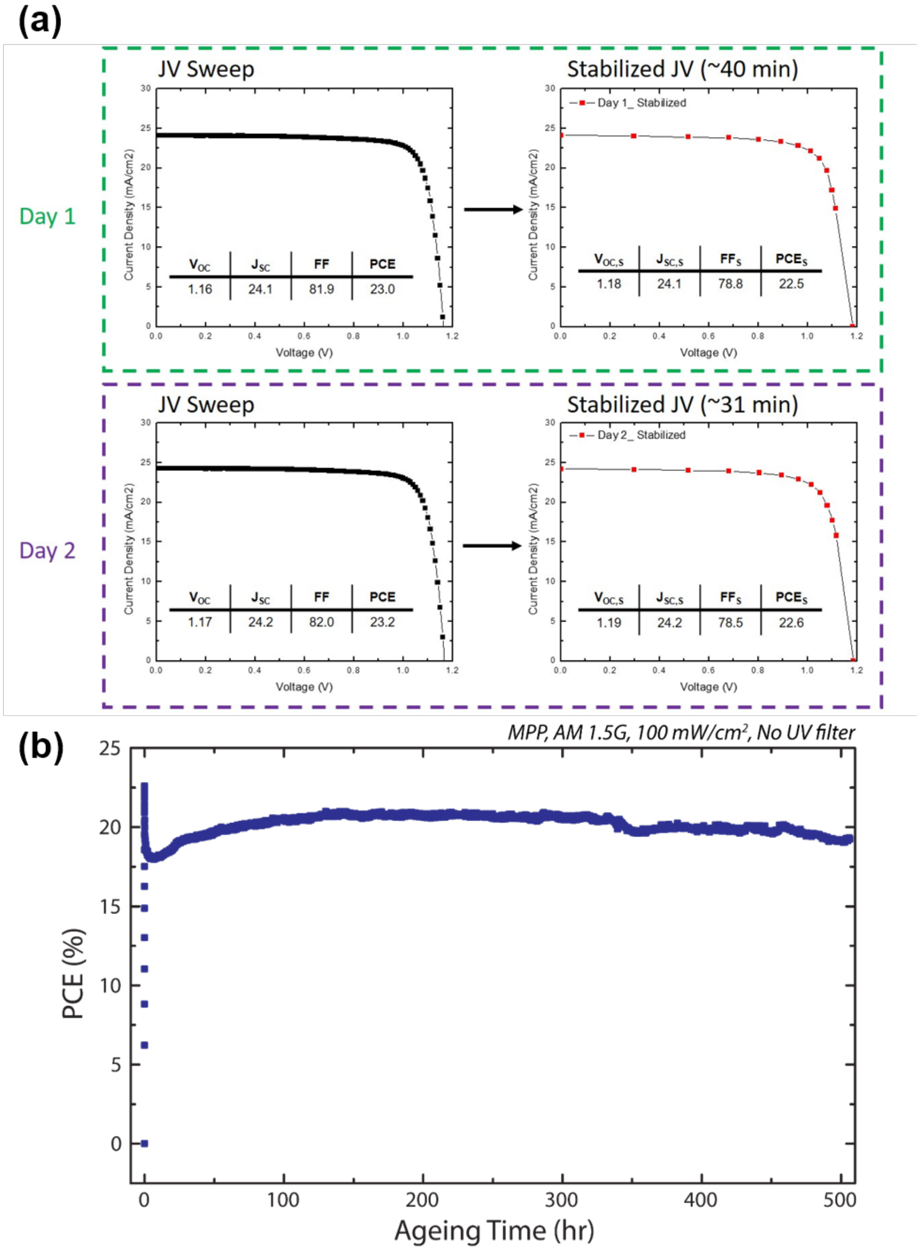

Figure 2-24: a, 3D/2D PSC device results on the same pad on two consecutive days (measurement at Newport). The 3D/2D PSC shows almost identical results even after extensive stabilization measurement (∼40 min on day 1 and ∼31 min on day 2) demonstrating remarkable operational stability. b, The MPP was measured under full solar illumination (AM 1.5G, 100 mW/cm^2) without a UV-filter. The PSC shows an initial PCE of 22.6% and maintained 85% of its efficiency after 500 hrs. The device is encapsulated and measured in ambient condition.

2.2 Low-Temperature Solution Processable ETL

The content of this chapter has been submitted for peer-review.

2.2.1 Why do we need a new ETL?

The last decade has seen a rapid and remarkable rise in the power conversion efficiency (PCE) of perovskite solar cells (PSCs), accompanied by a considerable maturation of their scientific and technological basis.[60][7][61][33][62][29][63][64][65][66] Nevertheless, PSCs still lag their commercialized solar cell counterparts in device performance, such as Silicon (Si) and Gallium Arsenide (GaAs), which show PCEs surpassing 80% of their band gap determined Shockley and Queisser (SQ) efficiency limits. For PSCs to effectively compete on the road to lower levelized costs of electricity from photovoltaic systems, further improvements in device performance are likely necessary.[67][68]

The short-circuit current density (J_{SC}) already closely approaches the SQ limit for the best performing PSCs.[69] Despite near ideal J_{SC}, the fill factor (FF) and the open-circuit voltage (V_{OC}) have remained bottlenecks towards further approaching the SQ efficiency limit. Improvements in carrier management, which is closely tied to the FF and the V_{OC}, is thus the more obvious path to increasing the device performance of PSCs. Strategies need to be developed to: 1) efficiently extract photo-generated carriers from the photo-absorber, and 2) transport these carriers through the transporting layer without carrier recombination and photo-voltage losses.

For a n-i-p structure, mesoporous TiO_2 (m-TiO_2) was widely used as it offered high collection efficiency due to its physical structure and has resulted in highly efficient perovskite solar cells (Figure 2-25). [25][70] However, m-TiO_2 requires high sintering temperature with hygroscopinc doping agents. In addition, TiO_2 exhibits a photocatalytic effect, which is not favorable from long-term stability aspect. Recently, tin dioxide (SnO_2) based ETLs have gained much interest as they offer favorable band alignment, while being low temperature processable with various deposition methods.[71][72][73][74][75][76] SnO_2 nanoparticles (NPs) have shown promise in fabricating highly efficient PSCs (Figure 2-25). However, NP-based ETLs suffer from incomplete interconnectivity between individual NPs resulting in imperfect surface coverage of the contact electrode. In addition, SnO_2 NPs synthesized via aqueous chemical routes are only weakly n-type, limiting efficient electron transport.[77] Finally, SnO_2 NPs based PSCs exhibit low external electroluminescence quantum efficiencies (ELEQE), compared to GaAs solar cells, in spite of various efforts to eliminate non-radiative recombination pathways via passivating the perovskite/HTL interface.[78] These deficiencies motivate developing strategies that minimize photo-voltage losses at the ETL/perovskite interface so as to maximize the V_{OC}, thus encouraging the search for a different deposition method that can develop the full potential of SnO_2 ETLs.

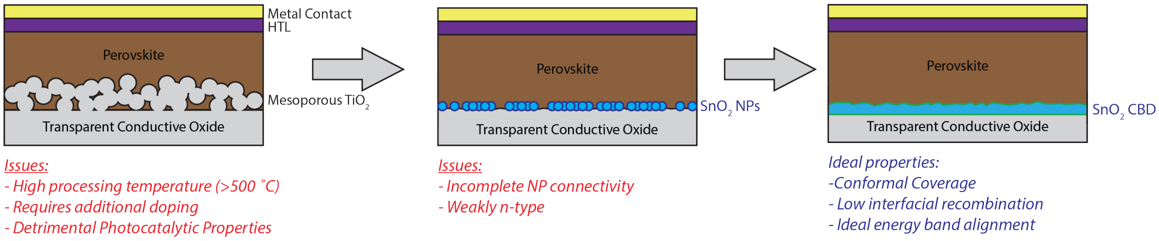

Figure 2-25: Illustration of m-TiO_2 based perovskite solar cell structure, SnO_2 NP based structure, and its issues. Lastly, the SnO_2 CBD based structure with ideal properties is shown on the right.

2.2.2 Developing efficient ETL using Tin oxide (SnO_2)

Synthesis and Characterization of CBD based SnO_2 ETL

In this chapter of the thesis, I report a facile method to chemically tune the physical and electronic properties of the SnO_2 ETL via chemical bath deposition (CBD). We show that this results in highly efficient PSCs. Chemical bath deposition (CBD) allows uniform and complete coverage of the underlying substrate via depositing a dense and conformal layer.[78][79] However, a lack of understanding of the complex chemical reactions during SnO_2 CBD has prevented fabricating highly efficient PSCs. We infer that the Sn intermediate species during CBD play a crucial role in the quality and the characteristics of the final SnO_2 layer, and that these Sn intermediate species can be modulated by controlling the pH of the CBD solution. More specifically, we suggest that the formation of various Sn intermediate species depends on the decomposition pathway of the Sn^{2+} precursor ($SnCl_2$), which depends on the pH of the reaction solution.[80][81][82] The freshly prepared CBD solution exhibits pH <1 and the pH increases with longer reaction time as urea decomposes and releases OH-. The changes in the thin film properties of the SnO_2 layer with reaction time, and thus pH, is shown below.

Figures 2-26A-D show scanning electron microscope (SEM) images of the SnO_2 layer synthesized on top of an FTO film via CBD. Although the large FTO nanodomains dominate the image, SnO_2 nanoparticles can be seen on top of the much larger FTO nanodomains. The top-right insets are the zoomed-in-view of the top-down SEM images, highlighting the texture and the surface morphology of the film, with the SnO_2 nanoparticles more clearly seen. The insets on the bottom-right are cross-section transmission electron microscope (TEM) images showing the cross-section characteristics of the thin, uniform, and conformal SnO_2 layer on top of the structured FTO film. In the early stage of the reaction, or when the pH of the reaction solution is still $\sim$1, the SnO_2 nanoparticle layer is $\sim$20 nm thick, conformal with the underlying FTO layer (Figures 2-26A lower right inset). With increasing reaction time, thus an increase in the pH of the reaction solution, the size of the nanoparticles increases while forming a densely packed layer with thicknesses up to 45nm and 70 nm (Figures 2-26B and C, pH 1.5 and 3, respectively). When the acidity of the solution reaches pH 6, the particles begin to grow in an elongated rod-like morphology (Figures 2-26D).

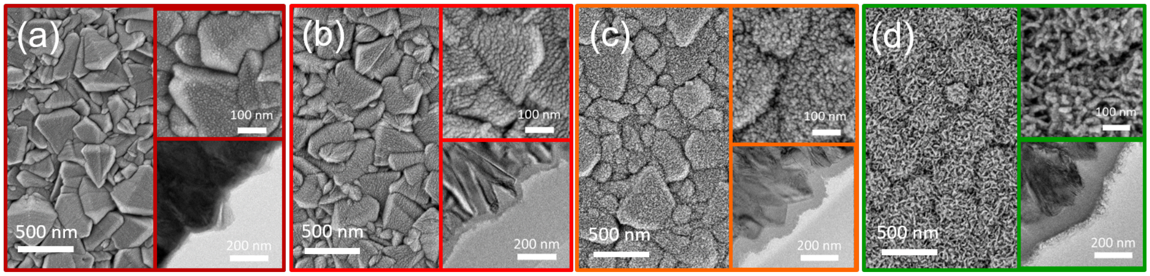

Figure 2-26: Top view SEM images synthesized with increasing time leading to an increased pH: (A) pH=1, (B) pH=1.5, (C) pH=3 and (D) pH=6. Top-right insets show a zoomed-in SEM and bottom-right insets show corresponding cross-sectional TEMs.

High-resolution TEM (HRTEM) analyses of the SnO_2 film are shown in Figures 2-26B, or when the pH is ~1.5 (Figure 2-27E and F). HRTEM shows the SnO_2 layer forming a complete coverage with interconnected nanoparticles, even down the sharp valleys within the FTO layer (Figure 2-27E).

The completeness of the coverage is further confirmed by cyclic voltammetry (CV), which shows that the films have robust hole-blocking properties when reacted past pH 1.5 (Figure 2-28). The lattice fringes in Figure 2-27b indicate that individual nanoparticles have high crystallinity, where the lattice fringes corresponds to the (110) and (101) planes of rutile SnO_2, which is in agreement with the result of selective-area electron diffraction (SAED) (Figure 2-27b inset). In addition, the films prepared while still under acidic conditions (pH= 1, 1.5, and 3) have a pure phase, while films prepared allowing the reaction solution to reach pH 6 contain secondary phases, such as $Sn_6O_4(OH)_4$ and SnO (Figure 2-29a).

X-ray photoelectron spectroscopy (XPS) provides insight on the progress of the oxidation state of Sn as a function of pH (Figure 2-29b). As the pH of the reaction solution increases, the peak corresponding to the Sn3d$_{\frac{5}{2}}$ state (~487 eV) shifts towards lower binding energies, suggesting formation of Sn^{2+} species, yielding

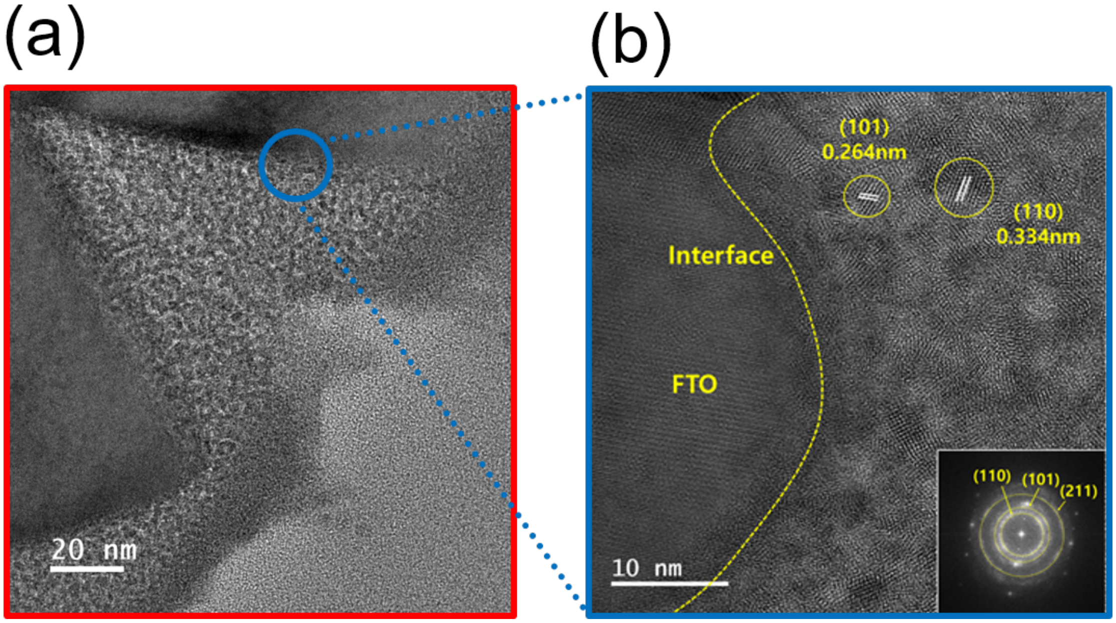

Figure 2-27: (a) and (b) are HR-TEM images of films prepared at the pH 1.5 time point (inset in Figure 2-27B: SAED pattern).

$SnO_{2-x,(0<x<2)}$,[83][84][85][86][87] thus resulting in increased oxygen vacancies in the SnO_{2-x} layer. UV-Vis spectroscopy further supports this conclusion (Figure 2-29c).[83][84][85][86][87] When the pH of the solution increases, SnO_{2-x} films show increased absorptivity in the blue-UV wavelength range. This can be attributed to an increase in the shallow donor levels near the conduction band.[83][86][88][89] These shallow donor levels can contribute free electrons to the conduction band, thus improving the conductivity and charge transport properties of layers as ETLs in PSCs.[77][90]

Based on the experimental results, we can classify the reaction progress into three parts based on the reaction time and the pH of the solution (Figure 2-30a). At the beginning of the reaction (Stage A-1, pH = 1-1.5), the dominant product of the CBD reaction is a somewhat oxygen deficient SnO_{2-x}. As the reaction progresses in time to a higher pH of ∼3 (Stage A-2), oxygen vacancies increase further as seen in the larger decrease in binding energy in XPS (Figure 2-29b) and a continuing increase in absorption in the UV-blue (Figure 2-29c). When the pH of the reaction solution reaches ∼6, oxygen deficient SnO_{2-x} is joined with $Sn_6O_4(OH)_4$ and SnO that are produced as secondary phases as observed from X-ray diffraction (XRD) data (Figure

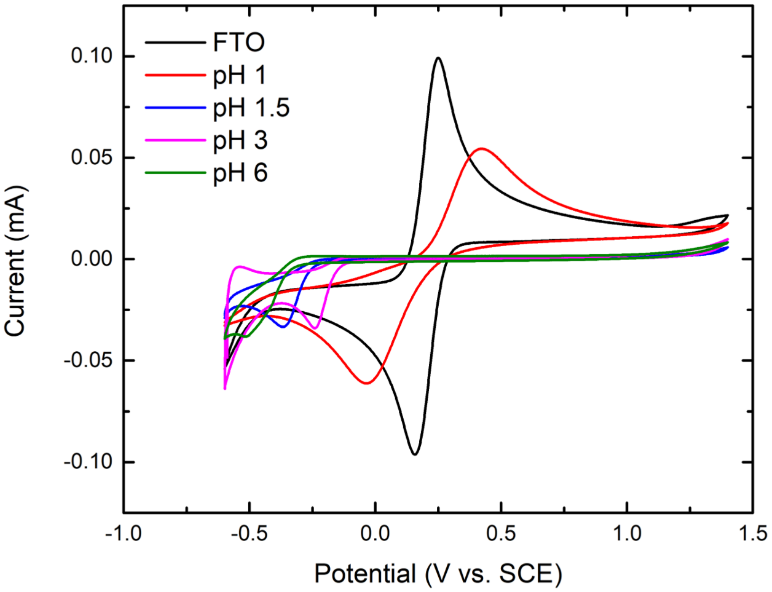

Figure 2-28: Cyclic voltammograms of bare FTO and SnO_2 ETL synthesized up to various pH values. The scan rate was 0.1 V/s and the electrolyte solution was 0.5 mM $K_4Fe(CN)_6$ + 0.5 mM $K_3Fe(CN)_6$ in 0.5M aqueous KCl. A saturated calomel electrode (SCE) is used as the reference electrode.

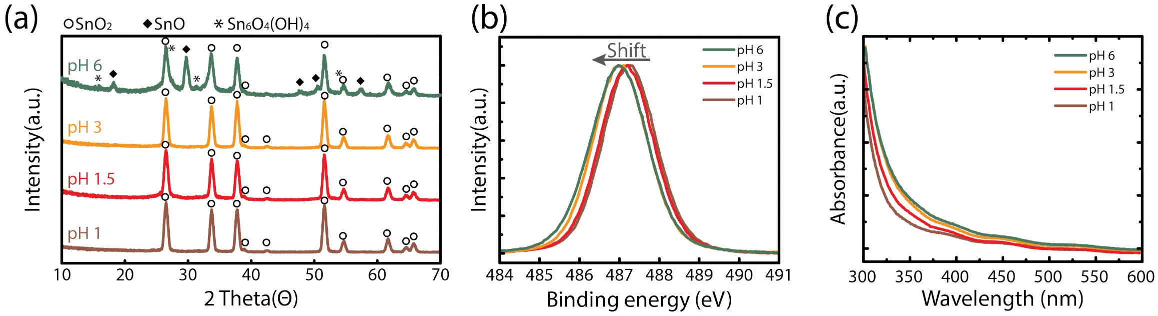

Figure 2-29: (A) XRD patterns, (B) XPS Sn3d5/2 spectra, and (C) UV-Vis absorption spectra of films synthesized with increasing time leading to an increased pH.

2-29a).

We propose a possible synthesis mechanism during the CBD growth of SnO_{2-x} in Figure 2-30b. In stage A, the Sn^{2+} ions dissolved in strong acidic aqueous solution undergo a hydrolysis reaction, and form $Sn(OH)^+$ intermediate species. $Sn(OH)^+$ is then oxidized to Sn^{4+} by the dissolved oxygen in the solution.[80] The Sn^{4+} ions then react with OH- ions, provided via decomposition of urea, to form $Sn(OH)_4$ species,

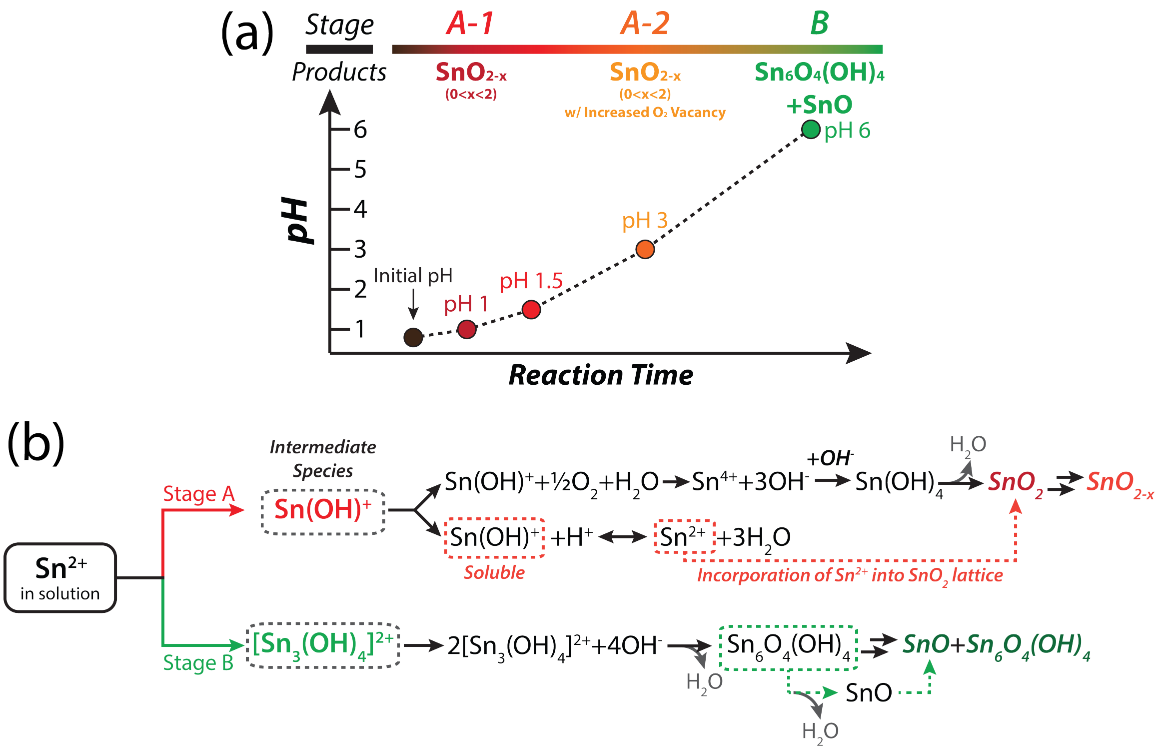

Figure 2-30: (a) and (b) Schematic illustration of the overall reaction mechanism for the formation of the tin oxide film.

which are converted to SnO_2 via a dehydration reaction (top branch in Figure 2-30b).[80][91] However, the conversion of $Sn(OH)^+$ to Sn^{4+} is not complete at CBD temperatures (<100 °C)[83]; Sn^{2+} ions from $Sn(OH)^+$ can then readily incorporate into the SnO_2 lattice due to comparable ionic radii between Sn^{2+} (0.62 Å) and Sn^{4+} (0.69Å) for hexa-coordinated Sn species (middle branch in Figure 2-30b).[86][87][89] The incorporation of Sn^{2+} into the SnO_2 lattice leads to the formation of oxygen vacancies in the SnO_2 layer to preserve charge neutrality. This leads to the oxygen deficient nonstoichiometric SnO_{2-x} that is synthesized in stages A-1 and A-2.

After the initial phase of the CBD reaction (stage A-1), the pO_2 (partial pressure of oxygen) decreases since the reaction occurs in a closed container and oxygen is consumed, and this slows down the oxidation of $SnOH^+$ to Sn^{4+}.[80][91] This results in a relative increase in Sn^{2+} species and leads to increased oxygen vacancies in the SnO_{2-x} layer due to self-doping of Sn^{2+} (stage A-2) (the decreased pO2 begins to favor the middle branch over the top branch in Figure 2-30b). With the pH of the solution reaching ~6 (stage B), a different Sn intermediate species, $Sn_3(OH)_4^{2+}$, forms in the reaction.[81][92] The $Sn_3(OH)_4^{2+}$ intermediate species can undergo a condensation reaction when the OH^- concentration is high enough, resulting in $Sn_6O_4(OH)_4$.[81][82][93] The $Sn_6O_4(OH)_4$ is then partially transformed to SnO via a dehydration reaction, producing a mixture of $Sn_6O_4(OH)_4$ and SnO (bottom branch in Figure 2-30b), consistent with the XRD (Figure 2-29).[82][94]

Perovskite solar cell device performance

A series of PSCs are fabricated at various time points (pH points) for the growth of the SnO_{2-x} layer to evaluate the effect of physical morphology and oxygen vacancies in the SnO_{2-x} layer on device performance. The perovskite composition is $FAPbI_3$ with an added 5 mol% $MAPbBr_3$. Figure 2-31a shows the device statistics for SnO_2 ETLs based PSCs, where the SnO_2 layer was reacted until the reaction solution reached a specific pH, with "pH 1" having the shortest and "pH 6" having the longest reaction time. PSCs with SnO_2 undergoing the shortest reaction time (pH 1) shows an average PCE of ~20% with wide distribution, likely due to incomplete coverage and thus poor hole-blocking effects in the SnO_2 layer (Figure 2-28), resulting in high interfacial recombination.

With an increase in the pH up to 1.5, the PSCs exhibited PCEs exceeding 24% with the greatest improvements in the V_{OC} and the FF, where they are exceeding 1.2 V and 84%, respectively (Figure 2-32). When the pH of the reaction solution exceeds 1.5, we observe gradual decrease in the device performance with greatest contribution from the lower FF and the V_{OC}, which can be attributed to the high concentration of oxygen vacancy in SnO_{2-x}. Optimum level of oxygen vacancies facilitate electron transport by forming shallow donor levels, while excess oxygen vacancies may trap photogenerated electrons, resulting in severe recombination and poor charge extraction.[95] The PSCs with pH 6 SnO_2 show the lowest PCE, likely due to the formation of non-SnO_{2-x} phases, such as $Sn_6O_4(OH)_4$ and SnO, which are not electron transporting. This demonstrates careful engineering of the oxygen vacancies in the SnO_{2-x} film with an appropriate coverage of the FTO, while suppressing the

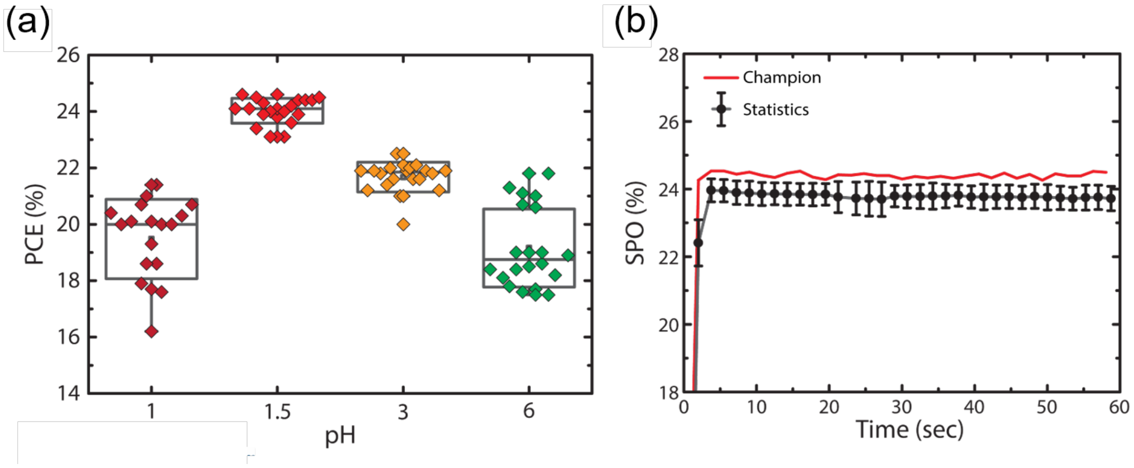

Figure 2-31: (A). PCE statistics for >20 best performing PSCs based on SnO_2 ETL synthesized with increasing time leading to increased pH time points. (B) Stabilized power output (SPO) for 16 PSCs with a SnO_2 ETL fabricated at the pH=1.5 time point. The black trace is the average statistics and the red trace is the champion device with SPO reaching up to 24.5%.

formation of non-SnO_{2-x} phase, is crucial for fabricating high performance PSCs.

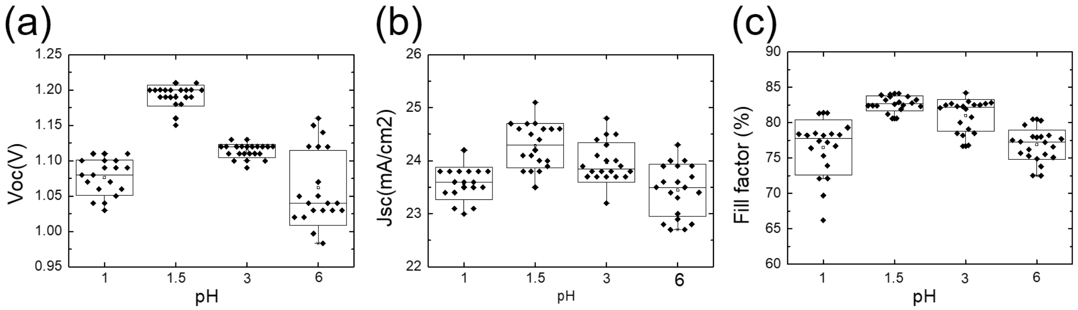

Figure 2-32: Device statistics for the open-circuit voltage (V_{OC}) (A), the short-circuit current density (J_{SC}) (B), and the fill factor (FF) (C) for the devices with SnO_{2-x} ETL synthesized up to various pH.

To obtain a reliable and reproducible result, we fabricated a large batch (68 devices) of PSCs with the optimized SnO_{2-x} ETL (pH 1.5), and they exhibit a narrow PCE distribution with an average PCE exceeding 24% (Figure 2-33). Furthermore, the average stabilized power output (SPO) extracted from maximum power point tracking for best 16 devices show an average SPO of 24.07% with a maximum SPO reaching up to 24.76% (Figure 2-31b). To certify our devices, we sent our best performing devices to Newport, a third-party testing center. Figure 2-34 shows the current-voltage (JV) curve measured before and after quasi steady-state (QSS) measurement as well as the QSS JV curve. The device showed almost no change in the PCE throughout each measurement with the PCE reaching up to 24.2%, determined from the QSS measurement. (Figure 2-35)

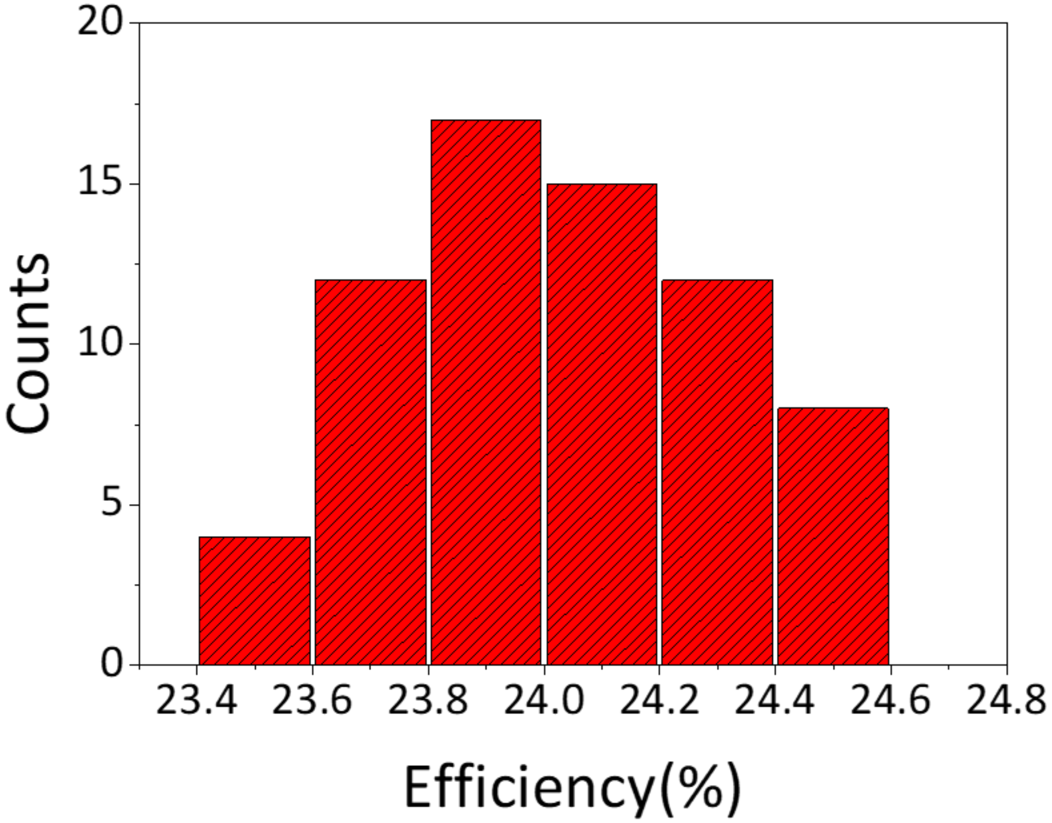

Figure 2-33: Histogram of device efficiency for 68 devices with pH 1.5 SnO_2 ETL.

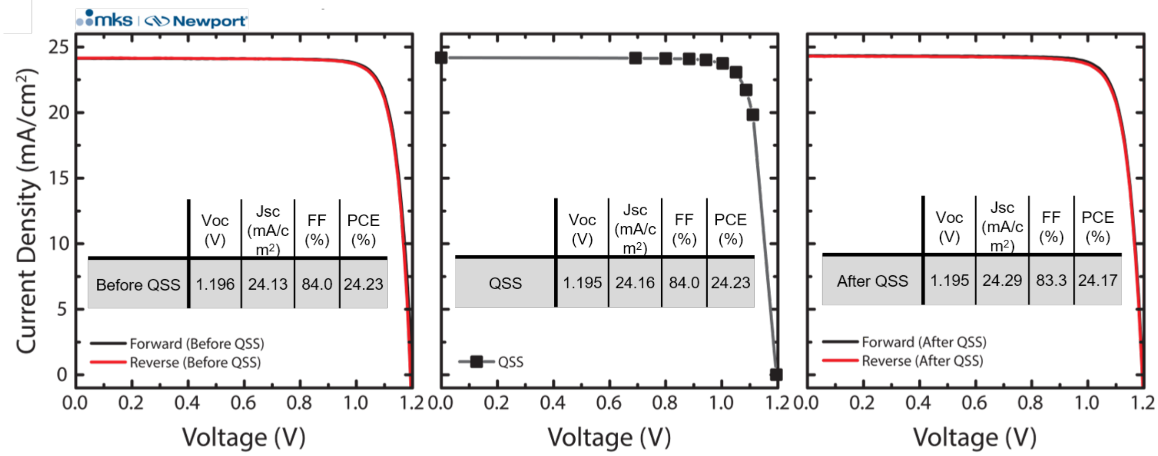

	Voc (V)	Jsc (mA/cm2)	FF (%)	PCE (%)
Before QSS	1.196	24.13	84.0	24.23

	Voc (V)	Jsc (mA/cm2)	FF (%)	PCE (%)
QSS	1.195	24.16	84.0	24.23

	Voc (V)	Jsc (mA/cm2)	FF (%)	PCE (%)
After QSS	1.195	24.29	83.3	24.17

Figure 2-34: J-V curves before and after stabilization, and QSS J-V curve of the best-performing device (pH 1.5) tested at Newport. The device exhibits a PCE of 24.2% from the QSS measurement. The inset tables show the average device performance from the reverse and the forward JV sweep.

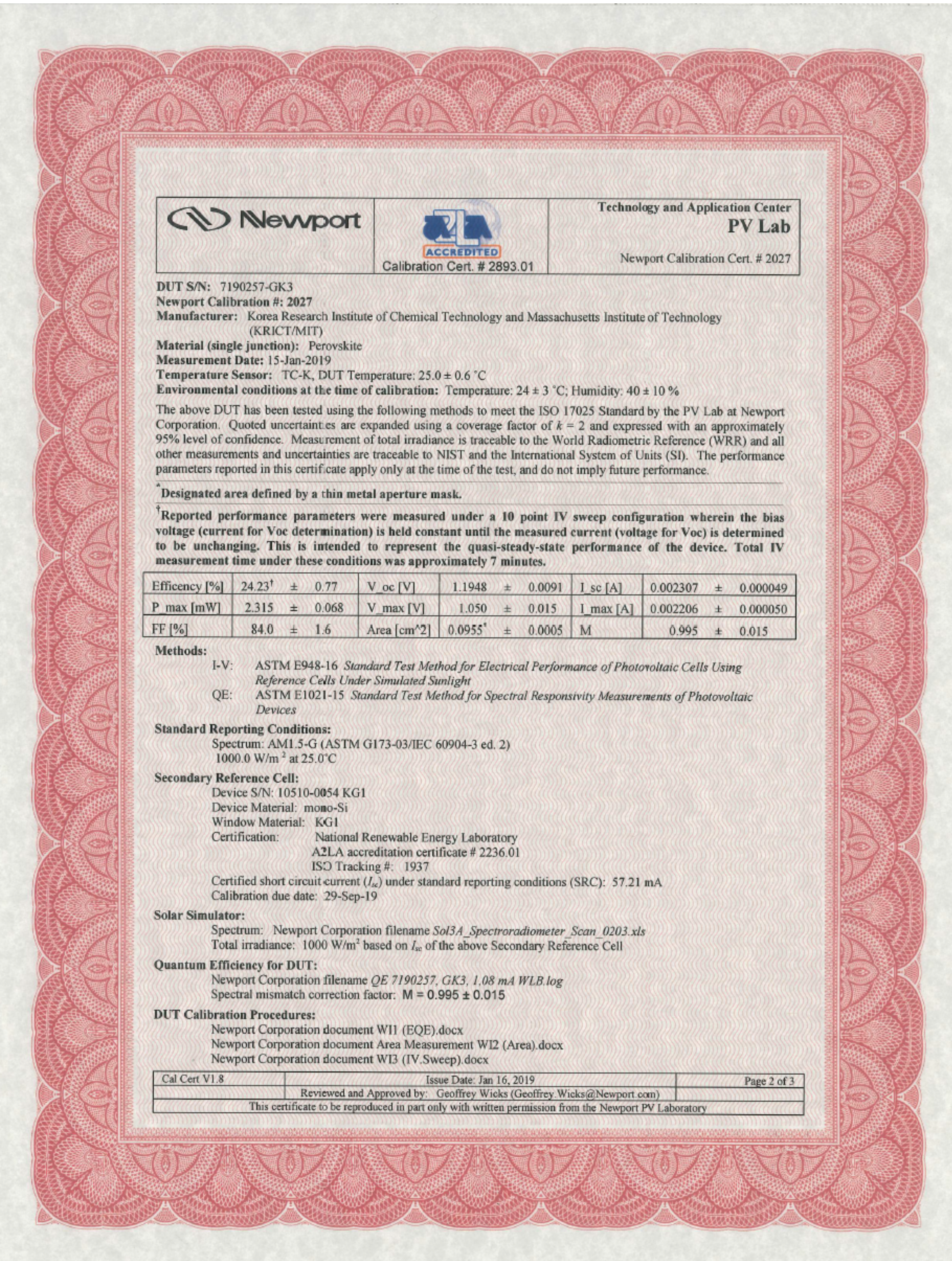

Newport

ACCREDITED
Calibration Cert. # 2893.01

Technology and Application Center
PV Lab
Newport Calibration Cert. # 2027

DUT S/N: 7190257-GK3
Newport Calibration #: 2027
Manufacturer: Korea Research Institute of Chemical Technology and Massachusetts Institute of Technology (KRICT/MIT)
Material (single junction): Perovskite
Measurement Date: 15-Jan-2019
Temperature Sensor: TC-K, DUT Temperature: 25.0 ± 0.6 °C
Environmental conditions at the time of calibration: Temperature: 24 ± 3 °C; Humidity: 40 ± 10 %

The above DUT has been tested using the following methods to meet the ISO 17025 Standard by the PV Lab at Newport Corporation. Quoted uncertainties are expanded using a coverage factor of $k = 2$ and expressed with an approximately 95% level of confidence. Measurement of total irradiance is traceable to the World Radiometric Reference (WRR) and all other measurements and uncertainties are traceable to NIST and the International System of Units (SI). The performance parameters reported in this certificate apply only at the time of the test, and do not imply future performance.

[*] **Designated area defined by a thin metal aperture mask.**

[†] **Reported performance parameters were measured under a 10 point IV sweep configuration wherein the bias voltage (current for Voc determination) is held constant until the measured current (voltage for Voc) is determined to be unchanging. This is intended to represent the quasi-steady-state performance of the device. Total IV measurement time under these conditions was approximately 7 minutes.**

Efficency [%]	24.23[†] ± 0.77	V_oc [V]	1.1948 ± 0.0091	I_sc [A]	0.002307 ± 0.000049
P_max [mW]	2.315 ± 0.068	V_max [V]	1.050 ± 0.015	I_max [A]	0.002206 ± 0.000050
FF [%]	84.0 ± 1.6	Area [cm^2]	0.0955[*] ± 0.0005	M	0.995 ± 0.015

Methods:
I-V: ASTM E948-16 *Standard Test Method for Electrical Performance of Photovoltaic Cells Using Reference Cells Under Simulated Sunlight*
QE: ASTM E1021-15 *Standard Test Method for Spectral Responsivity Measurements of Photovoltaic Devices*

Standard Reporting Conditions:
Spectrum: AM1.5-G (ASTM G173-03/IEC 60904-3 ed. 2)
1000.0 W/m^2 at 25.0°C

Secondary Reference Cell:
Device S/N: 10510-0054 KG1
Device Material: mono-Si
Window Material: KG1
Certification: National Renewable Energy Laboratory
A2LA accreditation certificate # 2236.01
ISO Tracking #: 1937
Certified short circuit current (I_{sc}) under standard reporting conditions (SRC): 57.21 mA
Calibration due date: 29-Sep-19

Solar Simulator:
Spectrum: Newport Corporation filename *Sol3A_Spectroradiometer_Scan_0203.xls*
Total irradiance: 1000 W/m^2 based on I_{sc} of the above Secondary Reference Cell

Quantum Efficiency for DUT:
Newport Corporation filename *QE 7190257, GK3, 1.08 mA WLB.log*
Spectral mismatch correction factor: M = 0.995 ± 0.015

DUT Calibration Procedures:
Newport Corporation document WI1 (EQE).docx
Newport Corporation document Area Measurement WI2 (Area).docx
Newport Corporation document WI3 (IV.Sweep).docx

Cal Cert V1.8	Issue Date: Jan 16, 2019	Page 2 of 3
	Reviewed and Approved by: Geoffrey Wicks (Geoffrey.Wicks@Newport.com)	
This certificate to be reproduced in part only with written permission from the Newport PV Laboratory		

Figure 2-35: Certification of PSC efficiency exhibiting stabilized power conversion efficiency of 24.23% obtained from a device with pH 1.5 SnO_2 ETL.

2.3 Improving Perovskite Thin Film's Optoelectronic Properties

2.3.1 How can we further improve PCE?

In addition to engineering the physical and electrical properties of the ETL, further improvements in PSC performance can be achieved by pushing the band gap of the FA-based perovskites redder towards pure band gap of $FAPbI_3$, thereby decreasing the band gap penalty. In lead halide perovskites, several strategies have been reported to eliminate $MAPbBr_3$, an α-$FAPbI_3$ stabilizing agent, from the perovskite composition as it leads to wider band gap perovskite.[8] Instead, an alternative inorganic or organic cations were introduced as a stabilizing agent.[96][46] However, this approach uses a cation that does not fit into the perovskite crystal structure, according to the Goldschmidt tolerance, and this can result in decreased carrier mobility and negatively affects device performance, especially the FF.[18] Thus, a strategy to red-shift the band gap of the perovskite without negatively affecting the carrier mobility is crucial for further improving the efficiency of PSC performance.

Highly efficient PSCs require that both the bulk and the interface be stabilized and passivated to remove detrimental defects. Here we decouple passivation of the bulk perovskite and the perovskite interface. We show that only a trace amount of $MAPbBr_3$ is needed to stabilize the bulk of the perovskite, thereby minimizing the band gap penalty from adding $MAPbBr_3$. This is in contrast to the commonly used range of 7-20 mol%, which we speculate may have become established through processes that passivate both the bulk and the interface in one step, where the more unstable interface requires the higher concentration. We were also motivated by previous reports that show that additives at less than 1 mol% can improve device performance.[97][98][70] For the interface of the perovskite, which has been reported to be more prone to the formation of defects and the unfavorable δ-phase, we use a post-treatment using a 2D perovskite strategy that has been previously described by us and others.[25][99] Thus, through separately passivating the bulk and the interface, high efficiency PSCs with high-quality perovskite bulk active layers can be fabricated by significantly reducing the commonly added $MAPbBr_3$ concentration, without adding foreign cations that fall out of the Goldschmidt tolerance range.

2.3.2 Minimizing $MAPbBr_3$ for redder perovskite thin film

Characterizing perovskite thin films with various $MAPbBr_3$ concentration

Figures below show the characterization of perovskite thin films passivated with a 2D perovskite, with the bulk perovskite fabricated with the addition of various mol% $MAPbBr_3$, ranging down from 10 mol% to 0 mol%. An increase in grain size with decreasing mol% $MAPbBr_3$ is clear in the SEM images of Figure 2-36: at 10 mol%, grain sizes are several hundred nanometers, whereas grain sizes for 2.5 mol%, 0.8 mol%, and 0 mol% samples are in the micrometer range in size. The increase in grain size with decreased $MAPbBr_3$ concentration suggests that $MAPbBr_3$ prevents Oswalt ripening and growth of perovskite grains, which may lead to shorter carrier lifetimes and thus negatively affect device performance.

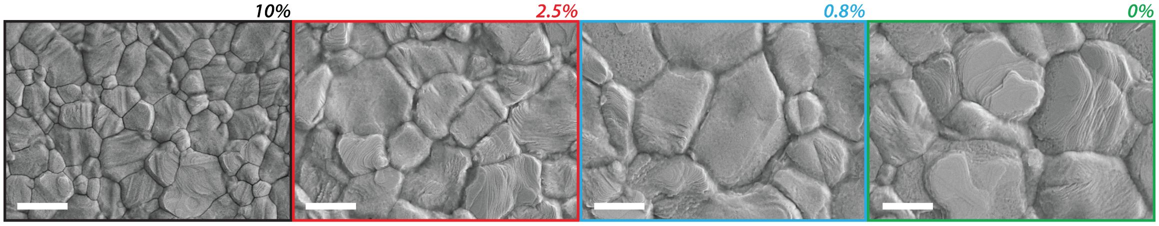

Figure 2-36: SEM images of perovskite thin films with decreasing mol% of added $MAPbBr_3$ (from 10% to 0%). The scale bar is 1 μm.

In addition to changes in grain size and morphology, the absorption onset and the PL peak red-shift (Figure 2-37), which is consistent with a decreased incorporation of $MAPbBr_3$ into the perovskite crystal (Figure 2-38). The PL peak position shifts from 780 nm for 10 mol%, to 797 nm for 2.5 mol%, to 801 nm for 0.8 mol%, and to 803 nm for 0 mol%. This shows that the change in band gap is minimal for perovskites where $MAPbBr_3$ is added below 2.5 mol%. The composition for best device performance can then be determined through intrinsic optoelectronic properties, such as carrier lifetime and effective carrier mobility.

Carrier lifetimes can be determined through fitting time resolved photoluminescence (TRPL) decays to a mono-exponential (Figure 2-39). Films with $MAPbBr_3$ added below 2.5 mol% show significantly longer carrier lifetimes than the 10 mol%

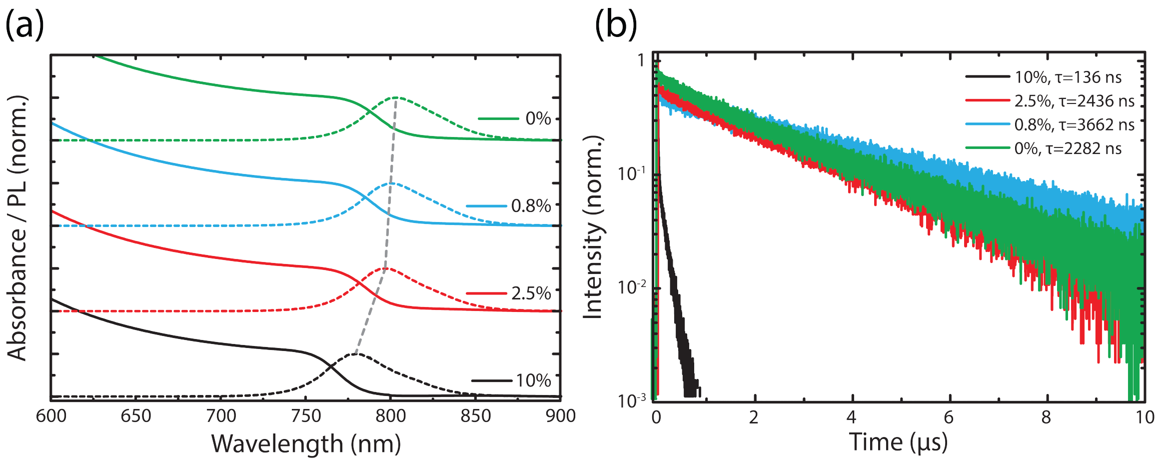

Figure 2-37: (a) UV-Vis absorbance and PL spectra of perovskite thin films with decreasing mol% of added $MAPbBr_3$. (b) TCSPC traces for perovskite thin films with decreasing mol% of added $MAPbBr_3$. Carrier lifetimes in the legend are obtained from a mono-exponential fit.

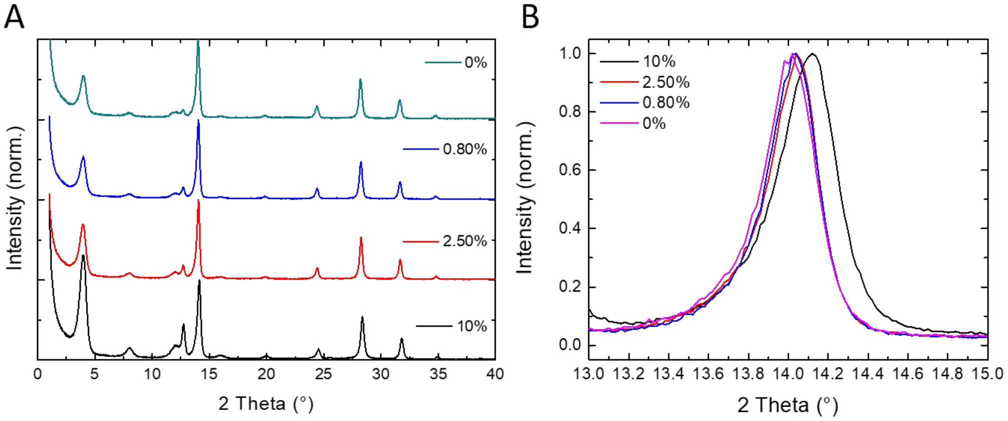

Figure 2-38: Grazing incident XRD (omega 0.3°) of various perovskite thin films. The diffraction pattern from 1-40° (A), and zoomed in (B), showing the shift in the perovskite main peak at 14°.

samples, with the longest carrier lifetimes, exceeding 3.6 μs, observed in 0.8 mol% samples. Carrier lifetimes in the μs range suggest there are few non-radiative pathways and this can lead to a higher V_{OC}. We attribute the long carrier lifetimes to a combination of increased perovskite crystal grain size and surface passivation using the 2D perovskite. Potentially detrimental halide segregation, suspected as carrier trap sites, are reduced at low added Br concentrations and this may also contribute to the increased carrier lifetimes.[25][100]

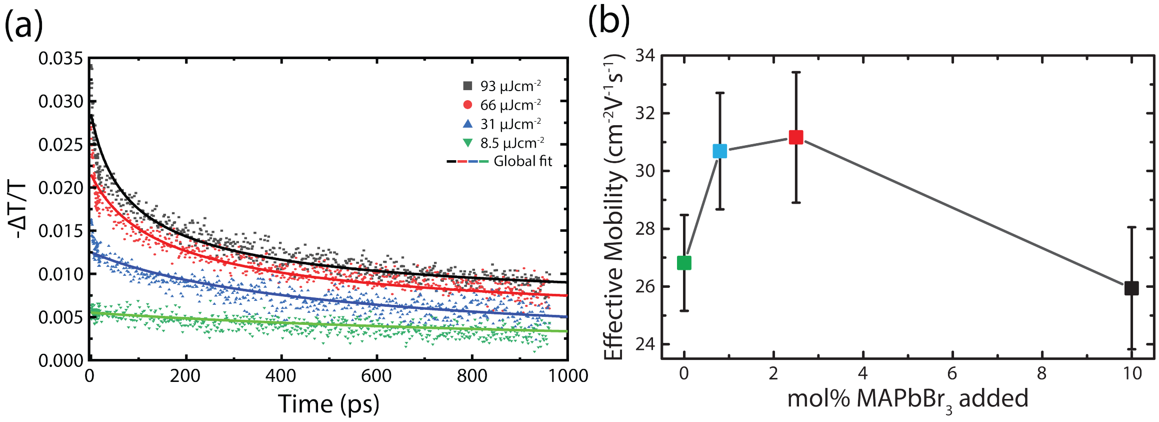

Figure 2-39: (a) OPTP traces for 0.8 mol% added $MAPbBr_3$ showing decay curves at different fluences. (b) Effective mobilities for perovskite thin films determined from OPTP measurements.

In addition to carrier lifetime, device performance is also affected by effective carrier mobilities in the perovskite thin film. Carrier dynamics can be obtained using optical pump-terahertz probe (OPTP) spectroscopy, measuring transient photoconductivity (-ΔT/T) at different carrier densities. Figure 2-39a shows OPTP transient curves for the 0.8 mol% sample (more detail shown in Figure 2-40). At low fluence, the OPTP trace shows a low -ΔT/T due to low carrier densities and slow decay dynamics due to dominant monomolecular recombination. With an increase in fluence, and thus an increase in carrier density, the -ΔT/T increases and the decay trace develops a fast component corresponding to increasing higher order recombinations. An effective mobility can be calculated from the recombination dynamics measured by OPTP.[101] Figure 2-39b plots effective mobilities as a function of mol% added $MAPbBr_3$. Interestingly, the effective mobility increases from 0 mol% to 2.5 mol% (26.8 $cm^2V^{-1}s^{-1}$ to 31.2 $cm^2V^{-1}s^{-1}$), before dropping down to 25.9 $cm^2V^{-1}s^{-1}$ for 10 mol%. The initial increase was unexpected as a previous report suggests that adding bromide leads to lower effective mobilities.[101] This previous report, however, does not probe the low concentration region between 0 mol% and 10 mol%. Indeed, as we have observed for grain sizes (Figure 2-36) and carrier lifetimes (Figure 2-37), this low concentration region can yield large changes in morphologies and carrier dynamics, which correlate with effective mobility. It is also possible that the perovskite crystal orientation, which is known to influence effective mobilities,[102] may also be affected at low concentrations of added MAPbBr$_3$.

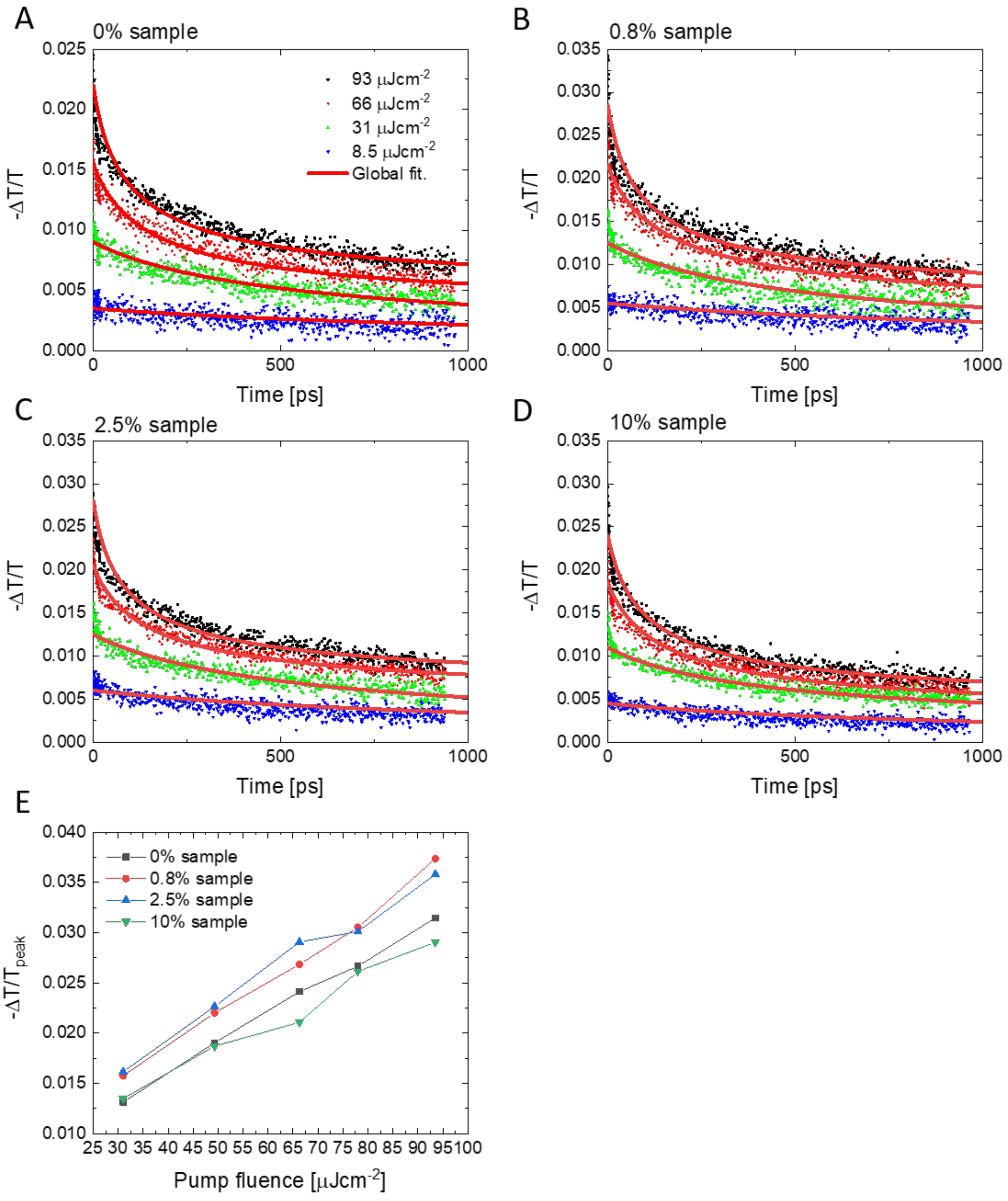

Figure 2-40: Optical-pump terahertz-probe (OPTP) traces for 0 mol% (A), 0.8 mol% (B), 2.5 mol% (C), and 10 mol% (D) of MAPbBr$_3$ added. (E) Plot of $-\Delta T/T_{peak}$ versus pump fluence for all perovskite composition.

Perovskite solar cell device performance

PSCs were fabricated by combining our newly developed SnO_2 ETL and the 3D/2D perovskite layer with improved carrier lifetimes and effective mobilities (0.8 mol%) described above. These PSCs ($\sim$0.1 cm^2) show an average PCE of 24.7%, with some devices exceeding a PCE of 25%, when measured in-house (blue data points, Figure 2-41a). The best performing devices were sent to Newport for certification with the test results shown as the red data points in Figure 2-41a. The champion device measured at Newport achieved a certified PCE of 25.2% from a QSS measurement, with PCEs determined from the JV sweep to be 25.3% and 25.4% for reverse and forward sweep, respectively (Figure 2-41b and Figure 2-42 to 2-45).

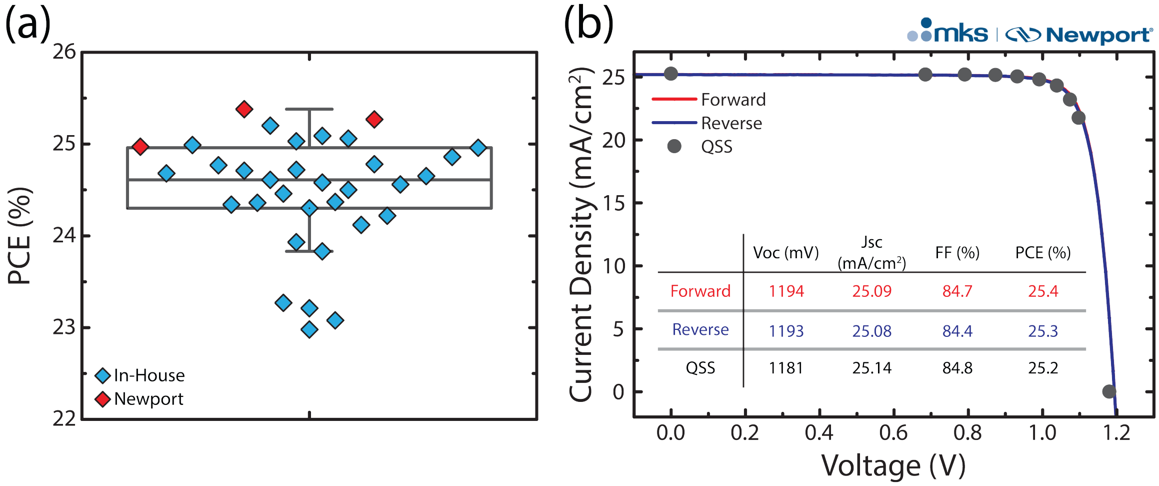

	Voc (mV)	Jsc (mA/cm²)	FF (%)	PCE (%)
Forward	1194	25.09	84.7	25.4
Reverse	1193	25.08	84.4	25.3
QSS	1181	25.14	84.8	25.2

Figure 2-41: (A) Statistical distribution for best performing PSCs (0.0937 cm^2 active area defined by a mask aperture). Devices with high and stable PCEs were then encapsulated and antireflective films were applied before testing at Newport. The blue points are PCE measured in-house and the red points are PCE measured at Newport for certification purposes. (B) JV curves of the champion device measured at Newport, showing both the conventional JV sweep and the certified QSS measurements.

The certified 25.2% PCE result was incorporated in the NREL best research cell efficiency chart (Figure 2-46).[11] We would like to note that the perovskite solar cells are not categorized as “not stabilized” according to the NREL efficiency chart anymore, likely due to employing more rigorous testing standards and improved device reliability. In addition, the certified device showed almost no change in PCE up to 3600 hr of storage (Figure 2-47). Additionally, we tested the stability of one

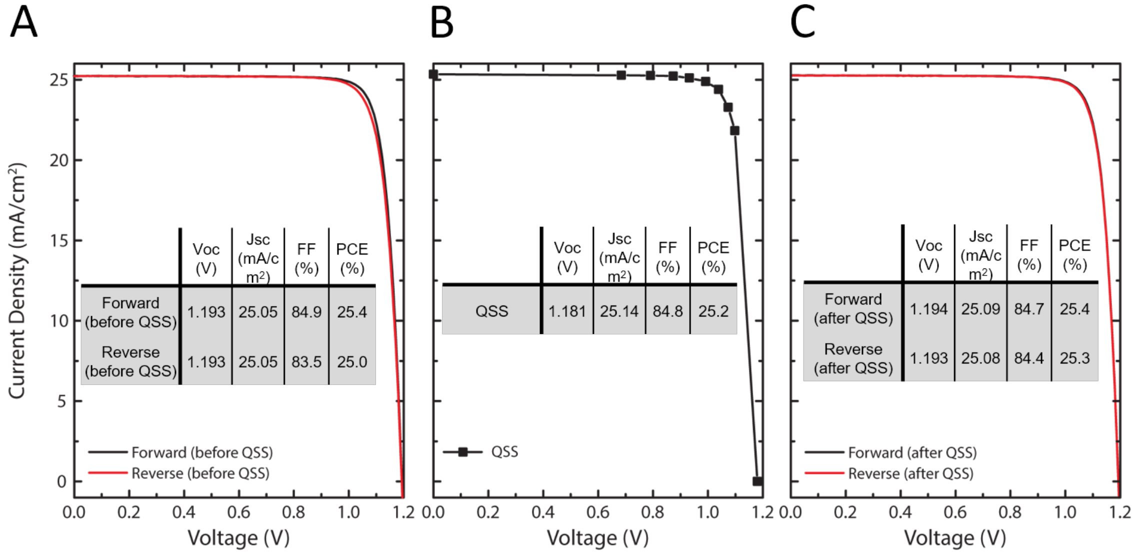

Figure 2-42: Sweep JV curves of the champion PSC before QSS (A), QSS JV curve (B), and sweep JV curve after QSS measurement (C).

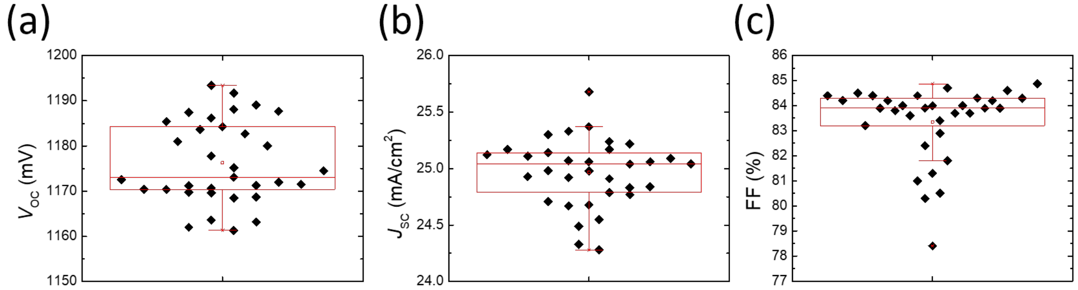

Figure 2-43: Device statistics for the open-circuit voltage (V_{OC}) (A), the short-circuit current density (J_{SC}) (B), and the fill factor (FF) (C) for the best performing devices with pH 1.5 SnO_2 ETL and 0.8 mol% $MAPbBr_3$.

of the devices under continuous light illumination at maximum power point (100 mW/cm², AM1.5G, 45°C), without a UV cut filter and without a cooling system. The encapsulated device retained 80% of its initial PCE after 500 h (Figure 2-48).

The band gap of this record cell, Eg=1.56 eV, was determined from the inflection point of the EQE curve (Eg^{IP}), a method suggested by Krückemeier et al (Figure 2-49).[69] This band gap corresponds to a SQ thermodynamic power conversion efficiency upper limit of 31.3%. At 25.2% PCE our best certified cell is thus at 80.5% of the SQ efficiency limit, which is comparable to the best Si solar cells which are at

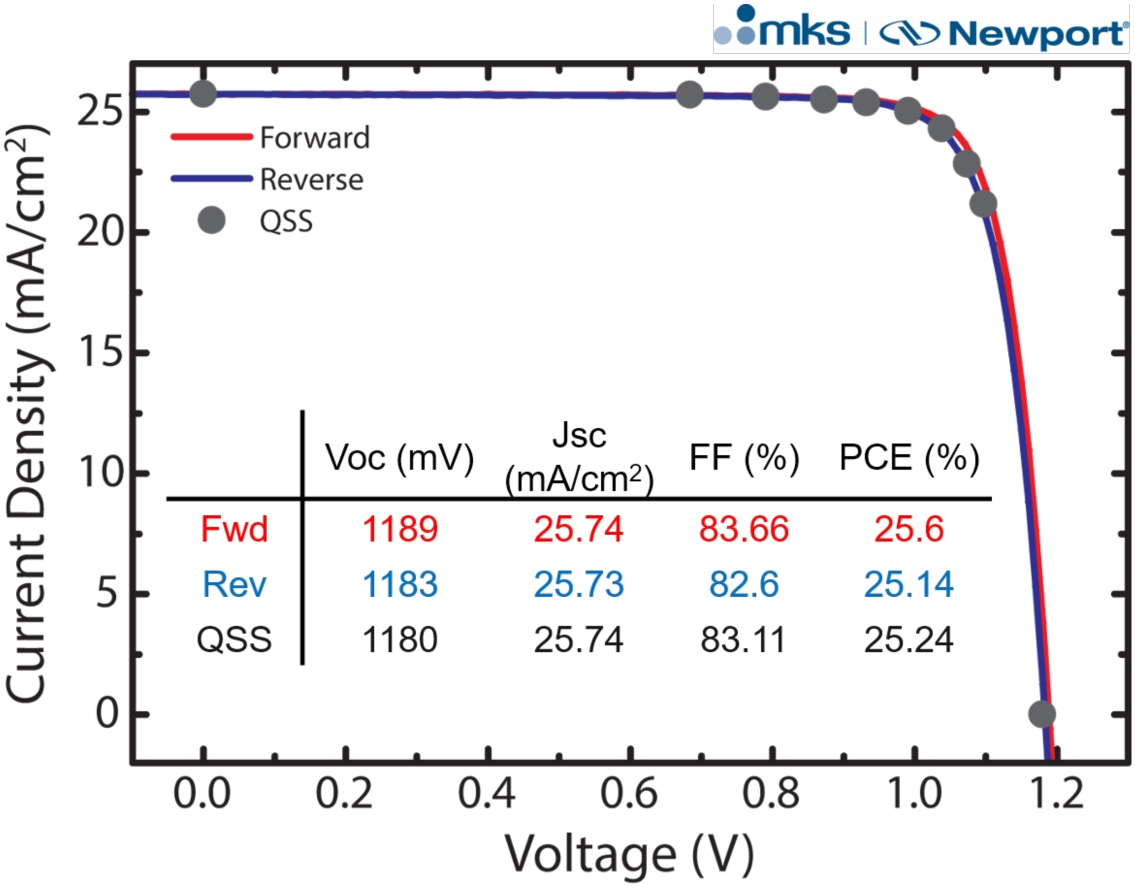

	Voc (mV)	Jsc (mA/cm^2)	FF (%)	PCE (%)
Fwd	1189	25.74	83.66	25.6
Rev	1183	25.73	82.6	25.14
QSS	1180	25.74	83.11	25.24

Figure 2-44: Sweep JV curve and QSS JV curve for champion device shown in Figure 2-41b tested a second time (second of 2 consecutive measurements).

80.9% of the SQ limit.[22]

PSCs with larger areas (~1cm^2) were also fabricated; our champion large-area cell (0.984 cm^2) exhibits PCEs up to 23.0% with high V_{OC} of 1198 mV (Figure 2-50a), which, at this time, are highest PCEs reported for PSCs with an active area of ~1 cm^2.

We attribute the high PCEs of our new cells to major improvements in the V_{OC} and the FF. The radiative V_{OC} limit (V_{OC}^{rad}) is calculated to be 1.270 V from the PV-EQE data (Figure 2-49). [69] With the V_{OC} measured without an aperture mask reaching 1.225 V (Figure 2-51),[29][103] our devices exhibit a V_{OC}/V_{OC}^{rad} ratio up to 96.5%, which is the highest reported thus far for a PSC, and is within striking distance to that for GaAs (97.7%). This low V_{OC} loss suggests that almost all non-radiative recombination pathways have been efficiently eliminated and suggests that

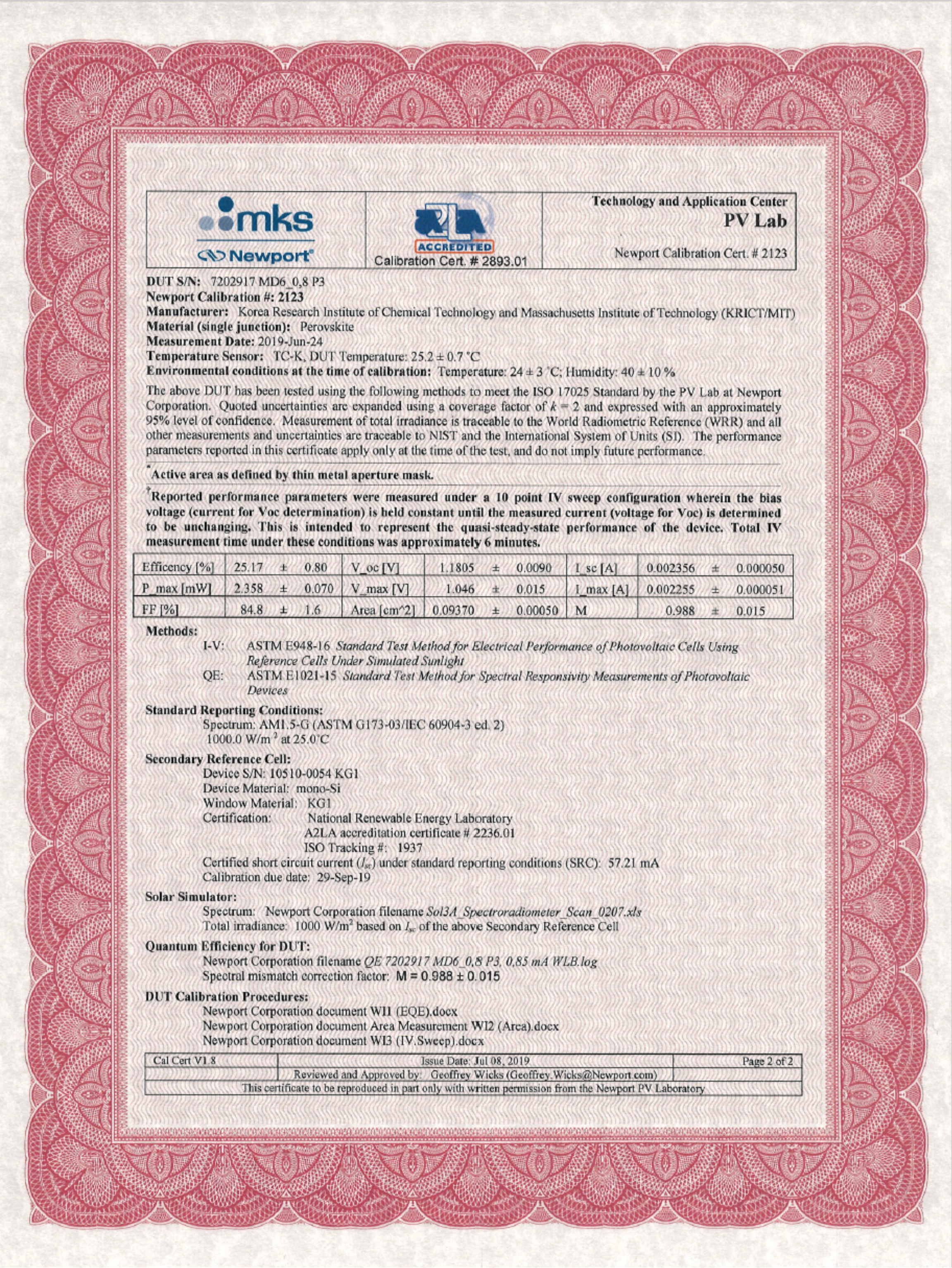

	Calibration Cert. # 2893.01	**Technology and Application Center** **PV Lab** Newport Calibration Cert. # 2123

DUT S/N: 7202917 MD6_0,8 P3
Newport Calibration #: 2123
Manufacturer: Korea Research Institute of Chemical Technology and Massachusetts Institute of Technology (KRICT/MIT)
Material (single junction): Perovskite
Measurement Date: 2019-Jun-24
Temperature Sensor: TC-K, DUT Temperature: 25.2 ± 0.7 °C
Environmental conditions at the time of calibration: Temperature: 24 ± 3 °C; Humidity: 40 ± 10 %

The above DUT has been tested using the following methods to meet the ISO 17025 Standard by the PV Lab at Newport Corporation. Quoted uncertainties are expanded using a coverage factor of $k = 2$ and expressed with an approximately 95% level of confidence. Measurement of total irradiance is traceable to the World Radiometric Reference (WRR) and all other measurements and uncertainties are traceable to NIST and the International System of Units (SI). The performance parameters reported in this certificate apply only at the time of the test, and do not imply future performance.

---

[*] **Active area as defined by thin metal aperture mask.**

[†] **Reported performance parameters were measured under a 10 point IV sweep configuration wherein the bias voltage (current for Voc determination) is held constant until the measured current (voltage for Voc) is determined to be unchanging. This is intended to represent the quasi-steady-state performance of the device. Total IV measurement time under these conditions was approximately 6 minutes.**

Efficency [%]	25.17 ± 0.80	V_oc [V]	1.1805 ± 0.0090	I_sc [A]	0.002356 ± 0.000050
P_max [mW]	2.358 ± 0.070	V_max [V]	1.046 ± 0.015	I_max [A]	0.002255 ± 0.000051
FF [%]	84.8 ± 1.6	Area [cm^2]	0.09370 ± 0.00050	M	0.988 ± 0.015

Methods:
I-V: ASTM E948-16 *Standard Test Method for Electrical Performance of Photovoltaic Cells Using Reference Cells Under Simulated Sunlight*
QE: ASTM E1021-15 *Standard Test Method for Spectral Responsivity Measurements of Photovoltaic Devices*

Standard Reporting Conditions:
Spectrum: AM1.5-G (ASTM G173-03/IEC 60904-3 ed. 2)
1000.0 W/m^2 at 25.0°C

Secondary Reference Cell:
Device S/N: 10510-0054 KG1
Device Material: mono-Si
Window Material: KG1
Certification: National Renewable Energy Laboratory
A2LA accreditation certificate # 2236.01
ISO Tracking #: 1937
Certified short circuit current (I_{sc}) under standard reporting conditions (SRC): 57.21 mA
Calibration due date: 29-Sep-19

Solar Simulator:
Spectrum: Newport Corporation filename *Sol3A_Spectroradiometer_Scan_0207.xls*
Total irradiance: 1000 W/m^2 based on I_{sc} of the above Secondary Reference Cell

Quantum Efficiency for DUT:
Newport Corporation filename *QE 7202917 MD6_0,8 P3, 0,85 mA WLB.log*
Spectral mismatch correction factor: M = 0.988 ± 0.015

DUT Calibration Procedures:
Newport Corporation document WI1 (EQE).docx
Newport Corporation document Area Measurement WI2 (Area).docx
Newport Corporation document WI3 (IV.Sweep).docx

Cal Cert V1.8	Issue Date: Jul 08, 2019	Page 2 of 2
	Reviewed and Approved by: Geoffrey Wicks (Geoffrey.Wicks@Newport.com)	
This certificate to be reproduced in part only with written permission from the Newport PV Laboratory		

Figure 2-45: Certification of a PSC efficiency exhibiting stabilized efficiency of 25.2% obtained from a device with pH 1.5 SnO_2 ETL and 0.8 mol% $MAPbBr_3$.

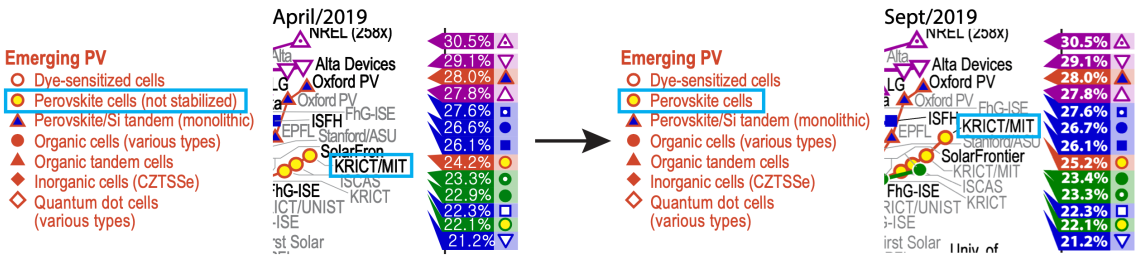

Figure 2-46: Solar cell efficiency chart published by NREL. The PSCs are no longer categorized as "not stabilized" as of September 2019.

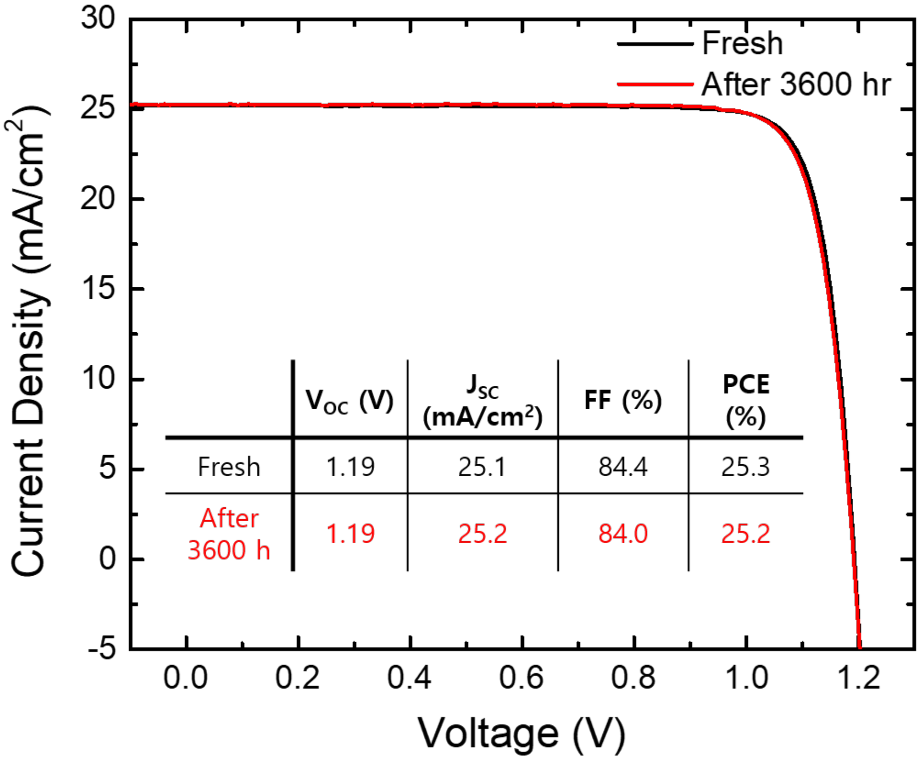

	V_{OC} (V)	J_{SC} (mA/cm^2)	FF (%)	PCE (%)
Fresh	1.19	25.1	84.4	25.3
After 3600 h	1.19	25.2	84.0	25.2

Figure 2-47: In-house measurements of reverse JV sweep and device data of the certified PSC, measured 3600 hr after certification at Newport.

these PSCs should be highly luminescent when operated as a light-emitting diode, as we find below.

Figure 2-50b shows a plot of EL_{EQE} and external luminescence energy conversion efficiency (EL_{ECE}) versus voltage of a PSC measured under forward bias (J and radiance versus voltage is shown in Figure 2-52). We observe an EL_{EQE} up to

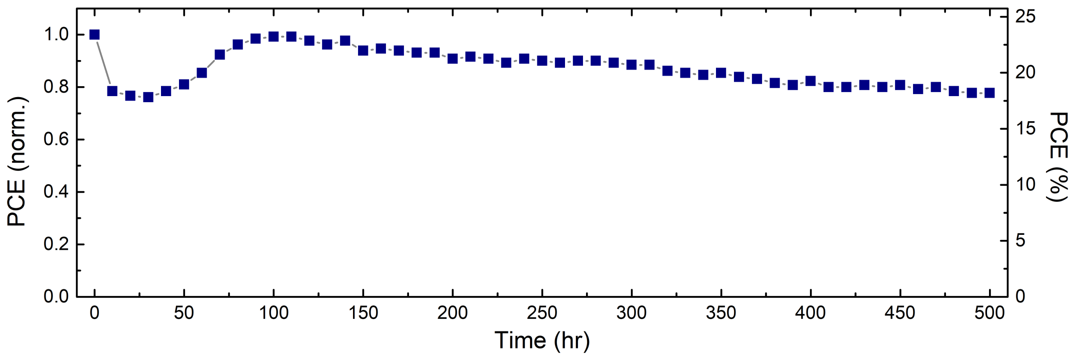

Figure 2-48: Long-term photostability test under AM 1.5G solar irradiation in a N2 purged chamber at 45 °C.

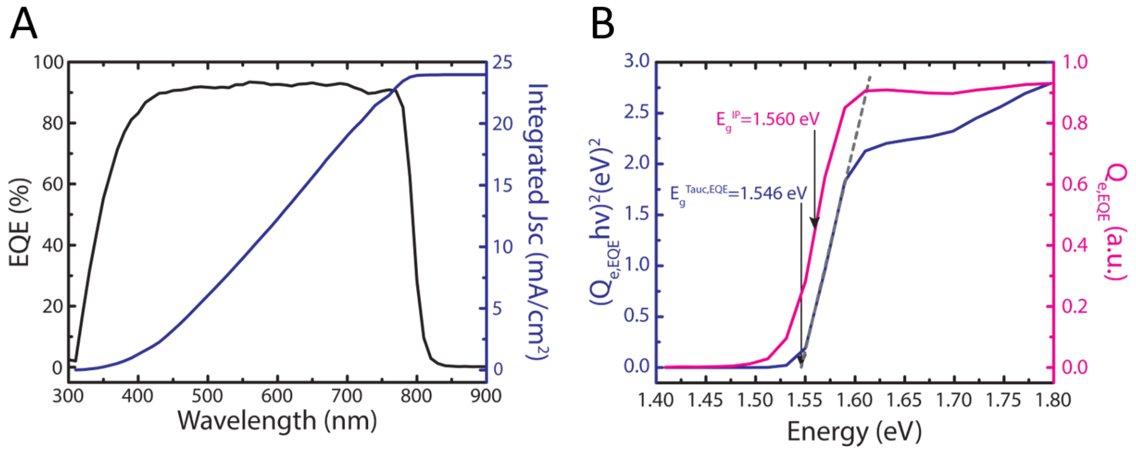

Figure 2-49: (A) EQE, and integrated J$_{SC}$ of the champion device shown in Figure 2-41b. (B) band gap analysis of the champion device.

17.2%, which approaches the efficiency of perovskite LEDs that are engineered specifically for light emission with thin (~100 nm) emitting layers and small grain sizes [104][105][106], whereas our devices have perovskite active layer thickness of ~600 nm, with grain sizes exceeding micrometers. In addition, due to early sub-band gap turn-on, likely from thermal carriers, our PSCs exhibits a peak EL$_{ECE}$ up to 21.6%.

In addition to a record low V$_{OC}$ loss and high luminescence efficiency, our devices exhibit a high FF up to 84.8%; a value this high has only been reported in much more mature technologies, such as Si and GaAs. This high FF is a result of improved carrier mobility in the perovskite active layer and better charge collection with the newly developed SnO$_2$ ETL with minimum parasitic losses from shut and series resistances.

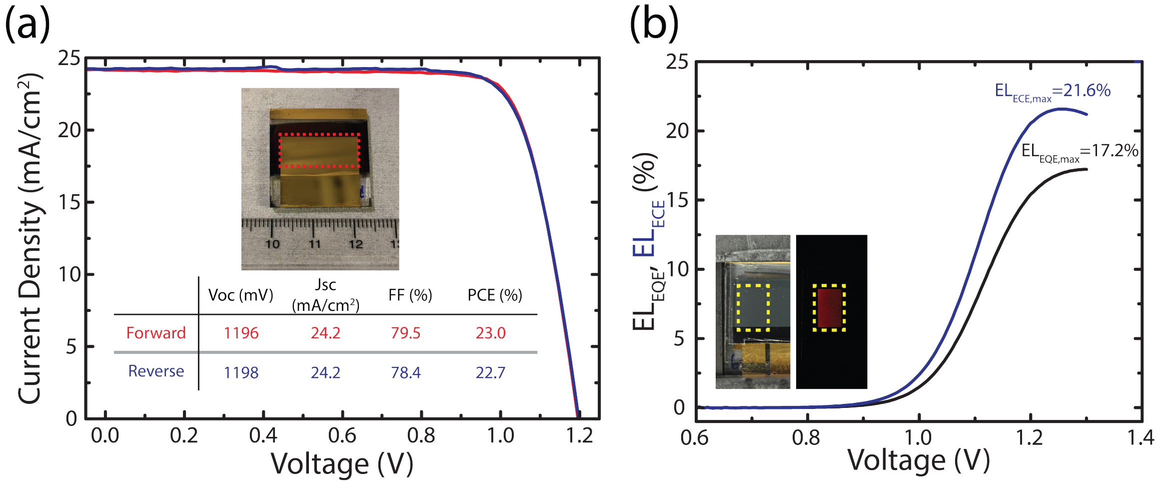

	Voc (mV)	Jsc (mA/cm^2)	FF (%)	PCE (%)
Forward	1196	24.2	79.5	23.0
Reverse	1198	24.2	78.4	22.7

Figure 2-50: (a) JV curves of a larger area PSC exhibiting PCE up to 23%. The active area is 0.984 cm^2, defined by a mask aperture. The inset is a photograph of the device, where the dotted outline approximates the mask aperture. (b) Electroluminescence EQE and ECE of our PSC under forward bias.

For further improvement in FF, future research should be focused on minimizing trap-assisted recombination to approach the the SQ limit FF (FF^{SQ}) of ∼90%.

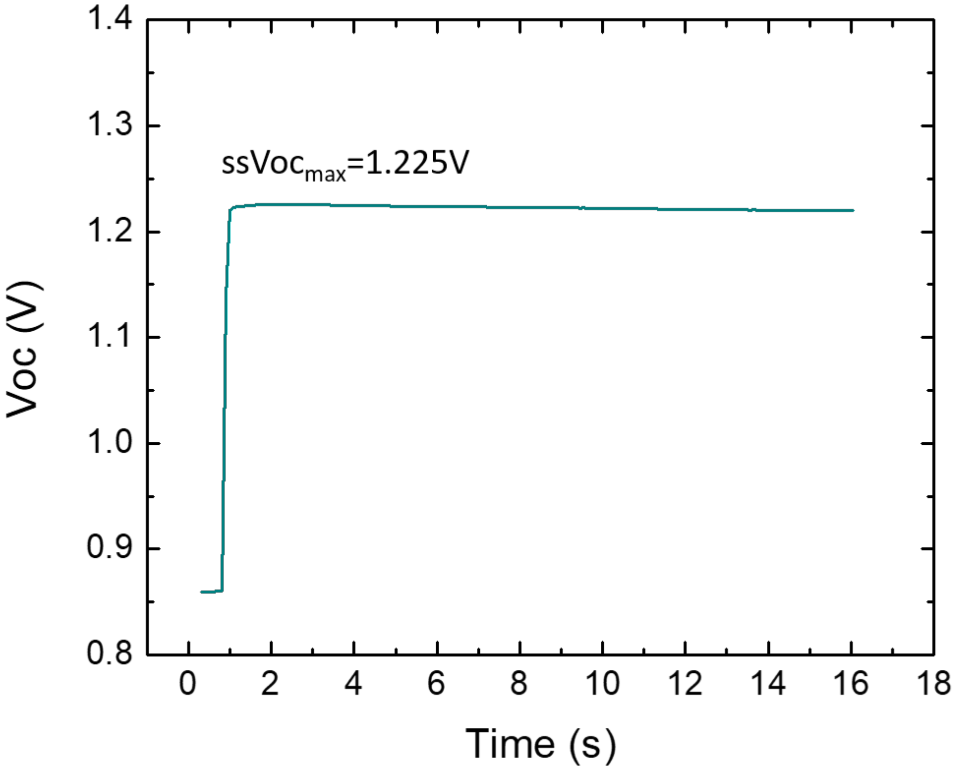

Figure 2-51: Plot of steady-state V_{OC} (ssV_{OC}) versus time. The ssV_{OC} was measured without a mask and the entire active area was illuminated.

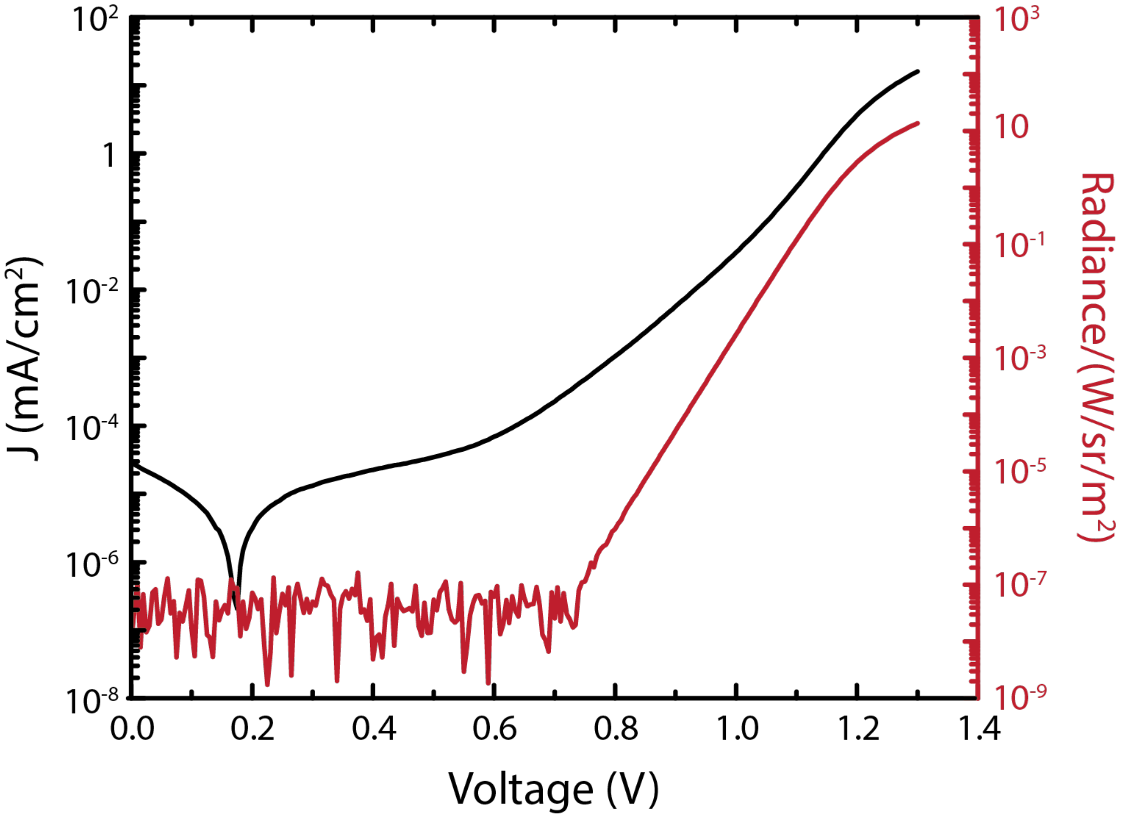

Figure 2-52: Plot of current density (J) and radiance versus voltage.

2.4 PV Characterization

2.4.1 JV Sweep vs Quasi steady-state measurement

Perovskite is a soft material where the crystal lattice is stabilized via ionic bonding. Compared to covalently bonded structures, such as Silicon and GaAs, the ions in the perovskite are highly mobile and is responsive to external stimuli, such as heat, voltage bias, and light. For solar cell applications, the ion migration upon voltage bias exhibits in a hysteresis when performing a JV sweep (Figure 2-53a). A hysteresis in a JV curve is the discrepancy in the device parameters, usually in FF for perovskite solar cells, between a forward JV sweep (from short-circuit to open-circuit) and a reverse JV sweep (from open-circuit to short-circuit). For perovskite solar cells hysteresis is most likely due to ion migrations not stabilizing within the measurement time window.

Figure 2-53a shows a JV curved that can be obtained by performing a conventional JV sweep (forward: red trace, reverse: blue trace) that exhibits a hysteresis. Note that depending on the device structure, either the forward JV curve or the reverse JV curve has a higher FF and PCE. Also, some devices are sweep rate sensitive in that the JV curves and the device performance change with different sweep rate (usually ranging from 10-1000 mV/s). The maximum power point (MPP), where the current density and voltage that generates the maximum power, is most often situated between the two JV curves (orange circle). Thus, it is difficult to determine the actual power (or the efficiency) that the device will generate with a device that exhibits severe hysteresis. However, it is important to note that a device that exhibits hysteresis is not a "bad" device, but rather simply exhibits hysteresis behavior.

Starting a few years ago, a more robust measurement was starting to be adopted by the perovskite community. It's a quasi steady-state (QSS) measurement and it is shown in Figure 2-53b. The QSS measurement is different from the conventional JV sweep in that is does not rely on the system to adjust the sweep rate to find the parameters that results in minimum hysteresis but rather let the device stabilize and run its course. In a QSS measurement, the bias voltage is held at a certain voltage

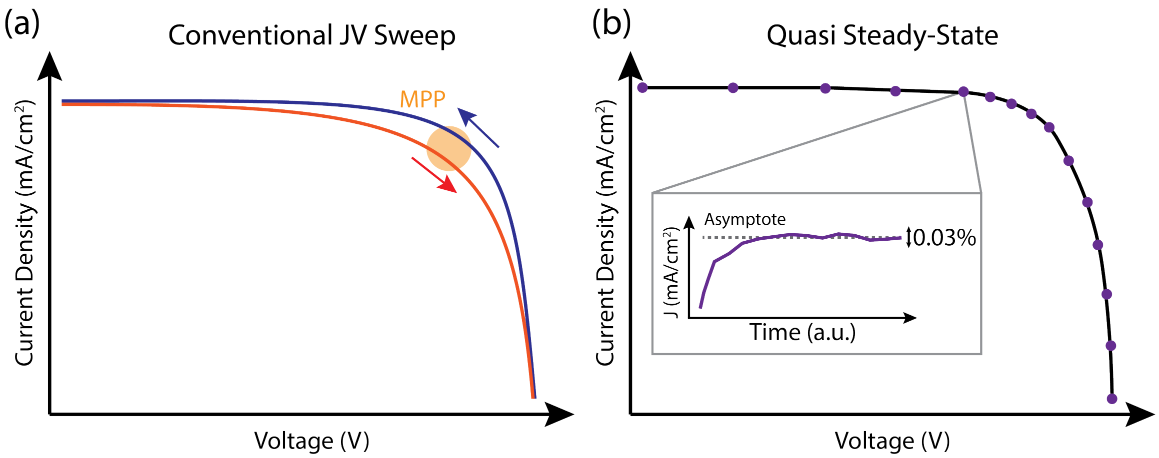

Figure 2-53: (a) A JV curved obtained via conventional JV sweep that exhibits hysteresis. The MPP is found between the two JV curves. (b) A quasi steady-state (QSS) measurement. Both plots are not real data and for illustration purposes.

and wait for the current density to stabilize within a set threshold (0.03% is used for our devices at Newport) until moving to the next voltage. The voltage range and the points (13 voltage points are used for our devices) are usually determined by using a JV sweep result as a reference and the voltage points are positioned more tightly in the range where we expect MPP. The QSS measurement takes into account the dynamic of the ion migrations and is adopted to eliminate device's sensitivity towards sweep rate, pre-conditioning, and etc.

A stabilized power output (SPO) is also a widely used measurement technique to find the maximum power a device can reliably output. SPO is usually determined by first performing the JV sweep and holding at V_{max} and measuring the current density, or the V_{max} can be dithered to track the maximum power point. While this should be more accurate and reliable than a conventional JV sweep to find the true power point and the efficiency, it lacks the information on the rest of the device parameters, such as the J_{SC}, FF, and V_{OC}.

2.4.2 Photoluminescence and Electroluminescence Characterization

Photoluminescence quantum yield (PLQY) is one of the most important metric for PV and also for LED and it sets an upper limit on the device efficiency. For both PV and LED, the maximum device efficiency is capped when the PLQY is 100%. From Chapter 1, the expression for PLQY is,

$$PLQY = \frac{k_2 n}{k_1 + k_2 n + k_3 n^2}$$

Here, k_2 is the sole radiative recombination rate (bimolecular recombination). PLQY can be thought of as the competition between non-radiative (k_1 and k_3) and radiative recombination (k_2) and the relative ratio between the two defined the PLQY.

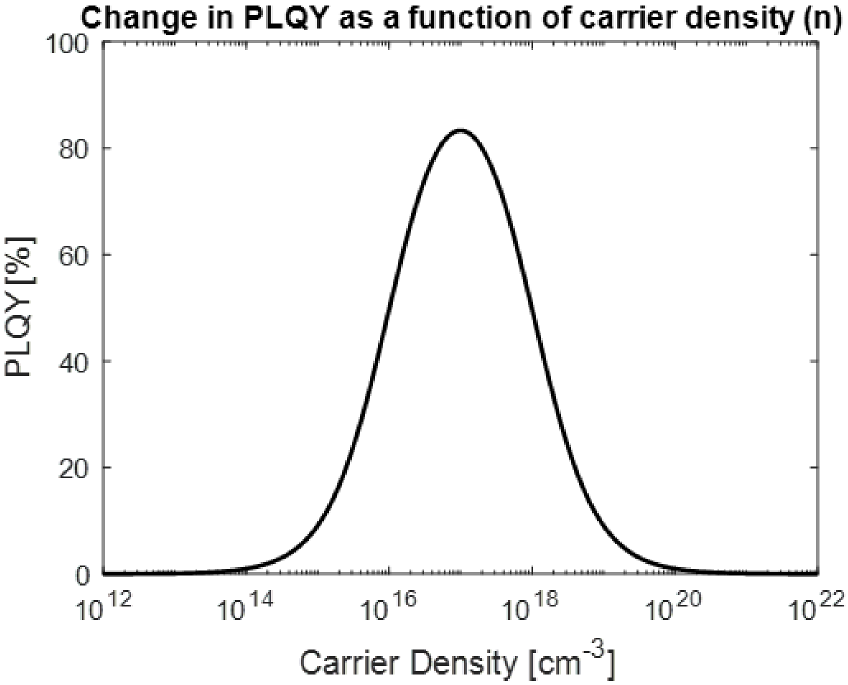

Figure 2-54: Plot of PLQY versus carrier density with $k_1=10^6$ s^{-1}, $k_2=10^{-10}$ cm^3s^{-1}, $k_3=10^{-28}$ cm^6s^{-1}.

The PLQY is also a function of carrier density (n) (Figure 2-54). With increase in the carrier density (n), the PLQY increases and reaches a peak, before decreasing. The increase in the PLQY is due to increase in the contribution from the radiative recombination rate, k_2, while the decrease in the PLQY past the peak is due to Auger recombination (k_3) being more dominant at higher carrier density.

Figure 2-55a is showing the plot of PLQY as a function of carrier density with varying radiative recombination rates (k_2). With increase in k_2, the maximum PLQY is increases and the full-width-half-max (FWHM) is wider, allowing wider range of carrier density with high PLQY. Figure 2-55b shows the plot of PLQY with fixed k_2 but with varying k_1, the monomolecular non-radiative recombination. The trend is the opposite of what we see from Figure 2-55a; the maximum PLQY and broader FWHM is observed with decreasing k_1.

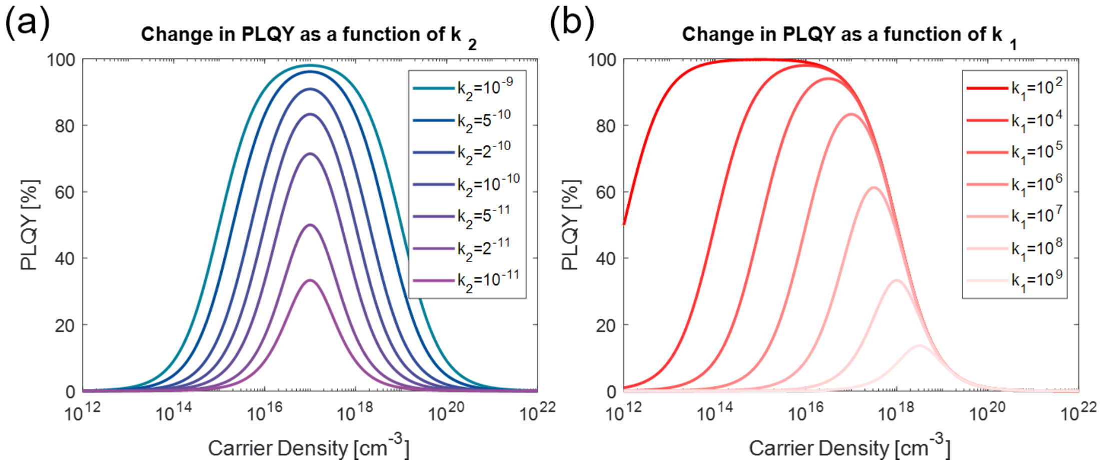

Figure 2-55: (a) Plot of PLQY versus carrier density with various k_2 values ranging from 10^{-9}-10^{-11} cm^3s^{-1} with k_1=10^6 s^{-1} and k_3=10^{-28} cm^6s^{-1}. (b) Plot of PLQY versus carrier density with various k_1 values ranging from 10^2-10^9 s^{-1} with k_2=10^{-10} cm^3s^{-1} and k_3=10^{-28} cm^6s^{-1}.

Here, I will relax the definition of both the PLQY and EL EQE as these metrics measure the fraction of either $\frac{\text{photon out}}{\text{photon in}}$ and $\frac{\text{photon out}}{\text{charge carrier in}}$, with the assumption that the physical meaning of one photon is equivalent to one charge carrier in LEDs. This is to come to the conclusion that both the PLQY and EL EQE has the same relationship with respect to V_{OC}. Then we can find the relationship between the PLQY (ultimately the EL EQE) and the V_{OC} of the device through the Reciprocity Theorem. [23] The expression for EL EQE (or EQE_{LED}) is,

$$EQE_{LED} = \frac{J_{emission}}{J_{injected}}$$

Using the diode equation, we can express $J_{emission}$ as,

$$J_{emission} \approx J_{emission,0} e^{\frac{qV}{kT}}$$

By combining the above two equations and setting $V=V_{OC}$,

$$EQE_{LED} = \frac{J_{emission,0} e^{\frac{qV}{kT}}}{J_{injected}}$$

$$ln(EQE_{LED}) = \frac{qV_{OC}}{kT} + ln\frac{J_{emission,0}}{J_{injection}}$$

In open-circuit condition, the injected current density ($J_{injection}$) is equal to the short-circuit current density (J_{SC}) since the total current density (J_{total}) is zero. By substituting $J_{injection}$ with J_{SC},

$$ln(EQE_{LED}) = \frac{qV_{OC}}{kT} + ln\frac{J_{emission,0}}{J_{SC}}$$

$$\frac{kT}{q} ln(EQE_{LED}) = V_{OC} - \frac{kT}{q} ln\frac{J_{SC}}{J_{emission,0}}$$

$$\frac{kT}{q} ln(EQE_{LED}) = V_{OC} - V_{OC}^{rad}$$

where V_{OC}^{rad} is the nominal V_{OC} from Chapter 1.2.1. Thus, we write the final expression,

$$V_{OC} = V_{OC,rad} + \frac{kT}{q} ln(EQE_{LED})$$

$$V_{OC} = V_{OC,rad} + \frac{kT}{q} ln(PLQY))$$

where unity for EQE_{LED} and PLQY is 1. An order of magnitude improvement in the EQE_{EL} and PLQY translates to ∼60 mV increase in the V_{OC}.

Common mistakes in measuring PLQY and EQE$_{EL}$

Due to the reciprocity relationship, one would expect to measure the PLQY of the newly synthesized samples as a way to accelerate the screen processing for potential candidates that would result in high device efficiencies. While the improvements in the PLQY will most likely lead to better device performance, I'd like to emphasize some important caveats.

First, the perovskite solar cell is composed of multiple layers and not just the perovskite active layer. This means that the high PLQY that may be observed in a stand-alone perovskite thin film may not translate to high PLQY with the addition of top and bottom transport layers. This is often observed if the interface between the perovskite layer and the transport layer is not well passivated and is full of defects. While the PLQY of the perovskite thin film needs to be high by itself, a device structure where the PLQY of the semi-stack or a full-stack (without the metal contact) is high is more important and also relevant for high device efficiency. On the other hand, adding a thick insulating layer may retain the high PLQY of the perovskite active layer but will not translate to high device efficiency due to severe parasitic resistance. Thus, the overall device structure along with the PLQY of the whole device stack needs to be considered.

Second, when measuring the V$_{OC}$ of the perovskite solar cell to cross-check with the EQE$_{EL}$, it is important to measure the V$_{OC}$ without a shadow mask and fully illuminate the entire device pad. While a shadow mask with a defined aperture is used when measuring the JV curve and calculating the PCE of the solar cell, it leads to larger contribution of the dark current (J$_{emission,0}$) from the covered area of the active area. For example, if a 0.1 cm^2 aperture is used on a 0.32 cm^2 active area, $\frac{kT}{q} log \frac{0.1}{0.32} \approx -30mV$ of V$_{OC}$ penalty is applied. This will underestimate the EQE$_{EL}$ by a factor of ~3.2.[103]

2.5 Future Directions

2.5.1 Efficiency

Due to the collective efforts from the perovskite scientific community to improve the device performance, the perovskite solar cell is now at a stage where it may be able to compete with traditional solar cell technologies due to its high efficiency and low fabrication cost. Some might say the efficiency of the perovskite solar cell is high enough and that we should focus our research to improve other metrics, such as stability and scalability, to truly realize large scale commercialization of perovskite solar cells. While there may be a diminishing return in further improving the efficiency, this shouldn't prevent us from exploring ways to enhance the device performance to enrich scientific knowledge of the perovskite solar cell system. By analyzing the device parameters for the best performing perovskite solar cell and comparing to the theoretical limit, we can get an idea of which parameter is the bottleneck and should gain the most attention for further improvements.

Figure 2-56 shows the device data point for the current record 25.2% that was established through collaboration with our group and KRICT. The percentage in blue is roughly how close it is to the maximum value. What we see is that all three device parameters (V_{OC}, J_{SC}, and FF) are roughly the same fraction of the maximum values, meaning they are equally good (or maybe bad?), and is equally responsible for the PCE deficit.

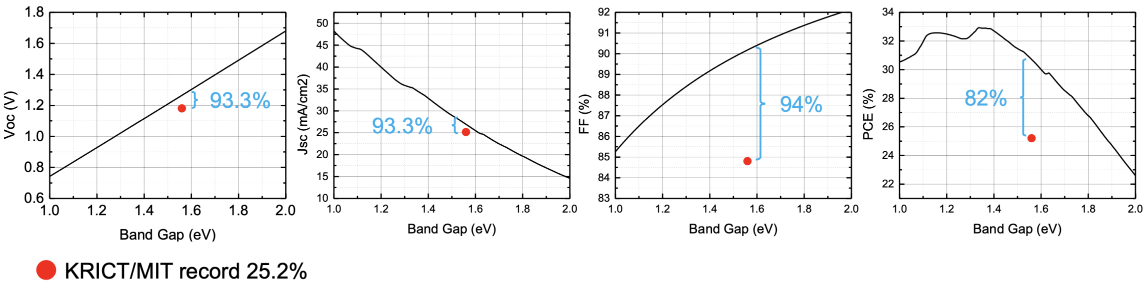

Figure 2-56: Plot of four device metrics (V_{OC}, J_{SC}, FF, and PCE) along with curve of theoretical maximum.

This suggests we need to find a strategy to improve the general performance of the perovskite solar cell rather than focusing on a single device metric, such as V_{OC}, to improve the PCE. As the all device metrics are within 93% of its maximum value, it is likely that a laser focused strategy to improve one metric may negatively affect other metrics and doesn't result in overall improvement, or even decrease the PCE.

One avenue that is worth looking into is Pb-Sn hybrid perovskite solar cell. Adding Sn to the Pb based perovskite results in a much lower band gap semiconductor, allowing fabrication of perovskite solar cells with band gap approaching the "sweet-spot" of ∼1.4 eV. Current focus on Pb-Sn perovskite solar cell has been to stabilze the oxidation state of Sn^{2+} as it is prone to oxidation and become Sn^{4+}, which forms a trap state. Currently, the device performance of Pb-Sn hybrid perovskite solar cell is behind that of the Pb only devices. However, I anticipate much improvements on the device performance and stability of the Pb-Sn hybrid perovskite solar cells and look forward to its progress in the next 3-5 years.

2.5.2 Long-term Stability

A solar cell is expected to reliably generate a predictable amount of power over a long period time. Improving long-term stability of the perovskite solar cell is arguably the hardest research challenge but one of the most important aspect of the technology to push into commercialization. It is particularly challenging due to slow feedback in stability results.

A typical perovskite solar cell requires a couple of days of fabrication and one can measure the performance to check whether a certain treatment or strategy has resulted in improved device performance. Many testing can be done in parallel, which accelerate the screening process. However, a typical long-term stability lasts for 1000 hours, or even several months, to obtain data on the device stability.

In addition, testing multiple devices in parallel is a challenge as setting up a testing station with a large solar simulator with stable light output for several weeks is highly expensive. This forces many researchers to test single device at a time and therefore prevents sufficient data accumulation for statistical analysis.

Lastly, the degradation in device performance during long-term stability is a multi-dimensional problem. In most cases, the degradation is the sum of failure from several layers of the full device stack, while some layers may be more responsible and prone to degradation than other layers. As a result, switching out one component of the device to a different material or design may not solve the overall problem.

Currently, the research on the long-term stability is highly empirical with slow feedback turn-over. An accelerated testing method without complicated experimental set up is highly desirable to lower the barrier to these test and make them more prevalent. This will allow collection of many stability data with hopefully statistical analysis that will guide us in the right direction for developing highly stable perovskite solar cells.

A potential method is to use electroluminescence as a metric and to track the degradation of electroluminescence instead of PCE. In general, the stability of the electroluminescence efficiency of the perovskite solar cell is much less than that of

PCE; tens of minutes for EL to decrease 80% of its initial efficiency compared to hundreds of hours for solar cell's PCE. This allows faster turn-over in feedback, allowing us to screen device structures or strategies faster. Also, an EL set up is much simpler than a solar cell testing set up is more affordable to test many devices in parallel.

Using EL as the accelerated stability testing platform requires the degradation mechanism under LED condition (under forward bias) to be the same as the degradation mechanism under solar cell condition (under reverse bias). However, it is unlikely that an improved LED stability of a PV structure exhibits less stable PV performance.

2.5.3 Scalability

A solar cell technology that can be solution processed has a relatively lower entry for commercialization due to ease of fabrication at the comfort of having wide range of solution processing techniques. The ultimate dream is to be able to fabricate solar cells like printing newspaper at high speed! To take advantage of this, much effort is put into developing fabrication techniques that would allow scale-up fabrication of perovskite solar cells. Unfortunately, the scale-up fabrication of perovskite solar cell introduces faces new challenges that is preventing achieving high efficiency large area modules.

Figure 2-57 shows the efficiency of Silicon, GaAs, and perovskite solar cells with each solar cell showing the unit cell (active area $<10\text{cm}^2$) and module (>800 cm^2). Silicon and GaAs solar cells show comparable efficiency between the unit cell and the module, with less than 15% relative difference between the two. However, that difference is much greater for the perovskite solar cell in unit cell and module size, up to 36%. Here, I'd like to note that the discrepancy in the efficiency between the unit cell and the module is not solely due to poor scalability in fabrication but is also due to difference in device structure, material choice, and etc.

There are many reasons as to why the scale-up fabrication of perovskite solar cell is challenging. For example, harsh processing that is possible for small unit cell sizes, such as thermal treatment at >500 °C for meso-TiO_2, may not be appropriate for large area substrates. Also, the deposition and crystallization protocols that are responsible high quality perovskite active layer during spin-coating process may not be directly translatable to large-area deposition methods, such as blade-coating and ink-jet printing. To achieve the same high quality perovskite active layer, different processing protocols need to be developed in vastly different parameters spaces, resulting in delay in development.

Research on the scalability aspect of the perovskite solar cell development should be focus on understanding the effect of different processing conditions on the quality of the perovskite active layer, using a high quality perovskite thin film that is fabricated

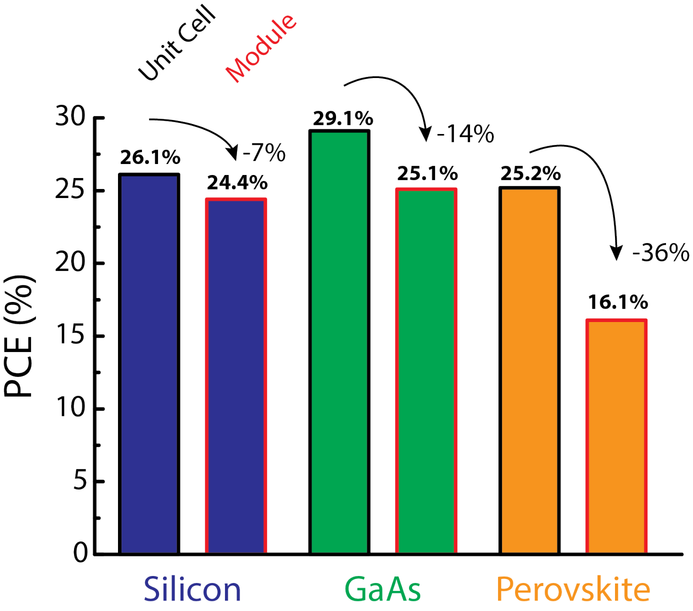

Figure 2-57: Plot of best unit cell efficiency and module efficiency for Silicon, GaAs, and perovskite solar cell. The data is extracted from the NREL efficiency chart.

via spin-coating method as the standard reference. Also, the effect of inhomogeneity of the optoelectronic properties of the layers, both in micro and macro scale, on the overall device performance need to be investigated. A large area photoluminescence and electroluminescence imaging could be a useful tool for this purpose.

Bibliography

[1] Martin Kaltenbrunner, Getachew Adam, Eric Daniel Głowacki, Michael Drack, Reinhard Schwödiauer, Lucia Leonat, Dogukan Hazar Apaydin, Heiko Groiss, Markus Clark Scharber, Matthew Schuette White, Niyazi Serdar Sariciftci, and Siegfried Bauer. Flexible high power-per-weight perovskite solar cells with chromium oxide-metal contacts for improved stability in air. *Nature Materials*, 14(10):1032–1039, 10 2015.

[2] Robert M. Pasquarelli, David S. Ginley, and Ryan O'Hayre. Solution processing of transparent conductors: From flask to film, 11 2011.

[3] Shuxia Tao, Ines Schmidt, Geert Brocks, Junke Jiang, Ionut Tranca, Klaus Meerholz, and Selina Olthof. Absolute energy level positions in tin- and lead-based halide perovskites. *Nature Communications*, 10(1):1–10, 12 2019.

[4] Handong Jin, Elke Debroye, Masoumeh Keshavarz, Ivan G. Scheblykin, Maarten B.J. Roeffaers, Johan Hofkens, and Julian A. Steele. It's a trap! on the nature of localised states and charge trapping in lead halide perovskites, 2 2020.

[5] Akihiro Kojima, Kenjiro Teshima, Yasuo Shirai, and Tsutomu Miyasaka. Organometal Halide Perovskites as Visible-Light Sensitizers for Photovoltaic Cells. *Journal of the American Chemical Society*, 131(17):6050–6051, 5 2009.

[6] Michael M. Lee, Joël Teuscher, Tsutomu Miyasaka, Takurou N. Murakami, and Henry J. Snaith. Efficient hybrid solar cells based on meso-superstructured organometal halide perovskites. *Science*, 338(6107):643–647, 11 2012.

[7] Nam Joong Jeon, Jun Hong Noh, Young Chan Kim, Woon Seok Yang, Seungchan Ryu, and Sang Il Seok. Solvent engineering for high-performance inorganic–organic hybrid perovskite solar cells. *Nature Materials*, 13(9):897–903, 9 2014.

[8] Nam Joong Jeon, Jun Hong Noh, Woon Seok Yang, Young Chan Kim, Seungchan Ryu, Jangwon Seo, and Sang Il Seok. Compositional engineering of perovskite materials for high-performance solar cells. *Nature*, 517(7535):476–480, 1 2015.

[9] Michael Saliba, Taisuke Matsui, Ji-Youn Seo, Konrad Domanski, Juan-Pablo Correa-Baena, Mohammad Khaja Nazeeruddin, Shaik M. Zakeeruddin, Wolfgang Tress, Antonio Abate, Anders Hagfeldt, and Michael Grätzel. Cesium-containing triple cation perovskite solar cells: improved stability, reproducibility and high efficiency. *Energy & Environmental Science*, 9(6):1989–1997, 6 2016.

[10] Joel Jean, Justin Xiao, Robert Nick, Nicole Moody, Michel Nasilowski, Moungi Bawendi, and Vladimir Bulović. Synthesis cost dictates the commercial viability of lead sulfide and perovskite quantum dot photovoltaics. *Energy and Environmental Science*, 11(9):2295–2305, 9 2018.

[11] National Renewable Energy Laboratory, Best Research-Cell Efficiencies chart; https://www.nrel.gov/pv/assets/pdfs/best-research-cell-efficiencies.20191106.pdf. (National Renewable Energy Laboratory, Best Research-Cell Efficiencies chart; https://www.nrel.gov/pv/assets/pdfs/best-research-cell-efficiencies.20191106.pdf).

[12] Armin Richter, Jan Benick, Frank Feldmann, Andreas Fell, Martin Hermle, and Stefan W. Glunz. n-Type Si solar cells with passivating electron contact: Identifying sources for efficiency limitations by wafer thickness and resistivity variation. *Solar Energy Materials and Solar Cells*, 173:96–105, 12 2017.

[13] Tze Chien Sum, Shi Chen, Guichuan Xing, Xinfeng Liu, and Bo Wu. Energetics and dynamics in organic–inorganic halide perovskite photovoltaics and light emitters. *Nanotechnology*, 26(34):342001, 8 2015.

[14] Nena Milenkovic, Thomas Rachow, Stefan Janz, and Stefan Reber. Epitaxial Growth of High Quality n-type Silicon Foils in a Quasi-inline APCVD Reactor. In *Energy Procedia*, volume 77, pages 613–618. Elsevier Ltd, 8 2015.

[15] Jérémy Barbé, Adam Pockett, Vasil Stoichkov, Declan Hughes, Harrison Ka Hin Lee, Matthew Carnie, Trystan Watson, and Wing C. Tsoi. In situ investigation of perovskite solar cells' efficiency and stability in a mimic stratospheric environment for high-altitude pseudo-satellites. *Journal of Materials Chemistry C*, 8(5):1715–1721, 2 2020.

[16] Hsinhan Tsai, Wanyi Nie, Jean Christophe Blancon, Constantinos C. Stoumpos, Reza Asadpour, Boris Harutyunyan, Amanda J. Neukirch, Rafael Verduzco, Jared J. Crochet, Sergei Tretiak, Laurent Pedesseau, Jacky Even, Muhammad A. Alam, Gautam Gupta, Jun Lou, Pulickel M. Ajayan, Michael J. Bedzyk, Mercouri G. Kanatzidis, and Aditya D. Mohite. High-efficiency two-dimensional ruddlesden-popper perovskite solar cells. *Nature*, 536(7616):312–317, 7 2016.

[17] Sai Bai, Peimei Da, Cheng Li, Zhiping Wang, Zhongcheng Yuan, Fan Fu, Maciej Kawecki, Xianjie Liu, Nobuya Sakai, Jacob Tse Wei Wang, Sven Huettner, Stephan Buecheler, Mats Fahlman, Feng Gao, and Henry J. Snaith. Planar

perovskite solar cells with long-term stability using ionic liquid additives, 7 2019.

[18] Noor Titan Putri Hartono, Shijing Sun, María C. Gélvez-Rueda, Polly J. Pierone, Matthew P. Erodici, Jason Yoo, Fengxia Wei, Moungi Bawendi, Ferdinand C. Grozema, Meng Ju Sher, Tonio Buonassisi, and Juan Pablo Correa-Baena. The effect of structural dimensionality on carrier mobility in lead-halide perovskites. *Journal of Materials Chemistry A*, 7(41):23949–23957, 2019.

[19] Alexander Z. Chen, Michelle Shiu, Xiaoyu Deng, Mustafa Mahmoud, Depei Zhang, Benjamin J. Foley, Seung Hun Lee, Gaurav Giri, and Joshua J. Choi. Understanding the Formation of Vertical Orientation in Two-dimensional Metal Halide Perovskite Thin Films. *Chemistry of Materials*, 31(4):1336–1343, 2 2019.

[20] Himchan Cho, Su Hun Jeong, Min Ho Park, Young Hoon Kim, Christoph Wolf, Chang Lyoul Lee, Jin Hyuck Heo, Aditya Sadhanala, No Soung Myoung, Seunghyup Yoo, Sang Hyuk Im, Richard H. Friend, and Tae Woo Lee. Overcoming the electroluminescence efficiency limitations of perovskite light-emitting diodes. *Science*, 350(6265):1222–1225, 12 2015.

[21] William Shockley and Hans J. Queisser. Detailed balance limit of efficiency of p-n junction solar cells. *Journal of Applied Physics*, 32(3):510–519, 3 1961.

[22] Jean Francois Guillemoles, Thomas Kirchartz, David Cahen, and Uwe Rau. Guide for the perplexed to the Shockley–Queisser model for solar cells. *Nature Photonics*, 13(8):501–505, 2019.

[23] Uwe Rau. Reciprocity relation between photovoltaic quantum efficiency and electroluminescent emission of solar cells. *Physical Review B - Condensed Matter and Materials Physics*, 76(8), 8 2007.

[24] Deying Luo, Rui Su, Wei Zhang, Qihuang Gong, and Rui Zhu. Minimizing non-radiative recombination losses in perovskite solar cells, 1 2020.

[25] Jason J. Yoo, Sarah Wieghold, Melany C. Sponseller, Matthew R. Chua, Sophie N. Bertram, Noor Titan Putri Hartono, Jason S. Tresback, Eric C. Hansen, Juan Pablo Correa-Baena, Vladimir Bulović, Tonio Buonassisi, Seong Sik Shin, and Moungi G. Bawendi. An interface stabilized perovskite solar cell with high stabilized efficiency and low voltage loss. *Energy and Environmental Science*, 12(7):2192–2199, 7 2019.

[26] Henry J. Snaith. Present status and future prospects of perovskite photovoltaics. *Nature Materials*, 17(5):372–376, 5 2018.

[27] Nam-Gyu Park, Michael Grätzel, Tsutomu Miyasaka, Kai Zhu, and Keith Emery. Towards stable and commercially available perovskite solar cells. *Nature Energy*, 1(11):16152, 10 2016.

[28] Juan-Pablo Correa-Baena, Michael Saliba, Tonio Buonassisi, Michael Grätzel, Antonio Abate, Wolfgang Tress, and Anders Hagfeldt. Promises and challenges of perovskite solar cells. *Science (New York, N.Y.)*, 358(6364):739–744, 11 2017.

[29] Michael Saliba, Taisuke Matsui, Konrad Domanski, Ji-Youn Youn Seo, Amita Ummadisingu, Shaik M. Zakeeruddin, Juan-Pablo Pablo Correa-Baena, Wolfgang R. Tress, Antonio Abate, Anders Hagfeldt, and Michael Grätzel. Incorporation of rubidium cations into perovskite solar cells improves photovoltaic performance. *Science (New York, N.Y.)*, 354(6309):206–209, 9 2016.

[30] Abhishek Swarnkar, Ashley R Marshall, Erin M Sanehira, Boris D Chernomordik, David T Moore, Jeffrey A Christians, Tamoghna Chakrabarti, and Joseph M Luther. Quantum dot-induced phase stabilization of α-CsPbI3 perovskite for high-efficiency photovoltaics. *Science (New York, N.Y.)*, 354(6308):92–95, 10 2016.

[31] Seong Sik Shin, Eun Joo Yeom, Woon Seok Yang, Seyoon Hur, Min Gyu Kim, Jino Im, Jangwon Seo, Jun Hong Noh, and Sang Il Seok. Colloidally prepared La-doped BaSnO3electrodes for efficient, photostable perovskite solar cells. *Science (New York, N.Y.)*, 356(6334):167–171, 4 2017.

[32] Woon Seok Yang, Byung-Wook Park, Eui Hyuk Jung, Nam Joong Jeon, Young Chan Kim, Dong Uk Lee, Seong Sik Shin, Jangwon Seo, Eun Kyu Kim, Jun Hong Noh, and Sang Il Seok. Iodide management in formamidinium-lead-halide-based perovskite layers for efficient solar cells. *Science (New York, N.Y.)*, 356(6345):1376–1379, 6 2017.

[33] Mojtaba Abdi-Jalebi, Zahra Andaji-Garmaroudi, Stefania Cacovich, Camille Stavrakas, Bertrand Philippe, Johannes M. Richter, Mejd Alsari, Edward P. Booker, Eline M. Hutter, Andrew J. Pearson, Samuele Lilliu, Tom J. Savenije, Håkan Rensmo, Giorgio Divitini, Caterina Ducati, Richard H. Friend, and Samuel D. Stranks. Maximizing and stabilizing luminescence from halide perovskites with potassium passivation. *Nature*, 555(7697):497–501, 3 2018.

[34] Yuchuan Shao, Zhengguo Xiao, Cheng Bi, Yongbo Yuan, and Jinsong Huang. Origin and elimination of photocurrent hysteresis by fullerene passivation in CH3NH3PbI3 planar heterojunction solar cells. *Nature Communications*, 5(1):5784, 12 2014.

[35] Gill Sang Han, Hyun Suk Chung, Byeong Jo Kim, Dong Hoe Kim, Jin Wook Lee, Bhabani Sankar Swain, Khalid Mahmood, Jin Sun Yoo, Nam-Gyu Park, Jung Heon Lee, and Hyun Suk Jung. Retarding charge recombination in perovskite solar cells using ultrathin MgO-coated TiO ₂ nanoparticulate films. *Journal of Materials Chemistry A*, 3(17):9160–9164, 4 2015.

[36] Hairen Tan, Ankit Jain, Oleksandr Voznyy, Xinzheng Lan, F Pelayo García de Arquer, James Z Fan, Rafael Quintero-Bermudez, Mingjian Yuan, Bo Zhang,

Yicheng Zhao, Fengjia Fan, Peicheng Li, Li Na Quan, Yongbiao Zhao, Zheng-Hong Lu, Zhenyu Yang, Sjoerd Hoogland, and Edward H Sargent. Efficient and stable solution-processed planar perovskite solar cells via contact passivation. *Science (New York, N.Y.)*, 355(6326):722–726, 2 2017.

[37] Xiaopeng Zheng, Bo Chen, Jun Dai, Yanjun Fang, Yang Bai, Yuze Lin, Haotong Wei, Xiao Cheng Zeng, and Jinsong Huang. Defect passivation in hybrid perovskite solar cells using quaternary ammonium halide anions and cations. *Nature Energy*, 2(7):17102, 6 2017.

[38] Yun Lin, Yang Bai, Yanjun Fang, Zhaolai Chen, Shuang Yang, Xiaopeng Zheng, Shi Tang, Ye Liu, Jingjing Zhao, and Jinsong Huang. Enhanced Thermal Stability in Perovskite Solar Cells by Assembling 2D/3D Stacking Structures. *The Journal of Physical Chemistry Letters*, 9(3):654–658, 2 2018.

[39] Ou Chen, Jing Zhao, Vikash P Chauhan, Jian Cui, Cliff Wong, Daniel K Harris, He Wei, Hee-Sun Han, Dai Fukumura, Rakesh K Jain, and Moungi G Bawendi. Compact high-quality CdSe-CdS core-shell nanocrystals with narrow emission linewidths and suppressed blinking. *Nature materials*, 12(5):445–51, 2013.

[40] Alex Neumüller, Oleg Sergeev, Stephan J. Heise, Segei Bereznev, Olga Volobujeva, Jose Fabio Lopez Salas, Martin Vehse, and Carsten Agert. Improved amorphous silicon passivation layer for heterojunction solar cells with post-deposition plasma treatment. *Nano Energy*, 43:228–235, 1 2018.

[41] Jian-Kun Sun, Sheng Huang, Xiao-Zhi Liu, Quan Xu, Qing-Hua Zhang, Wen-Jie Jiang, Ding-Jiang Xue, Jia-Chao Xu, Jing-Yuan Ma, Jie Ding, Qian-Qing Ge, Lin Gu, Xiao-Hong Fang, Hai-Zheng Zhong, Jin-Song Hu, and Li-Jun Wan. Polar Solvent Induced Lattice Distortion of Cubic CsPbI ₃ Nanocubes and Hierarchical Self-Assembly into Orthorhombic Single-Crystalline Nanowires. *Journal of the American Chemical Society*, 140(37):11705–11715, 9 2018.

[42] Kyung Taek Cho, Giulia Grancini, Yonghui Lee, Emad Oveisi, Jaehoon Ryu, Osbel Almora, Manuel Tschumi, Pascal Alexander Schouwink, Gabseok Seo, Sung Heo, Jucheol Park, Jyongsik Jang, Sanghyun Paek, Germà Garcia-Belmonte, and Mohammad Khaja Nazeeruddin. Selective growth of layered perovskites for stable and efficient photovoltaics. *Energy & Environmental Science*, 2018.

[43] Yasser Hassan, Yin Song, Ryan D. Pensack, Ahmed I. Abdelrahman, Yoichi Kobayashi, Mitchell A. Winnik, and Gregory D. Scholes. Structure-Tuned Lead Halide Perovskite Nanocrystals. *Advanced Materials*, 28(3):566–573, 1 2016.

[44] María C. Gélvez-Rueda, Eline M. Hutter, Duyen H. Cao, Nicolas Renaud, Constantinos C. Stoumpos, Joseph T. Hupp, Tom J. Savenije, Mercouri G. Kanatzidis, and Ferdinand C. Grozema. Interconversion between Free Charges

and Bound Excitons in 2D Hybrid Lead Halide Perovskites. *The Journal of Physical Chemistry C*, 121(47):26566–26574, 11 2017.

[45] Minsu Jung, Tae Joo Shin, Jangwon Seo, Gwisu Kim, and Sang Il Seok. Structural features and their functions in surfactant-armoured methylammonium lead iodide perovskites for highly efficient and stable solar cells. *Energy & Environmental Science*, 2018.

[46] Silver Hamill Turren-Cruz, Anders Hagfeldt, and Michael Saliba. Methylammonium-free, high-performance, and stable perovskite solar cells on a planar architecture. *Science*, 362(6413):449–453, 10 2018.

[47] Mengjin Yang, Zhen Li, Matthew O. Reese, Obadiah G. Reid, Dong Hoe Kim, Sebastian Siol, Talysa R. Klein, Yanfa Yan, Joseph J. Berry, Maikel F. A. M. van Hest, and Kai Zhu. Perovskite ink with wide processing window for scalable high-efficiency solar cells. *Nature Energy*, 2(5):17038, 3 2017.

[48] Kyung Taek Cho, Sanghyun Paek, Giulia Grancini, Cristina Roldán-Carmona, Peng Gao, Yonghui Lee, and Mohammad Khaja Nazeeruddin. Highly efficient perovskite solar cells with a compositionally engineered perovskite/hole transporting material interface. *Energy & Environmental Science*, 10(2):621–627, 2 2017.

[49] Ting Zhao, Chu Chen Chueh, Qi Chen, Adharsh Rajagopal, and Alex K.Y. Jen. Defect Passivation of Organic-Inorganic Hybrid Perovskites by Diammonium Iodide toward High-Performance Photovoltaic Devices. *ACS Energy Letters*, 1(4):757–763, 10 2016.

[50] Namyoung Ahn, Kwisung Kwak, Min Seok Jang, Heetae Yoon, Byung Yang Lee, Jong-Kwon Lee, Peter V. Pikhitsa, Junseop Byun, and Mansoo Choi. Trapped charge-driven degradation of perovskite solar cells. *Nature Communications*, 7:13422, 11 2016.

[51] John Ciro, Santiago Mesa, Jose Ignacio Uribe, Mario Alejandro Mejía-Escobar, Daniel Ramirez, Juan Felipe Montoya, Rafael Betancur, Hyun-Seok Yoo, Nam-Gyu Park, and Franklin Jaramillo. Optimization of the Ag/PCBM interface by a rhodamine interlayer to enhance the efficiency and stability of perovskite solar cells. *Nanoscale*, 9(27):9440–9446, 7 2017.

[52] Yongyoon Cho, Arman Mahboubi Soufiani, Jae Sung Yun, Jincheol Kim, Da Seul Lee, Jan Seidel, Xiaofan Deng, Martin A. Green, Shujuan Huang, and Anita W. Y. Ho-Baillie. Mixed 3D-2D Passivation Treatment for Mixed-Cation Lead Mixed-Halide Perovskite Solar Cells for Higher Efficiency and Better Stability. *Advanced Energy Materials*, page 1703392, 4 2018.

[53] Da Seul Lee, Jae Sung Yun, Jincheol Kim, Arman Mahboubi Soufiani, Sheng Chen, Yongyoon Cho, Xiaofan Deng, Jan Seidel, Sean Lim, Shujuan Huang, and

Anita W. Y. Ho-Baillie. Passivation of Grain Boundaries by Phenethylammonium in Formamidinium-Methylammonium Lead Halide Perovskite Solar Cells. *ACS Energy Letters*, pages 647–654, 2 2018.

[54] Dae-Yong Son, Seul-Gi Kim, Ja-Young Seo, Seon-Hee Lee, Hyunjung Shin, Donghwa Lee, and Nam-Gyu Park. Universal Approach toward Hysteresis-Free Perovskite Solar Cell via Defect Engineering. *Journal of the American Chemical Society*, 140(4):1358–1364, 1 2018.

[55] Wolfgang Tress. Metal Halide Perovskites as Mixed Electronic–Ionic Conductors: Challenges and Opportunities—From Hysteresis to Memristivity. *The Journal of Physical Chemistry Letters*, 8(13):3106–3114, 7 2017.

[56] Eugen Zimmermann, Ka Kan Wong, Michael Müller, Hao Hu, Philipp Ehrenreich, Markus Kohlstädt, Uli Würfel, Simone Mastroianni, Gayathri Mathiazhagan, Andreas Hinsch, Tanaji P. Gujar, Mukundan Thelakkat, Thomas Pfadler, and Lukas Schmidt-Mende. Characterization of perovskite solar cells: Towards a reliable measurement protocol. *APL Materials*, 4(9):091901, 9 2016.

[57] Ricky B. Dunbar, Benjamin C. Duck, Tom Moriarty, Kenrick F. Anderson, Noel W. Duffy, Christopher J. Fell, Jincheol Kim, Anita Ho-Baillie, Doojin Vak, The Duong, YiLiang Wu, Klaus Weber, Alex Pascoe, Yi-Bing Cheng, Qianqian Lin, Paul L. Burn, Ripon Bhattacharjee, Hongxia Wang, and Gregory J. Wilson. How reliable are efficiency measurements of perovskite solar cells? The first inter-comparison, between two accredited and eight non-accredited laboratories. *Journal of Materials Chemistry A*, 5(43):22542–22558, 11 2017.

[58] Lukas Wagner, Sijo Chacko, Gayathri Mathiazhagan, Simone Mastroianni, and Andreas Hinsch. High Photovoltage of 1 V on a Steady-State Certified Hole Transport Layer-Free Perovskite Solar Cell by a Molten-Salt Approach. *ACS Energy Letters*, pages 1122–1127, 4 2018.

[59] Michael Saliba. Perovskite solar cells must come of age. *Science (New York, N.Y.)*, 359(6374):388–389, 1 2018.

[60] Nam Joong Jeon, Hyejin Na, Eui Hyuk Jung, Tae-Youl Youl Yang, Yong Guk Lee, Geunjin Kim, Hee-Won Won Shin, Sang Il Seok, Jaemin Lee, and Jangwon Seo. A fluorene-terminated hole-transporting material for highly efficient and stable perovskite solar cells. *Nature Energy*, 3(8):682–689, 8 2018.

[61] Qi Jiang, Yang Zhao, Xingwang Zhang, Xiaolei Yang, Yong Chen, Zema Chu, Qiufeng Ye, Xingxing Li, Zhigang Yin, and Jingbi You. Surface passivation of perovskite film for efficient solar cells. *Nature Photonics*, 13(7):460–466, 7 2019.

[62] Yanbo Wang, Tianhao Wu, Julien Barbaud, Weiyu Kong, Danyu Cui, Han Chen, Xudong Yang, and Liyuan Han. Stabilizing heterostructures of soft perovskite semiconductors. *Science*, 365(6454):687–691, 8 2019.

[63] Jeffrey A. Christians, Philip Schulz, Jonathan S. Tinkham, Tracy H. Schloemer, Steven P. Harvey, Bertrand J. Tremolet De Villers, Alan Sellinger, Joseph J. Berry, and Joseph M. Luther. Tailored interfaces of unencapsulated perovskite solar cells for >1,000 hour operational stability. *Nature Energy*, 3(1):68–74, 1 2018.

[64] Wei Chen, Yongzhen Wu, Youfeng Yue, Jian Liu, Wenjun Zhang, Xudong Yang, Han Chen, Enbing Bi, Islam Ashraful, Michael Grätzel, and Liyuan Han. Efficient and stable large-area perovskite solar cells with inorganic charge extraction layers. *Science*, 350(6263):944–948, 11 2015.

[65] Yongzhen Wu, Xudong Yang, Wei Chen, Youfeng Yue, Molang Cai, Fengxian Xie, Enbing Bi, Ashraful Islam, and Liyuan Han. Perovskite solar cells with 18.21% efficiency and area over 1 cm2 fabricated by heterojunction engineering. *Nature Energy*, 1(11):1–7, 9 2016.

[66] Oki Gunawan, Seong Ryul Pae, Douglas M. Bishop, Yudistira Virgus, Jun Hong Noh, Nam Joong Jeon, Yun Seog Lee, Xiaoyan Shao, Teodor Todorov, David B. Mitzi, and Byungha Shin. Carrier-resolved photo-Hall effect. *Nature*, 575(7781):151–155, 11 2019.

[67] Sarah E. Sofia, Hao Wang, Annalisa Bruno, Jose Luis Cruz-Campa, Tonio Buonassisi, and Ian Marius Peters. Roadmap for cost-effective, commercially-viable perovskite silicon tandems for the current and future PV market. *Sustainable Energy & Fuels*, pages 852–862, 2020.

[68] Joel Jean, Michael Woodhouse, and Vladimir Bulović. Accelerating Photovoltaic Market Entry with Module Replacement. *Joule*, 3(11):2824–2841, 2019.

[69] Lisa Krückemeier, Uwe Rau, Martin Stolterfoht, and Thomas Kirchartz. How to Report Record Open-Circuit Voltages in Lead-Halide Perovskite Solar Cells. *Advanced Energy Materials*, 10(1):1902573, 1 2020.

[70] Eui Hyuk Jung, Nam Joong Jeon, Eun Young Park, Chan Su Moon, Tae Joo Shin, Tae Youl Yang, Jun Hong Noh, and Jangwon Seo. Efficient, stable and scalable perovskite solar cells using poly(3-hexylthiophene), 3 2019.

[71] Kwang Ho Jung, Ja Young Seo, Seonhee Lee, Hyunjung Shin, and Nam Gyu Park. Solution-processed SnO2 thin film for a hysteresis-free planar perovskite solar cell with a power conversion efficiency of 19.2%. *Journal of Materials Chemistry A*, 5(47):24790–24803, 2017.

[72] Shengwei Shi, Jing Li, Tongle Bu, Shili Yang, Junyan Xiao, Yong Peng, Wei Li, Jie Zhong, Zhiliang Ku, Yi Bing Cheng, and Fuzhi Huang. Room-temperature synthesized SnO2 electron transport layers for efficient perovskite solar cells. *RSC Advances*, 9(18):9946–9950, 2019.

[73] Jing Li, Tongle Bu, Yifan Liu, Jing Zhou, Jielin Shi, Zhiliang Ku, Yong Peng, Jie Zhong, Yi Bing Cheng, and Fuzhi Huang. Enhanced Crystallinity of Low-Temperature Solution-Processed SnO2 for Highly Reproducible Planar Perovskite Solar Cells. *ChemSusChem*, 11(17):2898–2903, 2018.

[74] Seonghwa Jeong, Seongrok Seo, Hyoungmin Park, and Hyunjung Shin. Atomic layer deposition of a SnO 2 electron-transporting layer for planar perovskite solar cells with a power conversion efficiency of 18.3%. *Chemical Communications*, 55(17):2433–2436, 2019.

[75] Matthew Kam, Qianpeng Zhang, Daquan Zhang, and Zhiyong Fan. Room-Temperature Sputtered SnO 2 as Robust Electron Transport Layer for Air-Stable and Efficient Perovskite Solar Cells on Rigid and Flexible Substrates. *Scientific Reports*, 9(1):1–10, 2019.

[76] Alan Jiwan Yun, Jinhyun Kim, Taehyun Hwang, and Byungwoo Park. Origins of Efficient Perovskite Solar Cells with Low-Temperature Processed SnO2 Electron Transport Layer. *ACS Applied Energy Materials*, 2(5):3554–3560, 2019.

[77] Fawad Ali, Ngoc Duy Pham, H. Jonathan Bradford, Nima Khoshsirat, Ken Ostrikov, John M. Bell, Hongxia Wang, and Tuquabo Tesfamichael. Tuning the Amount of Oxygen Vacancies in Sputter-Deposited SnOx films for Enhancing the Performance of Perovskite Solar Cells. *ChemSusChem*, 11(18):3096–3103, 2018.

[78] Elham Halvani Anaraki, Ahmad Kermanpur, Matthew T. Mayer, Ludmilla Steier, Taha Ahmed, Silver Hamill Turren-Cruz, Jiyoun Seo, Jingshan Luo, Shaik Mohammad Zakeeruddin, Wolfgang Richard Tress, Tomas Edvinsson, Michael Grätzel, Anders Hagfeldt, and Juan Pablo Correa-Baena. Low-Temperature Nb-Doped SnO2 Electron-Selective Contact Yields over 20% Efficiency in Planar Perovskite Solar Cells. *ACS Energy Letters*, 3(4):773–778, 4 2018.

[79] Juan Pablo Correa Baena, Ludmilla Steier, Wolfgang Tress, Michael Saliba, Stefanie Neutzner, Taisuke Matsui, Fabrizio Giordano, T. Jesper Jacobsson, Ajay Ram Srimath Kandada, Shaik M. Zakeeruddin, Annamaria Petrozza, Antonio Abate, Mohammad Khaja Nazeeruddin, Michael Grätzel, and Anders Hagfeldt. Highly efficient planar perovskite solar cells through band alignment engineering. *Energy & Environmental Science*, 8(10):2928–2934, 10 2015.

[80] Hiroaki Uchiyama, Hirotoshi Ohgi, and Hiroaki Imai. Selective preparation of SnO2 and SnO crystals with controlled morphologies in an aqueous solution system. *Crystal Growth and Design*, 6(9):2186–2190, 2006.

[81] C. Ararat Ibarguen, A. Mosquera, R. Parra, M. S. Castro, and J. E. Rodríguez-Páez. Synthesis of SnO2 nanoparticles through the controlled precipitation route. *Materials Chemistry and Physics*, 101(2-3):433–440, 2007.

[82] Saptarshi Ghosh and Somenath Roy. Effect of ageing on Sn6O4(OH)4 in aqueous medium—simultaneous production of SnO and SnO2 nanoparticles at room temperature. *Journal of Sol-Gel Science and Technology*, 81(3):769–773, 2017.

[83] Na Li, Kui Du, Gang Liu, Yingpeng Xie, Guangmin Zhou, Jing Zhu, Feng Li, and Hui Ming Cheng. Effects of oxygen vacancies on the electrochemical performance of tin oxide. *Journal of Materials Chemistry A*, 1(5):1536–1539, 2013.

[84] Yuanjie Yang, Yuhua Wang, and Shu Yin. Oxygen vacancies confined in SnO 2 nanoparticles for desirable electronic structure and enhanced visible light photocatalytic activity. *Applied Surface Science*, 420:399–406, 2017.

[85] Menglin Sun, Yiguo Su, Chunfang Du, Qihang Zhao, and Zhiliang Liu. Self-doping for visible light photocatalytic purposes: Construction of SiO2/SnO2/SnO2:Sn2+ nanostructures with tunable optical and photocatalytic performance. *RSC Advances*, 4(58):30820–30827, 2014.

[86] Hongkang Wang, Kunpeng Dou, Wey Yang Teoh, Yawen Zhan, Tak Fu Hung, Feihu Zhang, Jiaqiang Xu, Ruiqin Zhang, and Andrey L. Rogach. Engineering of facets, band structure, and gas-sensing properties of hierarchical Sn2+-Doped SnO2 nanostructures. *Advanced Functional Materials*, 23(38):4847–4853, 2013.

[87] Cong Min Fan, Yin Peng, Qing Zhu, Ling Lin, Rui Xia Wang, and An Wu Xu. Synproportionation reaction for the fabrication of Sn2+ self-doped SnO2-x nanocrystals with tunable band structure and highly efficient visible light photocatalytic activity. *Journal of Physical Chemistry C*, 117(46):24157–24166, 2013.

[88] Ayan Sarkar and Gobinda Gopal Khan. The formation and detection techniques of oxygen vacancies in titanium oxide-based nanostructures. *Nanoscale*, 11(8):3414–3444, 2019.

[89] Dan Han, Baolai Jiang, Ji Feng, Yadong Yin, and Wenshou Wang. Photocatalytic Self-Doped SnO 2x Nanocrystals Drive Visible-Light-Responsive Color Switching. *Angewandte Chemie - International Edition*, 56(27):7792–7796, 2017.

[90] Bing Wang, Meng Zhang, Xun Cui, Zewei Wang, Matthew Rager, Yingkui Yang, Zhigang Zou, Zhong Lin Wang, and Zhiqun Lin. Unconventional Route to Oxygen-Vacancy-Enabled Highly Efficient Electron Extraction and Transport in Perovskite Solar Cells. *Angewandte Chemie - International Edition*, pages 1611–1618, 2019.

[91] Jinghui Wang, Hui Li, Sugang Meng, Xiangju Ye, Xianliang Fu, and Shifu Chen. Controlled synthesis of Sn-based oxides: Via a hydrothermal method and their visible light photocatalytic performances. *RSC Advances*, 7(43):27024–27032, 2017.

[92] R. L. Cohen and K. W. West. Solution Chemistry and Colloid Formation in the Chloride Sensitizing Process. *Journal of the Electrochemical Society*, 119(4):433–438, 1972.

[93] Taisuke Matsui, Teruaki Yamamoto, Takashi Nishihara, Ryosuke Morisawa, Tomoyasu Yokoyama, Takashi Sekiguchi, and Takayuki Negami. Compositional Engineering for Thermally Stable, Highly Efficient Perovskite Solar Cells Exceeding 20% Power Conversion Efficiency with 85 °C/85% 1000 h Stability. *Advanced Materials*, page 1806823, 1 2019.

[94] Jiajia Ning, Quanqin Dai, Tao Jiang, Kangkang Men, Donghua Liu, Ningru Xiao, Chenyuan Li, Dongmei Li, Bingbing Liu, Bo Zou, Guangtian Zou, and William W. Yu. Facile synthesis of tin oxide nanoflowers: A potential high-capacity lithium-ion-storage material. *Langmuir*, 25(3):1818–1821, 2009.

[95] Jiayong Gan, Xihong Lu, Jingheng Wu, Shilei Xie, Teng Zhai, Minghao Yu, Zishou Zhang, Yanchao Mao, Shing Chi Ian Wang, Yong Shen, and Yexiang Tong. Oxygen vacancies promoting photoelectrochemical performance of in 2 O 3 nanocubes. *Scientific Reports*, 3:1–7, 2013.

[96] Hanul Min, Maengsuk Kim, Seung-Un Lee, Hyeonwoo Kim, Gwisu Kim, Keunsu Choi, Jun Hee Lee, and Sang Il Seok. Efficient, stable solar cells by using inherent bandgap of α-phase formamidinium lead iodide. *Science*, 366(6466):749–753, 11 2019.

[97] Jacob Tse Wei Wang, Zhiping Wang, Sandeep Pathak, Wei Zhang, Dane W. Dequilettes, Florencia Wisnivesky-Rocca-Rivarola, Jian Huang, Pabitra K. Nayak, Jay B. Patel, Hanis A. Mohd Yusof, Yana Vaynzof, Rui Zhu, Ivan Ramirez, Jin Zhang, Caterina Ducati, Chris Grovenor, Michael B. Johnston, David S. Ginger, Robin J. Nicholas, and Henry J. Snaith. Efficient perovskite solar cells by metal ion doping. *Energy and Environmental Science*, 9(9):2892–2901, 9 2016.

[98] Makhsud I. Saidaminov, Junghwan Kim, Ankit Jain, Rafael Quintero-Bermudez, Hairen Tan, Guankui Long, Furui Tan, Andrew Johnston, Yicheng Zhao, Oleksandr Voznyy, and Edward H. Sargent. Suppression of atomic vacancies via incorporation of isovalent small ions to increase the stability of halide perovskite solar cells in ambient air. *Nature Energy*, 3(8):1, 7 2018.

[99] Yuhang Liu, Seckin Akin, Linfeng Pan, Ryusuke Uchida, Neha Arora, Jovana V. Milić, Alexander Hinderhofer, Frank Schreiber, Alexander R. Uhl, Shaik M. Zakeeruddin, Anders Hagfeldt, M. Ibrahim Dar, Michael Grätzel, M. Ibrahim Dar, and Michael Grätzel. Ultrahydrophobic 3D/2D fluoroarene bilayer-based water-resistant perovskite solar cells with efficiencies exceeding 22%. *Science Advances*, 5(6):eaaw2543, 6 2019.

[100] Juan-Pablo Correa-Baena, Yanqi Luo, Thomas M. Brenner, Jordan Snaider, Shijing Sun, Xueying Li, Mallory A. Jensen, Noor Titan Putri Hartono, Lea

Nienhaus, Sarah Wieghold, Jeremy R. Poindexter, Shen Wang, Ying Shirley Meng, Ti Wang, Barry Lai, Martin V. Holt, Zhonghou Cai, Moungi G. Bawendi, Libai Huang, Tonio Buonassisi, and David P. Fenning. Homogenized halides and alkali cation segregation in alloyed organic-inorganic perovskites. *Science*, 363(6427):627–631, 2 2019.

[101] Waqaas Rehman, Rebecca L. Milot, Giles E. Eperon, Christian Wehrenfennig, Jessica L. Boland, Henry J. Snaith, Michael B. Johnston, and Laura M. Herz. Charge-Carrier Dynamics and Mobilities in Formamidinium Lead Mixed-Halide Perovskites. *Advanced Materials*, 27(48):7938–7944, 12 2015.

[102] Dong Hoe Kim, Jaehong Park, Zhen Li, Mengjin Yang, Ji-Sang Park, Ik Jae Park, Jin Young Kim, Joseph J. Berry, Garry Rumbles, and Kai Zhu. 300% Enhancement of Carrier Mobility in Uniaxial-Oriented Perovskite Films Formed by Topotactic-Oriented Attachment. *Advanced Materials*, 29(23):1606831, 6 2017.

[103] David Kiermasch, Lidón Gil-Escrig, Henk J. Bolink, and Kristofer Tvingstedt. Effects of Masking on Open-Circuit Voltage and Fill Factor in Solar Cells. *Joule*, 3(1):16–26, 2019.

[104] Kebin Lin, Jun Xing, Li Na Quan, F. Pelayo García de Arquer, Xiwen Gong, Jianxun Lu, Liqiang Xie, Weijie Zhao, Di Zhang, Chuanzhong Yan, Wenqiang Li, Xinyi Liu, Yan Lu, Jeffrey Kirman, Edward H. Sargent, Qihua Xiong, and Zhanhua Wei. Perovskite light-emitting diodes with external quantum efficiency exceeding 20 per cent, 10 2018.

[105] Yu Cao, Nana Wang, He Tian, Jingshu Guo, Yingqiang Wei, Hong Chen, Yanfeng Miao, Wei Zou, Kang Pan, Yarong He, Hui Cao, You Ke, Mengmeng Xu, Ying Wang, Ming Yang, Kai Du, Zewu Fu, Decheng Kong, Daoxin Dai, Yizheng Jin, Gongqiang Li, Hai Li, Qiming Peng, Jianpu Wang, and Wei Huang. Perovskite light-emitting diodes based on spontaneously formed submicrometrescale structures, 10 2018.

[106] Takayuki Chiba, Yukihiro Hayashi, Hinako Ebe, Keigo Hoshi, Jun Sato, Shugo Sato, Yong Jin Pu, Satoru Ohisa, and Junji Kido. Anion-exchange red perovskite quantum dots with ammonium iodine salts for highly efficient light-emitting devices. *Nature Photonics*, 12(11):681–687, 11 2018.

I did it!!!